



Universiteit
Leiden
The Netherlands

Unveiling the electrolyte effects of CO₂ electroreduction to CO and H₂ evolution from the interfacial pH perspective

Liu, X.

Citation

Liu, X. (2025, February 6). *Unveiling the electrolyte effects of CO₂ electroreduction to CO and H₂ evolution from the interfacial pH perspective*. Retrieved from <https://hdl.handle.net/1887/4178928>

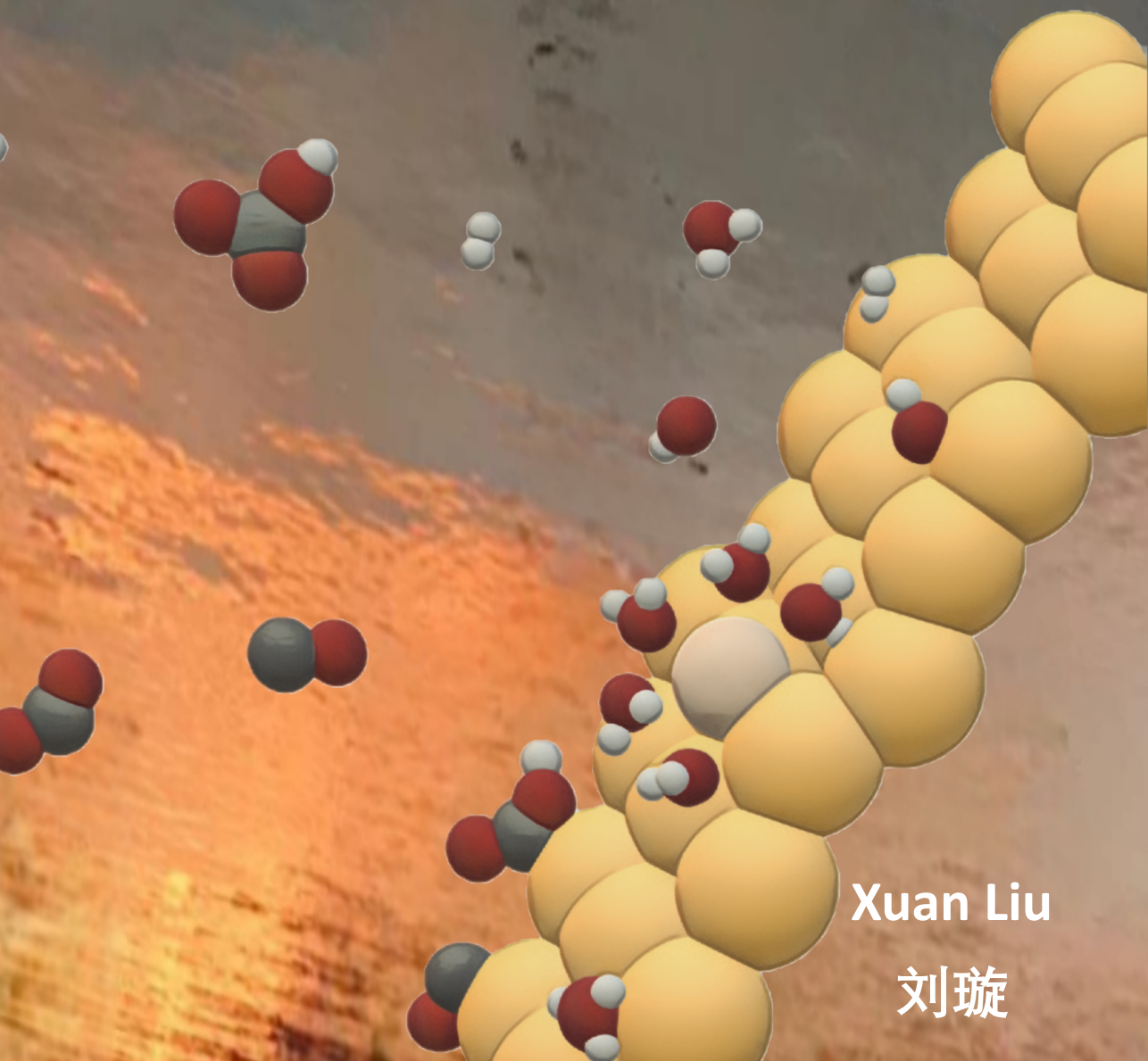
Version: Publisher's Version

[Licence agreement concerning inclusion of doctoral thesis in the Institutional Repository of the University of Leiden](#)

License: <https://hdl.handle.net/1887/4178928>

Note: To cite this publication please use the final published version (if applicable).

Unveiling the electrolyte effects of CO₂ electroreduction to CO and H₂ Evolution from the interfacial pH perspective



Xuan Liu

刘璇

Unveiling the electrolyte effects of CO₂ electroreduction to CO and H₂ Evolution from the interfacial pH perspective

Proefschrift

ter verkrijging van
de graad van doctor aan de Universiteit Leiden,
op gezag van rector magnificus prof.dr.ir. H. Bijl,
volgens besluit van het college voor promoties
te verdedigen op donderdag 6 februari 2025

klokke 10:00 uur

door

Xuan Liu

geboren te Si chuan, China
in 1995

Promotores:

Prof. dr. M. T. M. Koper

Prof. dr. ir. B.M. Weckhuysen (Universiteit Utrecht)

PROMOTIECOMMISSIE:

Prof. dr. M. Ubbink

Prof. dr. S.A. Bonnet

Dr. D.G.H. Hetterscheid

Prof. E.R. Savinova (Université de Strasbourg)

Dr. T.E. Burdyny (Delft University of Technology)

This work was supported by the project number ENPPS.IPP.019.002 in the framework of the Research Program of the Materials Innovation Institute (M2i) and received funding from Tata Steel Nederland Technology BV and the Dutch Research Council (NWO) in the framework of the ENW PPP Fund for the top sectors and from the Ministry of Economic Affairs in the framework of the “PPS Toeslagregeling”.

Table of Contents

Chapter 1. Introduction.....	2
Chapter 2. Interfacial pH measurements using a Rotating Ring-Disc Electrode with a voltammetric pH sensor	24
Chapter 3. Interfacial pH Measurements during CO ₂ Reduction on Gold Using a Rotating Ring-Disk Electrode	40
Chapter 4. Tuning the Interfacial Reaction Environment for CO ₂ Electroreduction to CO in Mildly Acidic Media	60
Chapter 5. The Effect of Weak Proton Donors on the Steady-State Behavior of Hydrogen Evolution in Mildly Acidic Media	82
Appendix A. Supporting Information to Chapter 2.....	100
Appendix B. Supporting Information to Chapter 3.....	110
Appendix C. Supporting Information to Chapter 4.....	120
Appendix D. Supporting Information to Chapter 5.....	130
Summary.....	143
Samenvatting	145
Summary in Chinese	147
List of publications	149
Curriculum vitae	150
Acknowledgements	152



Chapter 1

Introduction



1.1 Electrochemistry bridging electricity and chemical power

Electrochemistry is the branch of chemistry that investigates redox reactions in which electrons are transferred from the reductant (increasing valence of the elements) to the oxidant (decreasing valence of the elements). Redox reactions are universal and wildly utilized in our daily lives e.g. combustion of fuels, corrosion of metals, and photosynthesis and respiration in plants. Energy can be stored or released *via* an electrochemical process, making electrochemistry one of the most promising alternatives for relieving the energy crisis.

Dating back to the 16th century, electrochemistry originates from the exploration of magnetism and static electricity. William Gilbert, known as "The Father of Magnetism," discovered multiple methods for producing and strengthening magnets and made a principal contribution to the distinguishing between static electricity and magnetism. In fact, the English word "electricity" was derived from Gilbert's 1600 Neo-Latin "electricus", meaning "like amber in its attractive properties". The 18th century marked the birth of electrochemistry with experiments by Charles François de Cisternay Du Fay. Inspired by the invention of the first gas-discharge lamp by Francis Hauksbee in 1705, and the demonstration of conductivity of electricity by Stephen Gray and Jean Desaguliers in the 1730s, Charles François de Cisternay Du Fay discovered two forms of static electricity and proposed that like charges repel each other whilst unlike charges attract. Later, in 1799, a significant advancement was made by Alessandro Volta's ¹ invention of the first modern electric battery, the voltaic pile, which output a continuous electric current. Volta's work challenged Luigi Galvani's theory of animal electricity and for the first-time correlated electricity production with chemical power, which was further confirmed by the electrical theory of chemical affinities by Humphry Davy. By using the electric power supplied by the voltaic pile, Humphry Davy discovered several new elements such as sodium, potassium, and calcium, with the electric power converted to the chemical power. Noteworthy, water electrolysis was accomplished and properly interpreted even before the invention of the voltaic pile, in 1789. Without a stable current offered by the voltaic pile, a Dutch merchant Adriaan Paets van Troostwijk and his friend Johan Rudolph Deiman produced hydrogen and oxygen out of water by the electric discharge with a electrostatic generator.²

Throughout the 19th and 20th centuries, with the development of physical and chemical theories, mathematical methods, and experimental techniques, the investigations of electrochemistry notably thrived and largely enhanced the popularity and accessibility of electric power, which in turn boosted the industrial productivity and spawned the industrial revolution. In recent decades, electrochemistry has become a hot research area of versatile applications, contributing to advancements in batteries,³ fuel cells,⁴ electrolysis,⁵

corrosion prevention,⁶ wastewater treatment,⁷ and biosensing.⁸

1.1.1 The electrochemical cell

A redox process generally consists of two half-reactions, involving a reduction reaction and an oxidation reaction. Separating the half-reactions in space by immersing two electronic conductors (the electrodes) in an electrolyte solution and connecting them externally by a conductor (commonly a metal wire), an electrochemical cell is constructed. An electrochemical cell consists thereby of two electrodes, namely a cathode where the reduction reaction takes place and an anode where the oxidation reaction takes place, and two charge transport paths, namely electronic transport through the wire and ionic

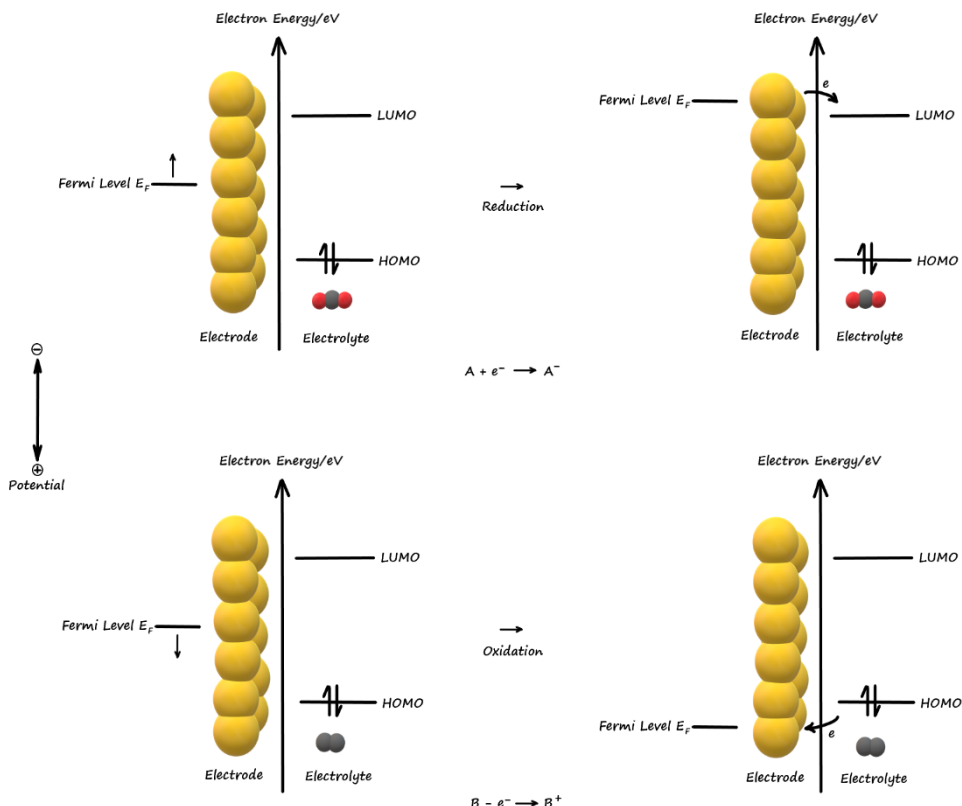


Figure 1. Representation of the heterogeneous electron transfer process between the Fermi energy level of the electrode and the molecule orbitals of the reactive species of a reduction reaction of A and an oxidation reaction of B respectively.

transport through the solution. Depending on the Gibbs free energy (G) difference between the reagents and the products, there are two types of electrochemical cells. In a galvanic cell, the G of the reagents is larger than that of the products, the redox reactions occur spontaneously, generating a faradaic current and releasing the chemical energy mostly into electric energy. On the other hand, an external energy supply is needed to drive the redox process in the opposite direction in a so-called electrolytic cell. The transfer of electrons occurs between the highest filled orbital of the electrode, known as the Fermi Energy Level (E_F) of a metal electrode, and the molecular orbitals of the reactant in the solution. By adjusting the electrode potential, the E_F of the electrode is adjusted with respect to the orbital energy levels in solution, to control the direction and extent of the reaction. As Figure 1 depicts, when negatively shifting the electrode potential, the energy of the electrons is lifted to reach the Lowest Unoccupied Molecular Orbital (LUMO) of the reagent, resulting in the electron transfer from the electrode to the reactant and a reduction current flow. In contrast, when the electrode potential is shifted in a positive direction, the energy of the electrons is lowered to approach the Highest Unoccupied Molecular Orbital (HOMO) of the reagent, leading to the electron transfer from the reactant to the electrode and an oxidation current flow. In commercial applications, galvanic cells are often employed as power sources such as batteries while the electrolytic cells are involved in the electrosynthesis process e.g. the production of chlorine or hydrogen, and in electroplating.

In an electrochemical process, the charge transferred is related to the extent of the chemical reaction. According to the Faraday's law (eq. 1):

$$Q = nFN \quad (1)$$

where Q is the charge transferred (C, 1 C is equivalent to 6.24×10^{18} electrons), n is the stoichiometric number of electrons transferred in the corresponding redox reaction, F denotes the Faraday's constant 96485 C/mol, and N (mol) is the amount of the reactants being consumed or the products being formed. In a single electron transfer reaction, the passage of 96485 C in the circuit brings about 1 equivalent of reaction (e.g., consumption of 1 mole of reactant or production of 1 mole of product). The current i , as defined in eq. 2:

$$i = \frac{dQ}{dt} \quad (2)$$

is the time derivative of the charge, where a current of 1 ampere (A) is equivalent to 1C/s.

By combining eqs. 1.1-1.2, the current is linearly related to the reaction rate $\frac{dN}{dt}$ (eq. 1.3):

$$v = \frac{dN}{dt} = \frac{dQ}{nFdt} = \frac{i}{nF} = \frac{i}{nFA}$$

(3)

Hence the current i and current density j are direct measures of the reaction rate of an electrochemical process. In fact, for a unimolecular elementary reaction (eq. 4):



the net reaction rate is:

$$v_{net} = v_f - v_b = k_f C_O - k_b C_R = \frac{i}{FA} \quad (5)$$

where v_f , k_f and v_b , k_b denote the reaction rate and reaction rate constant of the forward and the backward reactions, respectively, and C_X is the concentration of species X. The reaction rate constant is determined by the Arrhenius Equation (eq. 6):

$$k = A e^{-E_A/RT} \quad (6)$$

where A is the frequency factor, E_A is the activation energy, R is the universal ideal gas constant ($8.314 \text{ J K}^{-1} \text{ mol}^{-1}$), and T is the temperature. As illustrated in the diagram of Figure 2, showing the free energy of the reaction as a function of the reaction coordinate, a change of electrode potential causes the movement of the “A + e” free energy curve, leading to a corresponding change in the activation energy. This means that the electrode potential tunes the activation energy, thereby modulating the reaction rate and the current density. By plotting the current or current density as a function of the electrode potential, a polarization (i vs. E) curve of the electrode process is obtained, which is ubiquitous in electrochemical studies. These curves can be quite informative about the nature of the underlying process, and how it depends on the electrolyte and electrode, and further analysis of the polarization curves discloses qualitative or quantitative details about the thermodynamics and kinetics of the reaction processes taking place on the electrode.

In the study of an electrochemical half-cell reaction, a three-electrode set-up as shown in Figure 1.3 is commonly employed, constituting of a working electrode, a reference electrode, and a counter electrode. The working electrode is the electrode where the reaction of interest takes place. The reference electrode is an electrode with a known and well-defined potential which approaches an ideally nonpolarizable electrode under small current passage, so that it serves as the reference of the electrode potential of the working electrode. The Reversible Hydrogen Electrode (RHE), saturated calomel electrode (SCE, $\text{Hg}/\text{Hg}_2\text{Cl}_2$) and Ag/AgCl electrode (Ag/AgCl) are frequently used as a reference electrode in practical studies. Since the absolute value of the electrode potential is unknown, the

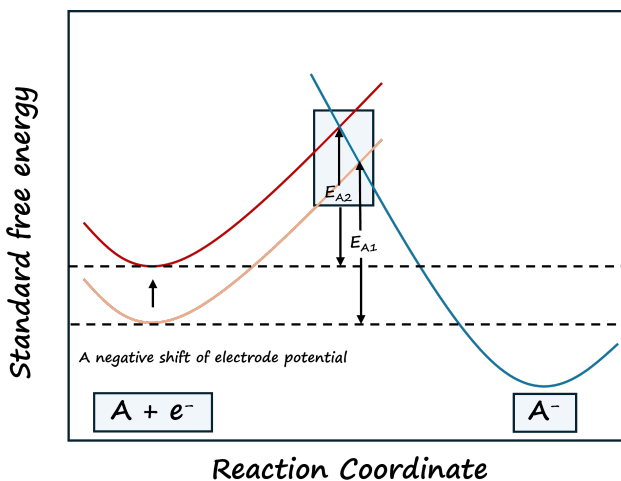


Figure 2. Schematic free energy diagram of the effects of a negative potential shift on the standard free energies of the partners in a redox reaction, and the corresponding changes in activation energy

potential of Standard Hydrogen Electrode (SHE, Pt/H₂ (a=1)) is standardized to be 0 V, and the potential of RHE, SCE, and Ag/AgCl are $-0.059 \cdot \text{pH}$ (the bulk pH of the electrolyte), 0.241 V, and 0.197 V vs SHE respectively. Current passes between the working electrode and the counter electrode to avoid any perturbation of the (potential of the) reference electrode. Investigations of the electrochemical behavior usually acquire valuable insights about the thermodynamic, kinetic, analytical, and other relevant aspects of the system by recording the excitation and response variables and applying an appropriate model to disentangle the information. They often proceed by keeping certain variables of the electrolysis cell constant while observing how other variables, e.g. current, potential, and species concentration change in response to controlled variables. For instance, chronoamperometry experiments during which the potential is kept constant while the current changes with time are often performed when studying the nucleation and growth process of electrodeposition and when testing the stability and durability of the electrocatalyst. Another way to investigate an electrochemical process is to monitor how the system responds to a perturbation. The electrochemical cell is subjected to a specific excitation function, and a specific response function is recorded, while all other system variables are kept constant. For example, Figure 3 illustrates a cyclic voltammetry (CV) measurement, which is one of the most used potential sweep methods in electrochemical research, in which the input electrode potential is ramped linearly with time in periodic

phases, leading to corresponding time-dependent current. CV curves usually exhibit so-called redox peaks. The shape and potential of these peaks provide information about the redox species, while the difference between the forward and backward scans indicates the kinetic reversibility of the redox couple.⁹

1.2 Electrochemical Interface

In contrast to homogeneous reactions, which occur in a single medium, electrochemical reactions take place heterogeneously at the electrode-electrolyte interface.¹⁰⁻¹¹ The characteristics of the interface impact the electrochemical performance importantly. At the interface, charge transfer and mass transport meet, in conjunction with potential and concentration gradients extending from the electrode surface to the bulk electrolyte. Understanding (the complexity of) this interface is therefore of paramount importance in electrochemical studies.

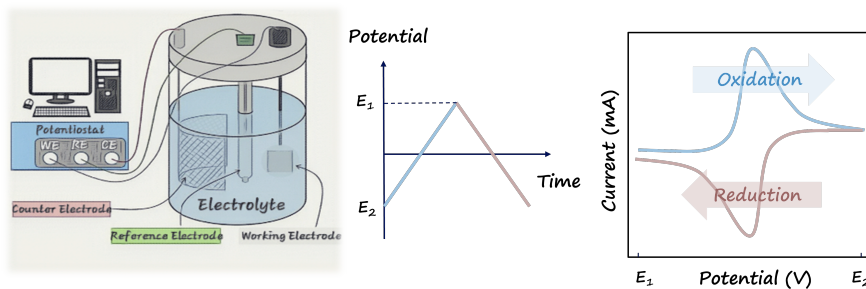


Figure 3. Schematic of a typical three-electrode electrolytic cell set-up and the cyclic voltammetry measurement where the blue curve denotes the forward scan where the electrode potential shifts positively and thus (typically) generating a positive current, while the red curve represents the

1.2.1 Electric double layer

The Electric Double Layer (EDL) is considered the core of the electrochemical interface. EDL corresponds to the spatial ordering of charge in the electrolyte that counters the surface charge on the electrode.¹² It is typically considered to consist of several layers of charged species, as shown in Figure 4, the first of which is located at the centers of the specifically adsorbed species at the electrode surface, known as the Inner Helmholtz Plane (IHP). This is also the location where catalytic reaction intermediates e.g. *CO in CO₂ electroreduction and *H in H₂ evolution reside. The second layer contains the solvated ions, their closest plane of approach known as the Outer Helmholtz Plane (OHP), where the solvated species reorganize their conformation prior to electron transfer. Due to the thermal motion in the

electrolyte, a third layer of charged species is distributed diffusely into the bulk electrolyte, known as the diffuse layer. The earliest EDL model was proposed by Helmholtz in the 19th century, who suggested a simple, rigid layer of ions adhering to the electrode surface. This model predicts a linear electrostatic potential profile across this interface leading to a constant capacitance. However, the model does not agree with the real EDL behavior as the capacitance varies with electrode potential. Later, Gouy and Chapman introduced the concept of a diffuse layer, where a Boltzmann distribution of the counterions was considered, resulting in the ions spreading out into the bulk electrolyte and a corresponding potential drop across the EDL. The Gouy-Chapman predicts a potential-dependent differential capacitance, with a minimum capacitance at the potential where the surface charge is zero. However, the Gouy-Chapman model does not explain the approximately constant capacitance observed at a highly polarized electrode surface. Stern integrated the ideas of the rigid adsorbed Helmholtz layer with the diffuse layer, which explains better the experimental observations of electrochemical interfaces. More advanced models have included the incorporation of ion size effects and solvent structure into EDL models. These considerations have led to the development of more complex models like the modified Gouy-Chapman-Stern model¹³⁻¹⁴ and the Bockris-Devanathan-Müller (BDM) model,¹⁵⁻¹⁶ which account for the finite size of ions and the orientation of solvent molecules, respectively.

The ongoing research in the field of EDL is focused on achieving a comprehensive

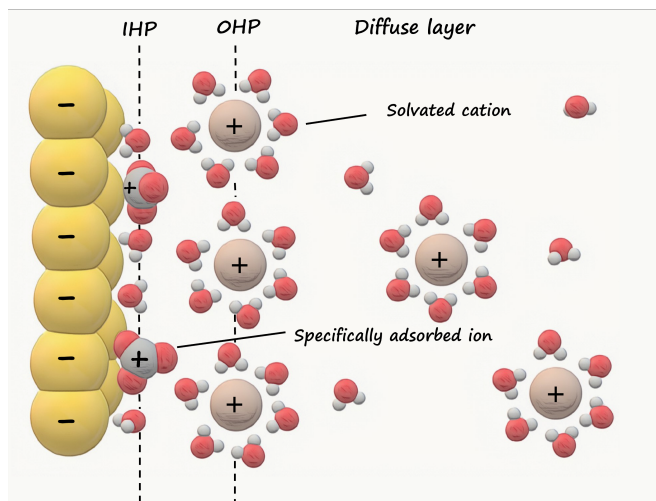


Figure 4. Schematic of the electric double layer region in aqueous solution including a negatively charged electrode surface and specifically adsorbed ions in the Inner Helmholtz Plane (IHP). OHP =

understanding of the interfacial phenomena at the molecular level, using advanced computational and experimental techniques like molecular dynamics simulations and *in-situ* spectroscopy. These studies aim to unravel the complexities of the EDL, such as the specific adsorption of ions,¹⁷ the role of solvent molecules,¹⁸ and the impact of electrode surface morphology¹⁹ on the EDL properties. The insights gained from these investigations are expected to accelerate the development of more reliable EDL models, which will further benefit the study of electrochemical processes and systems.

1.2.2 Electrode surface effect

As a vital component of the electrode-electrolyte interface, the electrode surface plays an indispensable role in electrochemical processes. When a reactive species arrives in the proximity of the electrode surface, it interacts with the surrounding solvent species and with the electrode surface itself. Depending on the interactions between the reactant and the electrode, the electrode surface functions differently in heterogeneous reactions. When the interaction is relatively weak, the reactant reorients the configuration of its solvation shell in the OHP but does not contact the surface directly during the reaction. This is known as the outer sphere electron transfer reaction, of which the redox reaction of $[\text{Ru}(\text{NH}_3)_6]^{2+/3+}$ would be an classic example, where the electrode surface merely serves as an electron reservoir and the nature of the electrode surface barely impacts the reaction. These reactions tend to proceed comparatively fast as there is no adsorption or bond formation or breakage occurring during the process. In contrast, if bond rearrangement or adsorption is involved in an electron transfer reaction, the reactive species partially loses its solvation shell and comes into direct contact with the surface in the IHP. Such processes are referred to as inner-sphere electron transfer reactions; electrocatalytic reactions belong to this class. In this scenario, the composition and the structure of the electrode surface markedly influence the electrochemical performance.

Considerable research efforts have been dedicated to revealing the relationship between the reaction performance and a certain parameter of the electrode or the active sites, such as the work function (E_F),²⁰ the strength of the metal-hydrogen bond,²¹⁻²² and the presence of the empty d-band orbitals.²³ One of the most distinguished empirical models is Sabatier's principle,²⁴ which correlates the reaction rate to the adsorption energy between the key catalytic intermediate binding to the electrode surface. A proper catalyst is expected to bind with the reaction intermediate with an intermediate strength. A strong interaction between the intermediate and the surface hinders the subsequent desorption and deactivates the reaction sites, while a weak interaction slows down the initial adsorption process. For instance, the Sabatier principle aids in interpreting the dependence of the CO_2

electroreduction reaction rate on the metal identity. Cu and Cu alloys ²⁵ are the most promising metal materials capable of producing multi-carbon species from CO₂ electroreduction, as they bind to the primary intermediate *CO appropriately. Strong adsorption of CO, such as with Pt, hampers the reaction performance, while weak adsorption of CO, as seen with Au, impedes subsequent reduction and mainly generates CO. ²⁶

Electrode surface modification customizes the composition and characteristics of the electrode surface, hence tuning its electronic structure to optimize the electron transfer rate of the reaction process. Research has shown that modifying the surface properties through strategies such as alloying, ^{25,27} doping, ²⁸⁻²⁹ or creating roughness ³⁰⁻³¹ can enhance the efficiency and selectivity of CO₂ electroreduction. The presence of certain metals or dopants in the catalyst can alter the electronic properties of the surface, thus affecting the reduction pathway and the energy barrier of the reaction. Specific surface facets provide distinctive active sites that promote the selectivity and activity for desired products. The activity of silver for CO₂ electroreduction, for example, has been reported to be strongly facet dependent. ³² Additionally, surface reconstruction and modification strategies, such as using surfactants, can significantly improve electrode performance. Studies reported that the electrode modified with Cetyltrimethylammonium bromide (CTAB) surfactant ³³⁻³⁴ exhibited a marked increase in CO₂ reduction activity and selectivity for CO production. This improvement was attributed to the formation of a favorable modified electrode/electrolyte interface with CTAB. Similarly, carbon-based electrodes functionalized with molecular organometallic complexes are beneficial to the dispersion of active components and facilitate the heterogeneous electron transfer, which further enhances the CO₂ electroreduction performance. ³⁵⁻³⁶

1.2.3 Mass transfer condition

During the (fast) electron transfer reaction at the interface, concentration gradients of the species involved in the reaction will develop from the electrode surface into the bulk electrolyte. This means that the interfacial concentration of the reactive species deviates considerably from the bulk value, which is due to the mismatch between the rate of charge transfer and mass transfer. Mass transfer is the result of gradients in the electrochemical potential, or the movement of solution by spontaneous or applied convection. Depending on different driving forces, there are three common modes of mass transfer, namely diffusion, migration, and convection. Diffusion denotes the movement of a species driven

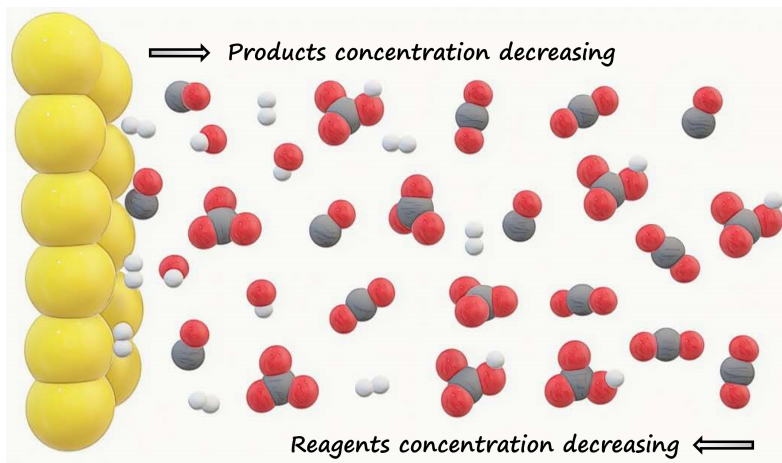


Figure 5. Schematic of the concentration gradients near the electrochemical interface where the product concentration increases from the electrode surface to the bulk phase while the reactant concentration decreases from the bulk phase to the electrode surface.

by a chemical potential gradient i.e. a concentration gradient. Migration involves the movements of a charged species driven by an electrical potential difference, while convection occurs due to stirring or hydrodynamic transport. The contribution of migration of the reactant can be neglected by using an excess of supporting electrolyte species in the solution, while convection can be ignored in a stagnant solution. Figure 5 illustrates that with the consumption of the reactant and generation of the products by the reaction, concentration gradients are formed, resulting in the transport of reactant from the bulk electrolyte to the surface and the product moving in the opposite direction. Under a mass transfer-controlled condition, the slower mass transfer compared with the electron transfer results in the incapability to replenish the consumed reactant and eliminate the accumulated product. In the absence of convection, the thickness of the diffusion layer grows over time and the current continuously decays, but in a convective system, it quickly reaches the steady-state value.

To study fast reaction kinetics, various methods can be used to control and increase the mass transfer rate, such as the Rotating-Disk-Electrode (RDE) and the Ultramicroelectrode (UME). RDE is a powerful and widely-used electroanalytical tool in electrochemical studies, which controls hydrodynamic

environment and generates well-defined mass transfer conditions for electrode kinetics investigations. It consists of a conductive disk, typically made of noble metal or glassy carbon, and an inert polymer shroud. Since the electrode is rotating during the measurements, a mass transfer contribution is brought about by the forced convection. Once the reactant is exhausted by the electrochemical reactions at the surface, the limiting current density is reached, which represents the largest current density under the given mass transfer-controlled conditions. By solving the relevant convective-diffusion equation displayed in eq. 7 (for one dimension):³⁷

$$\frac{\partial C_j}{\partial t} = D_j \frac{\partial^2 C_j}{\partial y^2} - \nu_y \frac{\partial C_j}{\partial y} \quad (7)$$

where on the right-hand side, the first and the second terms represent diffusion and convection respectively, the concentration profile can be calculated and the limiting current density is then given by the Levich equation (eq. 8):³⁸

$$i_l = 0.62nFAD^{2/3}\omega^{2/3}\nu^{2/3}C^* \quad (8)$$

where D is the diffusion coefficient of the electroactive species, ω is the rotation rate of RDE, ν is the kinematic viscosity, and C^* is the bulk concentration of the electroactive species.

Understanding mass transfer is extremely important in electrochemical studies. Mass transfer causes concentration polarization, making the characteristics of the interface remarkably different from those in the bulk phase. With the development of numerical simulation and in-situ spectroscopy techniques in modern electrochemistry, we now have the opportunity to visualize the details of mass transfer with the necessary resolution. Notably, the ring electrode in the Rotating Ring-Disk electrode can be used as an in-situ sensor to examine the interfacial environment under well-defined mass transfer conditions, without any interference to the reaction process.

1.2.4 Electrolyte effect

The interfacial electrolyte is an important part of the electrochemical interface. Inert electrolyte species are involved in the electrochemical current flow as charge carriers to establish the conduction path in the solution. However, at the interface, due to the influence of the electric field and the heterogeneous electron transfer process, electrolyte species in close vicinity of the electrode may interact with the electroactive species and the electrode itself. Although electro-inactive by themselves, they might hence impact the electron transfer in an implicit way.³⁹ An idealized single electron transfer process comprises mass transfer of the reactant, adsorption, electron transfer, desorption, and mass transfer of the product (outer sphere reactions taking place without adsorption and

desorption). However, in practical studies, the reactant and/or the product might undergo chemical reactions with the electrolyte species before or after the electrochemical reactions, resulting in complex reaction pathways e.g. CE reaction (with a preceding chemical reaction), EC reaction (with a subsequent chemical reaction). The hydrolysis of the hydrated cation, the interaction of the cation with the reaction intermediate, the homogeneous reactions of anions, and the resulting variation of interfacial pH all impose profound influences on the reaction process, which will be elaborated and demonstrated in the next few chapters.

1.3 CO₂ reduction reaction

Carbon is the pivotal element of all life on Earth. It is stored and circulated within the atmosphere, the ocean, the ecosystem, and the lithosphere, during thousands of years, which forms the Natural Carbon Cycle (NCC).⁴⁰ CO₂ is released into the atmosphere by the respiration of plants, consumption of organic carbon by animals and decomposition of organic matter by microorganisms, while it is solidified and stored as organic carbon *via* photosynthesis of plants and as lithosphere in the long term. Alternatively, the scientific community has been dedicated to the development of the anthropogenic carbon cycle (ACC), which is based on the capture, fixation, and temporary storage of CO₂ followed by the conversion of CO₂ into commercial products. Compared with NCC, the anthropogenic carbon cycle can be industrially scaled up to produce sustainable, renewable, and environmental-friendly carbon sources. Here, CO₂ is treated as a valuable industrial C1 raw material to produce valuable products, instead of a greenhouse gas that does harm to the global environment.

CO₂ is a linear and centrosymmetric molecule, with two C=O bonds which require 800 kJ mol⁻¹ to dissociate. This endothermic CO₂ reduction reaction can be powered by biomass energy,⁴¹ photon energy,⁴² thermal energy,⁴³ and electricity.⁴⁴ In comparison with other techniques, electrochemical CO₂ reduction reaction (CO₂RR) in aqueous solution is simply carried out through the passage of a current under a moderate reaction condition. Importantly, when coupled with renewable energy e.g. solar energy, wind energy, and hydropower, CO₂RR produces carbonaceous feedstock with zero carbon emission. The early examples of CO₂RR dates back to 1900s,⁴⁵⁻⁴⁶ in which CO₂ was reduced on mercury electrode, followed by enlightening studies by Hori et al of CO₂RR on Cu electrode.⁴⁷⁻⁴⁸ Since then, investigations have been focused on the development of a highly efficient and selective electrocatalyst system. In the past decade, impressive breakthroughs have been made in the exploration of selective reaction pathways for C₂₊ products,⁴⁹⁻⁵¹ which is based on the understanding of the CO₂ activation mechanism, guided by the Sabatier principle. With the progressive advancement of nanoscience, material science, and computer science,

great progress has been achieved in catalyst design,^{39,52} reaction understanding,⁴⁴ electrolyzer construction²⁶ and industrialization.^{35,53} However, there are still challenges, including improving the current density and the catalyst durability to a real industrial scale. Therefore, further innovation is needed in catalyst selectivity, activity, and cost-effectiveness, as well as enhancements in energy efficiency and system stability for the transition from lab setting to industrial application. CO2RR is a promising technology to contribute to environmental concerns and energy demands to realize carbon neutrality. The future should be targeting to devise a sustainable and highly efficient electrochemical system to convert CO₂ into other value-added products with an acceptable cost and a simple downstream treatment.

1.4 H₂ evolution reaction

The current energy landscape still highly counts on fossil fuels, which imposes significant worldwide challenges, such as greenhouse gas emissions and energy crisis. The move to renewables is picking up momentum, among which green hydrogen, as a clean energy carrier, is a promising alternative to fossil fuels due to its high energy density and zero-emission character. Despite the abundance of hydrogen elements on Earth, it is combined in various compounds, making its production energy demanding. Unfortunately, the principal and least expensive technique of hydrogen production still relies on reforming fossil fuels or other multi-carbon compounds, due to the low energy cost, although it causes massive pollutant emissions (i.e. CO₂) and needs further purification of hydrogen from other by-products e.g. CO₂ and CO. Alternatively, hydrogen can also be produced by water electrolysis,⁵⁴ thermochemical process,⁵⁵ photoconversion,⁵⁶ or photobiological processes,⁵⁷ from which water electrolysis is the most affordable, pollution free, and efficient. More importantly, when coupled with electricity derived from renewable sources such as solar and wind power, water electrolysis is highly sustainable with a minimal carbon footprint. This is in alignment with the goal of a low-carbon economy, where green hydrogen could play a critical role in decarbonizing the chemical industry, in energy storage and serve as a power source for various applications.

Hydrogen Evolution Reaction (HER) is a critical component of water splitting, laying the cornerstone of electrocatalysis. The efficiency of the HER is highly dependent on the electrode material. Design, synthesis, and analysis of these HER electrode materials have been the subject of extensive research.⁵⁸⁻⁶⁰ Pt-group catalysts are noted for their high activity and stability for HER, but their scarcity and high cost largely impede their application⁶¹⁻⁶². Recent advancements have focused on the exploration of alternative non-precious metal catalysts, including transition metal sulfides, phosphides, and selenides such as iron,

cobalt, and nickel-based complexes.⁶³⁻⁶⁵ These materials offer an excellent combination of good activity and affordability, which is necessary for large-scale implementation. Since HER is a typical inner sphere (catalytic) reaction that is highly surface sensitive, the performance of the catalyst is heavily influenced by the electrode surface properties e.g. such as electronic structure, surface morphology, and interaction with the electrolyte. Tuning the structure of the catalyst enhances HER performance by providing more active sites,^{60,66} while doping catalysts with other elements introduce local heterostructures that can modify the electronic structure, thereby improving the catalytic activity.^{63,67-68}

Elucidating complex reaction mechanisms is of great importance for HER, especially under alkaline conditions where the kinetics are slower compared with acidic media. Studies have demonstrated the prominent influence of the electrolyte species.⁶⁹⁻⁷⁰ Disclosing the role of these electro-inactive species in the interface and their interaction with the reactant and the reaction intermediates during HER can make an eminent contribution to the fundamental understanding of HER. Besides, reaction parameters such as the adsorption energies of certain intermediates and the potential dependence of the reaction rate have been investigated as interfacial descriptors of the HER, offering valuable insights and principles for the rational design of electrocatalysts.^{62,71-72}

The integration of the HER process with renewable energy is a viable path to produce sustainable hydrogen. The declining costs of renewable electricity render water electrolysis an attractive candidate for industrial hydrogen production. However, challenges remain in improving the efficiency and reducing the cost of electrolyzers. Coupling electrochemistry with the advanced techniques such as in-situ spectroscopies, molecular simulations, can assist in progressing the understanding of the interfacial environment of HER at a molecular level, eventually contributing to a more sustainable, efficient and affordable production of green hydrogen.

1.5 Scope of this thesis

During the heterogeneous electron transfer process, the electrochemical interface provides a non-uniform environment for the reactive species, in which the inert electrolyte species are part of the molecular micro-environment and have a profound influence on the reaction process. Interfacial pH plays a decisive role among these interfacial parameters. The main goal of this thesis is to develop an in-depth understanding of the interplay between the interfacial pH and other electrolyte effects and evaluate its impact on CO₂RR and HER.

In **Chapter 2**, we devise a reliable and highly sensitive interfacial pH sensor using RRDE coupled with a voltammetric redox couple, to visualize the variation of interfacial pH during HER under well-defined mass transport conditions. Protic anions are shown to impact the

interfacial pH through homogeneous reactions with the electrogenerated OH^- , i.e. the buffering acid-base reaction. **Chapter 3** demonstrates the influence of CO_2 , HCO_3^- , the alkali cations, and mass transport on the interfacial pH during CO2RR. We find that the buffering capacity increases in the order $\text{Li}^+ < \text{Na}^+ < \text{K}^+ < \text{Rb}^+ < \text{Cs}^+ < \text{HCO}_3^-$. The interfacial pH in turn impacts the speciation near the interface, the electrochemical reaction, and the competition between CO2RR and HER. Inspired by these results, in **Chapter 4**, CO2RR is carried out in mildly acidic media, where the CO2RR is capable of competing with proton reduction under proper conditions. By adjusting the interfacial environment *via* the protic anion HSO_4^- , the weakly hydrated alkali cations e.g. Cs^+ , and mass transfer, the Faradaic Efficiency of CO2RR can reach over 80%, even under acid conditions. Finally, **Chapter 5** demonstrates the impact of HSO_4^- and the weakly hydrated alkali cations on the steady state current of HER. The limiting current density increases with the concentration of these inert electrolyte species. The linear variation of the Koutecký–Levich Slope with respect to the concentration of these species is revealed, out of which valuable thermodynamic information is extracted through mathematical analysis.

References

- (1)Pancaldi, G., Electricity and life. Volta's path to the battery. *Historical studies in the physical and biological sciences* **1990**, *21* (1), 123-160.
- (2)de Levie, R., The electrolysis of water. *Journal of Electroanalytical Chemistry* **1999**, *476* (1), 92-93.
- (3)Zhang, C.; Wei, Y. L.; Cao, P. F.; Lin, M. C., Energy storage system: Current studies on batteries and power condition system. *Renewable & Sustainable Energy Reviews* **2018**, *82*, 3091-3106.
- (4)Noël, T.; Cao, Y. R.; Laudadio, G., The Fundamentals Behind the Use of Flow Reactors in Electrochemistry. *Accounts of Chemical Research* **2019**, *52* (10), 2858-2869.
- (5)Shih, A. J.; Monteiro, M. C. O.; Dattila, F.; Pavesi, D.; Philips, M.; da Silva, A. H. M.; Vos, R. E.; Ojha, K.; Park, S.; van der Heijden, O.; Marcandalli, G.; Goyal, A.; Villalba, M.; Chen, X.; Gunasooriya, G. T. K. K.; McCrum, I.; Mom, R.; López, N.; Koper, M. T. M., Water electrolysis. *Nature Reviews Methods Primers* **2022**, *2* (1), 84.
- (6)Esmaily, M.; Svensson, J. E.; Fajardo, S.; Birbilis, N.; Frankel, G. S.; Virtanen, S.; Arrabal, R.; Thomas, S.; Johansson, L. G., Fundamentals and advances in magnesium alloy corrosion. *Progress in Materials Science* **2017**, *89*, 92-193.
- (7)Vasudevan, S.; Oturan, M. A., Electrochemistry: as cause and cure in water pollution-an overview. *Environmental Chemistry Letters* **2014**, *12* (1), 97-108.
- (8)Lubin, A. A.; Plaxco, K. W., Folding-Based Electrochemical Biosensors: The Case for Responsive Nucleic Acid Architectures. *Accounts of Chemical Research* **2010**, *43* (4), 496-505.

(9)Bard, A. J.; Faulkner, L. R.; White, H. S., *Electrochemical methods: fundamentals and applications*. John Wiley & Sons: 2022.

(10)Attias, R.; Salama, M.; Hirsch, B.; Goffer, Y.; Aurbach, D., Anode-Electrolyte Interfaces in Secondary Magnesium Batteries. *Joule* **2019**, 3 (1), 27-52.

(11)Stamenkovic, V. R.; Strmcnik, D.; Lopes, P. P.; Markovic, N. M., Energy and fuels from electrochemical interfaces. *Nature Materials* **2017**, 16 (1), 57-69.

(12)Grahame, D. C., The electrical double layer and the theory of electrocapillarity. *Chemical Reviews* **1947**, 41 (3), 441-501.

(13)Chen, X.; Flores, S. C.; Lim, S. M.; Zhang, Y. J.; Yang, T. L.; Kherb, J.; Cremer, P. S., Specific Anion Effects on Water Structure Adjacent to Protein Monolayers. *Langmuir* **2010**, 26 (21), 16447-16454.

(14)Wang, J.; Bard, A. J., Direct atomic force microscopic determination of surface charge at the gold/electrolyte interface - The inadequacy of classical GCS theory in describing the double-layer charge distribution. *Journal of Physical Chemistry B* **2001**, 105 (22), 5217-5222.

(15)Bonciocat, N.; Anghel, D. F.; Saito, S.; Iovescu, A.; Baran, A., An electrochemical model for interpreting the counterion effect of cationic surfactants in interaction with charged polymers. I - Adsorption isotherm. Counterion effect upon the adsorption process. *Revue Roumaine De Chimie* **2003**, 48 (6), 425-431.

(16)Wang, X. X.; Liu, J.; Zhang, Z. H.; Xiang, Q.; Zhang, J. J.; Chen, L.; Xie, H. J., Mechanism for corrosion inhibition of pure iron in 1 M HCl by Raujella Fujisana: Experimental, GC-MS, DFT, VASP and solid-liquid modeling studies. *Industrial Crops and Products* **2024**, 207, 16.

(17)Wang, Y. G.; Song, Y. F.; Xia, Y. Y., Electrochemical capacitors: mechanism, materials, systems, characterization and applications. *Chemical Society Reviews* **2016**, 45 (21), 5925-5950.

(18)Frackowiak, E.; Béguin, F., Carbon materials for the electrochemical storage of energy in capacitors. *Carbon* **2001**, 39 (6), 937-950.

(19)Simon, P.; Gogotsi, Y., Materials for electrochemical capacitors. *Nature Materials* **2008**, 7 (11), 845-854.

(20)Trasatti, S., Work function, electronegativity, and electrochemical behaviour of metals: III. Electrolytic hydrogen evolution in acid solutions. *Journal of Electroanalytical Chemistry and Interfacial Electrochemistry* **1972**, 39 (1), 163-184.

(21)Gerischer, H.; Tobias, C. W., *Advances in Electrochemistry and Electrochemical Engineering*. Wiley: 1977.

(22)Nørskov, J. K.; Bligaard, T.; Logadottir, A.; Kitchin, J.; Chen, J. G.; Pandelov, S.; Stimming, U., Trends in the exchange current for hydrogen evolution. *Journal of The Electrochemical Society* **2005**, 152 (3), J23.

(23)Conway, B.; Beatty, E.; DeMaine, P., Electrochemical kinetics of hydrogen evolution at copper-nickel alloys. Relation to electronic properties of the electrodes. *Electrochimica Acta* **1962**, 7 (1), 39-54.

(24)Sabatier, P., Hydrogénations et déshydrogénations par catalyse. *Berichte der deutschen chemischen Gesellschaft* **1911**, 44 (3), 1984-2001.

(25)Vasileff, A.; Xu, C. C.; Jiao, Y.; Zheng, Y.; Qiao, S. Z., Surface and Interface Engineering in Copper-Based Bimetallic Materials for Selective CO₂ Electroreduction. *Chem* **2018**, 4 (8), 1809-1831.

(26)Jin, S.; Hao, Z. M.; Zhang, K.; Yan, Z. H.; Chen, J., Advances and Challenges for the Electrochemical Reduction of CO₂ to CO: From Fundamentals to Industrialization. *Angewandte Chemie-International Edition* **2021**, 60 (38), 20627-20648.

(27)Huang, J. F.; Mensi, M.; Oveisi, E.; Mantella, V.; Buonsanti, R., Structural Sensitivities in Bimetallic Catalysts for Electrochemical CO₂ Reduction Revealed by Ag-Cu Nanodimers. *Journal of the American Chemical Society* **2019**, 141 (6), 2490-2499.

(28)Pan, Y.; Lin, R.; Chen, Y. J.; Liu, S. J.; Zhu, W.; Cao, X.; Chen, W. X.; Wu, K. L.; Cheong, W. C.; Wang, Y.; Zheng, L. R.; Luo, J.; Lin, Y.; Liu, Y. Q.; Liu, C. G.; Li, J.; Lu, Q.; Chen, X.; Wang, D. S.; Peng, Q.; Chen, C.; Li, Y. D., Design of Single-Atom Co-N₅Catalytic Site: A Robust Electrocatalyst for CO₂Reduction with Nearly 100% CO Selectivity and Remarkable Stability. *Journal of the American Chemical Society* **2018**, 140 (12), 4218-4221.

(29)Varela, A. S.; Sahraie, N. R.; Steinberg, J.; Ju, W.; Oh, H. S.; Strasser, P., Metal-Doped Nitrogenated Carbon as an Efficient Catalyst for Direct CO₂ Electroreduction to CO and Hydrocarbons. *Angewandte Chemie-International Edition* **2015**, 54 (37), 10758-10762.

(30)Chen, H.; Liang, X.; Liu, Y. P.; Ai, X.; Asefa, T.; Zou, X. X., Active Site Engineering in Porous Electrocatalysts. *Advanced Materials* **2020**, 32 (44).

(31)Loidice, A.; Lobaccaro, P.; Kamali, E. A.; Thao, T.; Huang, B. H.; Ager, J. W.; Buonsanti, R., Tailoring Copper Nanocrystals towards C₂ Products in Electrochemical CO₂ Reduction. *Angewandte Chemie-International Edition* **2016**, 55 (19), 5789-5792.

(32)Liu, S. B.; Tao, H. B.; Zeng, L.; Liu, Q.; Xu, Z. G.; Liu, Q. X.; Luo, J. L., Shape-Dependent Electrocatalytic Reduction of CO₂ to CO on Triangular Silver Nanoplates. *Journal of the American Chemical Society* **2017**, 139 (6), 2160-2163.

(33)Banerjee, S.; Han, X.; Thoi, V. S., Modulating the Electrode-Electrolyte Interface with Cationic Surfactants in Carbon Dioxide Reduction. *Acs Catalysis* **2019**, 9 (6), 5631-5637.

(34)Banerjee, S.; Zhang, Z. Q.; Hall, A. S.; Thoi, V. S., Surfactant Perturbation of Cation Interactions at the Electrode-Electrolyte Interface in Carbon Dioxide Reduction. *Acs Catalysis* **2020**, 10 (17), 9907-9914.

(35)Möller, T.; Ju, W.; Bagger, A.; Wang, X. L.; Luo, F.; Thanh, T. N.; Varela, A. S.; Rossmeisl, J.; Strasser, P., Efficient CO₂ to CO electrolysis on solid Ni-N-C catalysts at industrial current densities. *Energy & Environmental Science* **2019**, 12 (2), 640-647.

(36)Pan, F. P.; Zhang, H. G.; Liu, K. X.; Cullen, D.; More, K.; Wang, M. Y.; Feng, Z. X.; Wang, G. F.; Wu, G.; Li, Y., Unveiling Active Sites of CO₂ Reduction on Nitrogen-Coordinated and Atomically Dispersed Iron

and Cobalt Catalysts. *Acs Catalysis* **2018**, *8* (4), 3116-3122.

(37)Albery, W. J.; Calvo, E. J., Ring–disc electrodes. Part 21.—pH measurement with the ring. *Journal of the Chemical Society, Faraday Transactions 1: Physical Chemistry in Condensed Phases* **1983**, *79* (11), 2583-2596.

(38)Levich, V. G.; Tobias, C. W., Physicochemical hydrodynamics. *Journal of The Electrochemical Society* **1963**, *110* (11), 251C.

(39)Gao, D. F.; Arán-Ais, R. M.; Jeon, H. S.; Roldan Cuenya, B., Rational catalyst and electrolyte design for CO₂ electroreduction towards multicarbon products. *Nature Catalysis* **2019**, *2* (3), 198-210.

(40)Wang, Y., *Electrocatalysis in Balancing the Natural Carbon Cycle*. John Wiley & Sons: 2021.

(41)Sheldon, R. A.; Brady, D., Green Chemistry, Biocatalysis, and the Chemical Industry of the Future. *Chemsuschem* **2022**, *15* (9), 20.

(42)Ji, S. F.; Qu, Y.; Wang, T.; Chen, Y. J.; Wang, G. F.; Li, X.; Dong, J. C.; Chen, Q. Y.; Zhang, W. Y.; Zhang, Z. D.; Liang, S. Y.; Yu, R.; Wang, Y.; Wang, D. S.; Li, Y. D., Rare-Earth Single Erbium Atoms for Enhanced Photocatalytic CO₂ Reduction. *Angewandte Chemie-International Edition* **2020**, *59* (26), 10651-10657.

(43)Wei, Z. X.; Zhu, Y. T.; Liu, J. Y.; Zhang, Z. C.; Hu, W. P.; Xu, H.; Feng, Y. Z.; Ma, J. M., Recent advance in single-atom catalysis. *Rare Metals* **2021**, *40* (4), 767-789.

(44)Wagner, A.; Sahm, C. D.; Reisner, E., Towards molecular understanding of local chemical environment effects in electro- and photocatalytic CO₂ reduction. *Nature Catalysis* **2020**, *3* (10), 775-786.

(45)Royer, E., Reduction of Carbonic Acid into Formic Acid, *CR. Acad. Aci* **1870**, *70*, 731-735.

(46)Rysselberghe, P. v., Polarographic Reduction of Carbon Dioxide. II. Polymerization and Adsorption at the Dropping Mercury Cathode1. *Journal of the American Chemical Society* **1946**, *68* (10), 2047-2049.

(47)Hori, Y.; Kikuchi, K.; Suzuki, S., Production of CO and CH₄ in electrochemical reduction of CO₂ at metal electrodes in aqueous hydrogencarbonate solution. *Chem. lett.* **1985**, *14* (11), 1695-1698.

(48)Hori, Y.; Murata, A.; Takahashi, R., Formation of hydrocarbons in the electrochemical reduction of carbon dioxide at a copper electrode in aqueous solution. *J. Chem. Soc., Faraday Trans. 1* **1989**, *85* (8), 2309-2326.

(49)Jiang, K.; Siahrostami, S.; Zheng, T. T.; Hu, Y. F.; Hwang, S.; Stavitski, E.; Peng, Y. D.; Dynes, J.; Gangisetty, M.; Su, D.; Attenkofer, K.; Wang, H. T., Isolated Ni single atoms in graphene nanosheets for high-performance CO₂ reduction. *Energy & Environmental Science* **2018**, *11* (4), 893-903.

(50)Li, F. W.; Thevenon, A.; Rosas-Hernandez, A.; Wang, Z. Y.; Li, Y. L.; Gabardo, C. M.; Ozden, A.; Dinh, C. T.; Li, J.; Wang, Y. H.; Edwards, J. P.; Xu, Y.; McCallum, C.; Tao, L. Z.; Liang, Z. Q.; Luo, M. C.; Wang, X.; Li, H. H.; O'Brien, C. P.; Tan, C. S.; Nam, D. H.; Quintero-Bermudez, R.; Zhuang, T. T.; Li, Y. G. C.; Han, Z. J.; Britt, R. D.; Sinton, D.; Agapie, T.; Peters, J. C.; Sargent, E. H., Molecular tuning of CO₂-to-ethylene conversion. *Nature* **2020**, *577* (7791), 509-.

(51)Zhang, S.; Fan, Q.; Xia, R.; Meyer, T. J., CO₂ Reduction: From Homogeneous to Heterogeneous Electrocatalysis. *Accounts of Chemical Research* **2020**, *53* (1), 255-264.

(52)Chen, Y. J.; Ji, S. F.; Chen, C.; Peng, Q.; Wang, D. S.; Li, Y. D., Single-Atom Catalysts: Synthetic Strategies and Electrochemical Applications. *Joule* **2018**, *2* (7), 1242-1264.

(53)Yang, H. P.; Wu, Y.; Li, G. D.; Lin, Q.; Hu, Q.; Zhang, Q. L.; Liu, J. H.; He, C., Scalable Production of Efficient Single-Atom Copper Decorated Carbon Membranes for CO₂ Electroreduction to Methanol. *Journal of the American Chemical Society* **2019**, *141* (32), 12717-12723.

(54)You, B.; Sun, Y. J., Innovative Strategies for Electrocatalytic Water Splitting. *Accounts of Chemical Research* **2018**, *51* (7), 1571-1580.

(55)Xue, Y. P.; Zhao, G. C.; Yang, R. Y.; Chu, F.; Chen, J.; Wang, L.; Huang, X. B., 2D metal-organic framework-based materials for electrocatalytic, photocatalytic and thermocatalytic applications. *Nanoscale* **2021**, *13* (7), 3911-3936.

(56)Wang, X. C.; Maeda, K.; Thomas, A.; Takanabe, K.; Xin, G.; Carlsson, J. M.; Domen, K.; Antonietti, M., A metal-free polymeric photocatalyst for hydrogen production from water under visible light. *Nature Materials* **2009**, *8* (1), 76-80.

(57)Lee, S. H.; Choi, D. S.; Kuk, S. K.; Park, C. B., Photobiocatalysis: Activating Redox Enzymes by Direct or Indirect Transfer of Photoinduced Electrons. *Angewandte Chemie-International Edition* **2018**, *57* (27), 7958-7985.

(58)Eftekhari, A., Electrocatalysts for hydrogen evolution reaction. *International Journal of Hydrogen Energy* **2017**, *42* (16), 11053-11077.

(59)Zheng, Y.; Jiao, Y.; Zhu, Y. H.; Li, L. H.; Han, Y.; Chen, Y.; Jaroniec, M.; Qiao, S. Z., High Electrocatalytic Hydrogen Evolution Activity of an Anomalous Ruthenium Catalyst. *Journal of the American Chemical Society* **2016**, *138* (49), 16174-16181.

(60)Deng, J.; Ren, P. J.; Deng, D. H.; Yu, L.; Yang, F.; Bao, X. H., Highly active and durable non-precious-metal catalysts encapsulated in carbon nanotubes for hydrogen evolution reaction. *Energy & Environmental Science* **2014**, *7* (6), 1919-1923.

(61)Liu, D. B.; Li, X. Y.; Chen, S. M.; Yang, H.; Wang, C. D.; Wu, C. Q.; Haleem, Y. A.; Duan, S.; Lu, J. L.; Ge, B. H.; Ajayan, P. M.; Luo, Y.; Jiang, J.; Song, L., Atomically dispersed platinum supported on curved carbon supports for efficient electrocatalytic hydrogen evolution. *Nature Energy* **2019**, *4* (6), 512-518.

(62)Zheng, J.; Sheng, W. C.; Zhuang, Z. B.; Xu, B. J.; Yan, Y. S., Universal dependence of hydrogen oxidation and evolution reaction activity of platinum-group metals on pH and hydrogen binding energy. *Science Advances* **2016**, *2* (3), 8.

(63)Zhang, J.; Wang, T.; Pohl, D.; Rellinghaus, B.; Dong, R. H.; Liu, S. H.; Zhuang, X. D.; Feng, X. L., Interface Engineering of MoS₂/Ni₃S₂ Heterostructures for Highly Enhanced Electrochemical Overall-Water-Splitting Activity. *Angewandte Chemie-International Edition* **2016**, *55* (23), 6702-6707.

(64)Wang, J.; Xu, F.; Jin, H. Y.; Chen, Y. Q.; Wang, Y., Non-Noble Metal-based Carbon Composites in 21

Hydrogen Evolution Reaction: Fundamentals to Applications. *Advanced Materials* **2017**, *29* (14), 35.

(65)Sun, H. M.; Yan, Z. H.; Liu, F. M.; Xu, W. C.; Cheng, F. Y.; Chen, J., Self-Supported Transition-Metal-Based Electrocatalysts for Hydrogen and Oxygen Evolution. *Advanced Materials* **2020**, *32* (3), 18.

(66)Chen, C.; Kang, Y. J.; Huo, Z. Y.; Zhu, Z. W.; Huang, W. Y.; Xin, H. L. L.; Snyder, J. D.; Li, D. G.; Herron, J. A.; Mavrikakis, M.; Chi, M. F.; More, K. L.; Li, Y. D.; Markovic, N. M.; Somorjai, G. A.; Yang, P. D.; Stamenkovic, V. R., Highly Crystalline Multimetallic Nanoframes with Three-Dimensional Electrocatalytic Surfaces. *Science* **2014**, *343* (6177), 1339-1343.

(67)Wang, D. Y.; Gong, M.; Chou, H. L.; Pan, C. J.; Chen, H. A.; Wu, Y. P.; Lin, M. C.; Guan, M. Y.; Yang, J.; Chen, C. W.; Wang, Y. L.; Hwang, B. J.; Chen, C. C.; Dai, H. J., Highly Active and Stable Hybrid Catalyst of Cobalt-Doped FeS₂ Nanosheets-Carbon Nanotubes for Hydrogen Evolution Reaction. *Journal of the American Chemical Society* **2015**, *137* (4), 1587-1592.

(68)Deng, J.; Li, H. B.; Xiao, J. P.; Tu, Y. C.; Deng, D. H.; Yang, H. X.; Tian, H. F.; Li, J. Q.; Ren, P. J.; Bao, X. H., Triggering the electrocatalytic hydrogen evolution activity of the inert two-dimensional MoS₂ surface via single-atom metal doping. *Energy & Environmental Science* **2015**, *8* (5), 1594-1601.

(69)Kamat, G. A.; Zeledón, J. A. Z.; Gunasooriya, G.; Dull, S. M.; Perryman, J. T.; Norskov, J. K.; Stevens, M. B.; Jaramillo, T. F., Acid anion electrolyte effects on platinum for oxygen and hydrogen electrocatalysis. *Communications Chemistry* **2022**, *5* (1), 10.

(70)Merrill, M. D.; Logan, B. E., Electrolyte effects on hydrogen evolution and solution resistance in microbial electrolysis cells. *Journal of Power Sources* **2009**, *191* (2), 203-208.

(71)Kibsgaard, J.; Tsai, C.; Chan, K.; Benck, J. D.; Norskov, J. K.; Abild-Pedersen, F.; Jaramillo, T. F., Designing an improved transition metal phosphide catalyst for hydrogen evolution using experimental and theoretical trends. *Energy & Environmental Science* **2015**, *8* (10), 3022-3029.

(72)Durst, J.; Siebel, A.; Simon, C.; Hasché, F.; Herranz, J.; Gasteiger, H. A., New insights into the electrochemical hydrogen oxidation and evolution reaction mechanism. *Energy & Environmental Science* **2014**, *7* (7), 2255-2260.



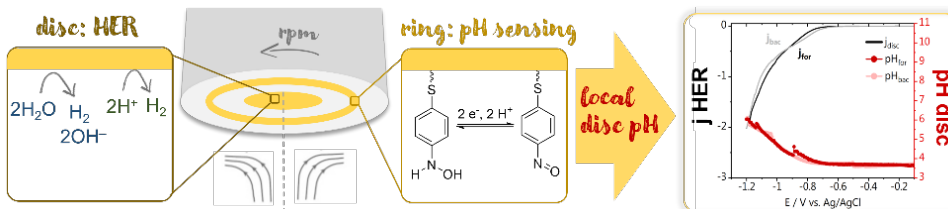
Chapter 2

Interfacial pH measurements using a Rotating Ring-Disc Electrode with a voltammetric pH sensor



Abstract

Electrochemical reactions in which H^+ or OH^- ions are produced or consumed, affect the pH near the electrode surface. Probing the pH locally is therefore highly desired to understand and model the reaction environment under operando conditions. We carried out interfacial pH measurements under mass transport control using a rotating ring-disc electrode (RRDE) coupled with our recently developed voltammetric pH sensor. The interfacial disc pH is detected by functionalizing the gold ring with a hydroxylaminothiophenol (4-HATP)/4-nitrosothiophenol (4-NSTP) redox couple. As protons only have to interact with a monolayer containing the 4-HATP/4-NSTP, the sensitivity and time resolution that can be achieved are superior to potentiometric sensors. We used hydrogen evolution as a model reaction and performed measurements in buffered and unbuffered electrolytes. The effects of the current density, potential, the buffer capacity of the electrolyte and rotation rate on the local pH were investigated. This work shows a reliable and sensitive method for accurately probing the reaction environment under well-defined mass transport conditions, over a wide pH range.



This chapter is based on Monteiro, M. C. O.; Liu, X.; Hagedoorn, B. J. L.; Snabilié, D. D.; Koper, M. T. M., Interfacial pH Measurements Using a Rotating Ring-Disc Electrode with a Voltammetric pH Sensor. *ChemElectroChem* 2021, 9 (1), e202101223.

2.1 Introduction

Electrochemical reactions that consume/produce protons or hydroxyl ions can generate a pH gradient between the electrode surface and the bulk of the electrolyte. In general, the value of the local pH developed at the surface is a function of the current drawn, the electrolyte composition, and the mass transport conditions.^[1] It has been shown that the (local) electrolyte pH plays a significant role in various reactions, such as hydrogen evolution^[2] (HER), CO₂ reduction^[3], oxygen evolution^[4] and reduction^[5], among others. Therefore, it is highly desired to probe the pH gradient near the surface during these electrochemical reactions, with high sensitivity, and with good time and spatial resolution. We have recently reviewed the main techniques available for performing local pH measurements^[1], the most frequently used ones being Scanning Electrochemical Microscopy (SECM)^[6–8], Scanning Ion Conductance Microscopy (SICM)^[9,10], Scanning Ion Selective Electrode (SIET), Rotating Ring-Disc Electrode (RRDE)^[11–14], confocal fluorescence scanning microscopy^[15], infra-red^[16,17] and Raman spectroscopy.^[18] Among these, RRDE is the only technique that allows for measurements to be performed under well-defined mass transport conditions, at the expense of the in-plane spatial resolution. Firstly introduced by Albery and Calvo^[19–21], pH measurements using RRDE consist of a reaction taking place at the disc electrode and the detection of the proton concentration during the course of this reaction by a pH sensing material at the ring electrode. Due to the electrode geometry and rotation, the flow of species going from the disc to the ring is described by a convective-diffusion equation. This allows the interfacial pH observed at the ring electrode to be directly converted into the pH at the surface of the disc electrode. The advantage is that the detection by the ring electrode does not affect the reactions taking place on the disc electrode. The analytical solution derived by Albery and Calvo^[19–21] was recently further developed by Yokoyama et al.^[22] by including the autoprotolysis of water in the description, which allows for determining the interfacial disc pH more accurately in a wider pH range. A few works on interfacial pH measurements with RRDE have been reported, however mainly potentiometric pH sensors were employed, the most common being iridium oxide (IrO_x).^[11,13,14] The ring electrode is normally modified with an IrO_x film and the pH at the disc is determined based on the Nernstian open circuit potential (OCP) response of the ring. A major drawback of using IrO_x is that the stability and time resolution depend, for example, on the film thickness and pH.^[23,24] Besides IrO_x, certain reactions on bare metal surfaces have also been used to estimate changes in local pH. Figueiredo et al.^[12] used shifts in the equilibrium potential of the hydrogen evolution reaction on a Pt ring to estimate the disc pH during ethanol oxidation. Zhang et al. used the CO oxidation reaction on a gold ring to probe the disc pH during CO₂ reduction to CO on gold.^[13] However, it is known that the sensitivity

and accuracy of these measurements can be highly compromised by the reaction environment, as both HER and CO oxidation have shown to be affected, i.e. by the cation^[25–27], surface structure^[28,29] and pH.^[30,31] Also, buffering species in the electrolyte are not always taken into account when converting the pH measured at the ring to the local disc pH, which may lead to an overestimation of the local alkalinity. Besides that, based on the analytical description of Yokoyama et al.^[22], changes of the local disc pH may correspond to an order of magnitude smaller changes in the ring pH based on detection efficiency and buffering, especially in solutions far from neutral pH. Therefore, a more sensitive pH sensor for RRDE is desired, and in fact necessary, for performing accurate interfacial pH measurements with this technique.

In this work, we have assessed the feasibility of using our previously developed voltammetric pH sensor in the RRDE configuration. The sensor consists of a self-assembled monolayer on gold, and was previously used for local pH measurements in the diffusion layer with SECM.^[32,33] The pH response is based on the voltammetry of the hydroxylaminothiophenol (4-HATP)/4-nitrosothiophenol (4-NSTP) redox couple, specifically the Nernstian shift of the oxidation reaction mid-peak potential. We show here that the 4-HATP/4-NSTP voltammetric response is not affected by the electrode rotation, and that this redox couple can be used in a RRDE system. We employed it to probe the interfacial disc pH during hydrogen evolution in buffered and unbuffered electrolytes at mildly acidic pH. With the high sensitivity and time resolution of this voltammetric sensor, we measured the interfacial disc pH during cyclic voltammetry, chronoamperometry and chronopotentiometry experiments, and also determined the rotation rate required to minimize interfacial pH changes in the electrolytes studied. The application of this sensitive and reliable pH sensor for RRDE pH measurements presents an alternative to commonly used potentiometric sensors, and a step forward to more accurately probing the reaction environment under well-defined mass transport conditions.

2.2 Experimental Section

Materials. All glassware used was cleaned by immersion in a potassium permanganate solution overnight (1 g/L KMnO₄ dissolved in 0.5 M H₂SO₄), followed by immersion in dilute piranha. The glassware was further boiled in ultrapure water at least five times. The electrolytes used in this work, KH₂PO₄ (Alfa Aesar, dried, 99.99 %) and K₂SO₄ (Alfa Aesar, Puratronic, 99.997 %, metals basis), were adjusted to pH 3-5 by addition of appropriate amounts of H₂SO₄ (Merck, Suprapur, 96%) or H₃PO₄ (ortho-Phosphoric acid 85%, Suprapur®, Merck).

pH sensor fabrication and characterization. A gold ring electrode (E6R1PK tip, Pine Research Instrumentation) was used in this work, together with a gold disc (diameter = 5 mm, Pine Research Instrumentation). Prior to experiments, the ring and the disc (Pine Research Instrumentation) were polished with a polycrystalline diamond suspension of 0.25 μm (MetaDi, Buehler) and then sonicated (Bandelin Sonorex RK 52H) in ultrapure water ($>18.2\text{ M}\Omega\text{ cm}$, Millipore Milli-Q) for 10 minutes.^[36] Before functionalization of the ring with the pH sensing monolayer, the ring and disc were characterized by recording the blank voltammetry between 0.1 and 1.75 V vs. RHE in argon saturated (6.0 purity, Linde) 0.1 M H_2SO_4 (Merck, Suprapur, 96%) in a one compartment electrochemical cell. A gold wire (0.5 mm diameter, MaTeck, 99.9%) was used as counter electrode and a reversible hydrogen electrode (RHE) as reference. The electrochemically active surface area (ECSA) of the disc was calculated based on the charge corresponding to the gold oxide reduction and a specific capacitance of 386 $\mu\text{C}/\text{cm}^2$.^[37] The gold ring electrode is modified by immersing it (without the disc inserted) into a 1 mM solution of 4-NTP (Merck, 80%) in ethanol for 15 minutes. The ring is then thoroughly rinsed with ethanol and water, and dried. The disc electrode is carefully inserted in the shaft, avoiding too much friction (which could damage the 4-NTP monolayer). The 4-NTP is then electrochemically reduced to 4-HATP in the working electrolyte ($\text{pH} \approx 4$) by cycling the ring from 0.3 to -0.43 V vs. Ag/AgCl (argon saturated, 100 mV s^{-1}). It is important to point out that the monolayer can be easily removed from the gold ring by polishing it with a polycrystalline diamond suspension of 0.25 μm . This can be done whenever necessary i.e. when the 4-HATP/4-NSTP signal is for some reason compromised. A decrease in signal can be caused e.g., by bubbles and loss of potential control during measurements. Considering how simple and fast the pH sensor synthesis is, it is advised to always have a fresh monolayer adsorbed onto the surface at the start of new experiments.

RRDE pH measurements. All electrochemical measurements were carried out using a BioLogic 2-channel potentiostat/galvanostat/ EIS (SP-300). The ring and disc electrodes were controlled simultaneously, by two different potentiostat channels. Two gold wires (0.5 mm diameter, MaTeck, 99.9%) were used as counter electrodes and a Ag/AgCl (low profile, BioLogic) as reference. Argon (6.0 purity, Linde) was purged through the solution for 20 minutes prior to the experiments. The argon flow was kept also during the experiments in order to avoid oxygen diffusing into the electrolyte. The ring cyclic voltammetry (CV) was constantly recorded at 200 mV/s while hydrogen evolution took place at the disc.

Calculating the local disc pH. The mid-peak potential (E_{peak}) of the 4-HATP oxidation to 4-NSTP was determined by fitting the forward scans with a Gaussian function containing a linear background. E_{peak} was then converted to the ring pH (pH_{ring}) using the calibration curve of the 4-HATP/4-NSTP from our previous work: $\text{pH}_{\text{ring}} = (0.341 - E_{\text{peak}})/0.057$.^[32] It is

important to point out that the ring open circuit potential (OCP) cannot be used to extract the ring pH, as the 4-NTP monolayer initially adsorbed to the gold is only partially converted to the 4-HATP/4-NSTP redox couple, yielding a convoluted OCP response. To calculate the interfacial disc pH (pH_{disc}), for an unbuffered electrolyte, we use Equation 1, from Yokoyama et al.^[22], which is an extension of the analytical solution of Albery and Calvo^[19,20], taking the autoprotolysis of water (Equation 2) into account.

$$c_{r,H^+} - c_{r,OH^-} = N_D(c_{d,H^+} - c_{d,OH^-}) + (1 - N_D)(c_{\infty,H^+} - c_{\infty,OH^-}) \quad (1)$$

$$K_W = c_{rt,H^+}c_{rt,OH^-} \quad (2)$$

c_{∞} represents the proton or OH^- concentration in the bulk and c_d , and c_r , the same at the disc and ring, respectively. The detection efficiency N_D is given by Equation S3 and S4 (see Supporting Information) and is only dependent on the geometrical parameters of the ring and disc electrode, see Figure S1. For the electrode used in this work $N_D = 0.23$. Figure S2 in the Supporting Information (SI) shows the theoretical relationships between pH_{Disc} and pH_{Ring} at various pH_{∞} , comparing Equation 1 (Yokoyama) and Equation S1 (Albery and Calvo) for an unbuffered electrolyte. It can be observed that not taking the

autoprotolysis of water into account can lead to over/underestimating the disc pH, depending on the bulk pH. Equation 1 was rewritten as follows and used to convert pH_{ring} to pH_{disc} .

$$\text{pH}_{\text{disk}} = -\log \left(\frac{c_{r,H^+} - c_{r,OH^-}}{N_D} - \frac{c_{\infty,H^+} - c_{\infty,OH^-}}{N_D} + c_{\infty,H^+} - c_{\infty,OH^-} \right) \quad (3)$$

For buffered systems, as the phosphate electrolyte used in this work, a correction must be applied to Equation 3, to consider the homogeneous reactions taking place involving the phosphate species. In this case, the OH^- concentration is given by Equation 4 and is applied to Equation 5 to obtain the interfacial disc pH.

$$c'_{OH^-} = c_{OH^-} + [H_2PO_4^-] + 2[HPO_4^{2-}] + 3[PO_4^{3-}] \quad (4)$$

$$N_D = \frac{c'_{r,OH^-} - c'_{\infty}}{c'_{d,OH^-} - c'_{\infty}} \quad (5)$$

The equilibrium constants and further details are available in the Supporting Information, Equations S5-S14. The analytical solution of the quartic equation that results, is shown in Equations S15-S24. The theoretical relationship between pH_{Disc} and pH_{Ring} at various pH_{∞} for a phosphate buffered system is shown in Figure S2c in the SI.

2.3 Results and Discussion

Interfacial pH measurements during hydrogen evolution (HER) using a rotating ring-disc

electrode (RRDE) were performed using the electrode assembly schematically represented in Figure 1a. Prior to measurements, the gold ring and disc electrodes are characterized by blank voltammetry, to assure a clean and reproducible surface (see Figure S3a in the Supporting Information (SI)). For the pH sensing, the gold ring is modified with a self-assembled monolayer of 4-NTP, which is then electrochemically converted to the 4-HATP/4-NSTP redox couple by cyclic voltammetry, as shown in Figure 1b. The 4-NTP modified gold ring is immersed in the electrolyte under potential control (0.3 V vs. Ag/AgCl) and then a cathodic sweep at 100 mVs⁻¹ is performed to partially reduce the monolayer to 4-HATP. The voltammetry of the resulting 4-HATP/4-NSTP redox couple is also shown in Figure 1b recorded at 200 mVs⁻¹ (in red), which is the scan rate used during the pH measurements. In principle, even higher scan rates can be used (up to 500 mVs⁻¹), if the process being studied

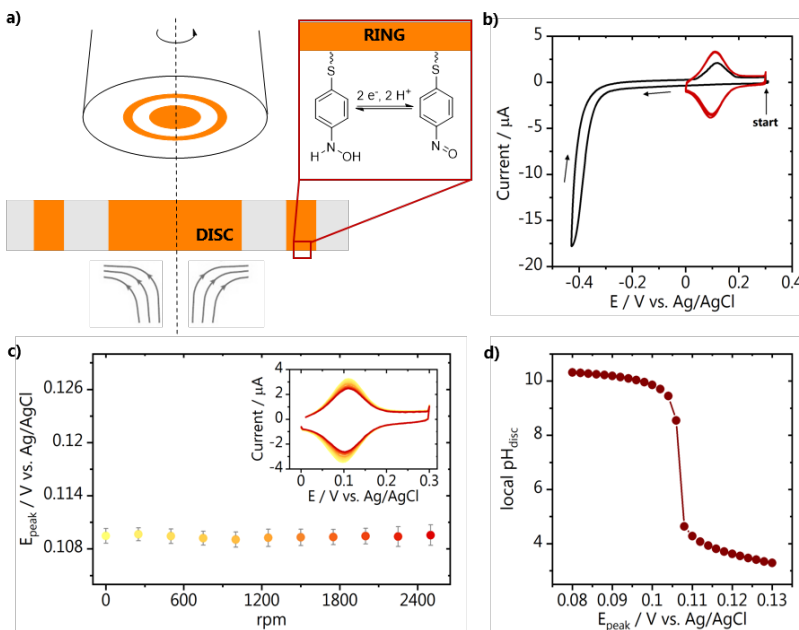


Figure 1. a) Schematic representation of the RRDE with the functionalized ring; b) cyclic voltammetry of the 4-NTP to 4-HATP conversion (black, 100 mV s⁻¹) together with a characterization of the 4-HATP/4-NSTP redox couple (red, 200 mV s⁻¹). Both were recorded in 0.1 M K₂SO₄, pH = 4. c) Effect of rotation on the pH sensor mid-peak potential, extracted from the voltammograms shown in the inset. d) Theoretical relationship between E_{peak} and pH_{disc} using Equation 1 for pH_∞ = 4.

requires better time resolution. Different from our previous work, here the molecule conversion was performed in the same electrolyte as in which HER was carried out. We find

that it gives similar results as in the previously used 0.1 M H_2SO_4 if the 60 mV/pH Nernstian shift of the potential window is taken into account. We show here the voltammetry for the conversion in 0.1 M K_2SO_4 at pH = 4 (Figure 1b). In Figure S3b in the SI, the same is shown in 0.1 KH_2PO_4 and 0.1 M H_2SO_4 , for comparison. The molecule conversion has also been successfully performed in, for example, perchlorate and bicarbonate electrolytes, although not shown here.

Before performing the interfacial pH measurements, we have investigated if the rotation of the electrode has any influence on the 4-HATP/4-NSTP response. The ring voltammetry (CV)

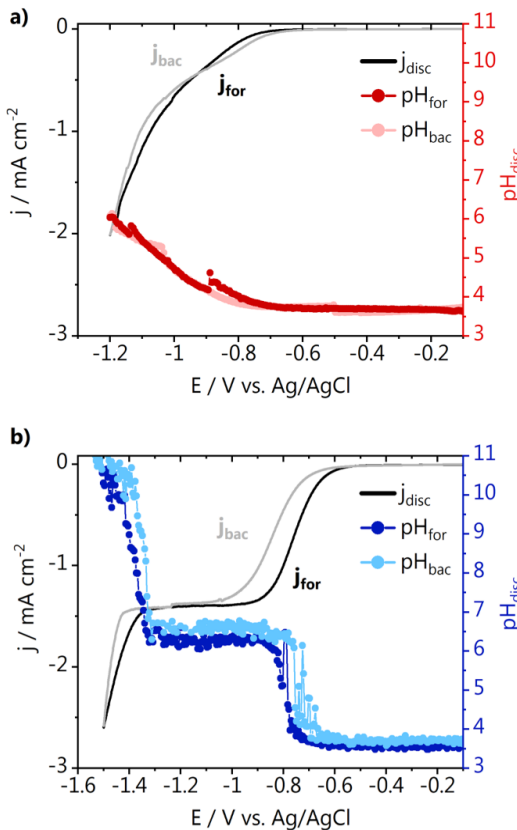


Figure 2. Interfacial pH measurement during the disc cyclic voltammetry in 0.1 M argon saturated at 2000 rpm in a) KH_2PO_4 $\text{pH}_{\text{bulk}} = 3.7$ and b) K_2SO_4 $\text{pH}_{\text{bulk}} = 3.5$. CVs were recorded at 2 mV s^{-1} and the 4-HATP/4-NSTP CVs at 200 mV s^{-1} . The forward and backward scans are indicated as j_{for} , pH_{for} and j_{bac} , pH_{bac} .

was constantly recorded while the rotation rate was varied. Results are shown in Figure 1c going from 0 to 2600 rpm. Each data point is the average mid-peak potential (E_{peak}) determined from 10 consecutive cycles together with the standard deviation, and the corresponding CVs are shown in the graph inset. We observe a stable E_{peak} of 0.109 V vs. Ag/AgCl for all rotation rates. There is a slight decrease in the absolute ring current, however this does not affect the peak fitting and extraction of E_{peak} . These results assure that any changes in the ring voltammetry during HER are due to the reaction taking place at the disc, and not affected by the rotation rate or the turbulence of the electrolyte. This is very important, especially when working far from neutral pH. As shown in Figure 1d, considering an unbuffered electrolyte with a bulk pH of 4, a difference of 20 mV in E_{peak} corresponds to a change in pH_{disc} of 7 pH units. The entire E_{peak} range plotted is actually only 50 mV, which

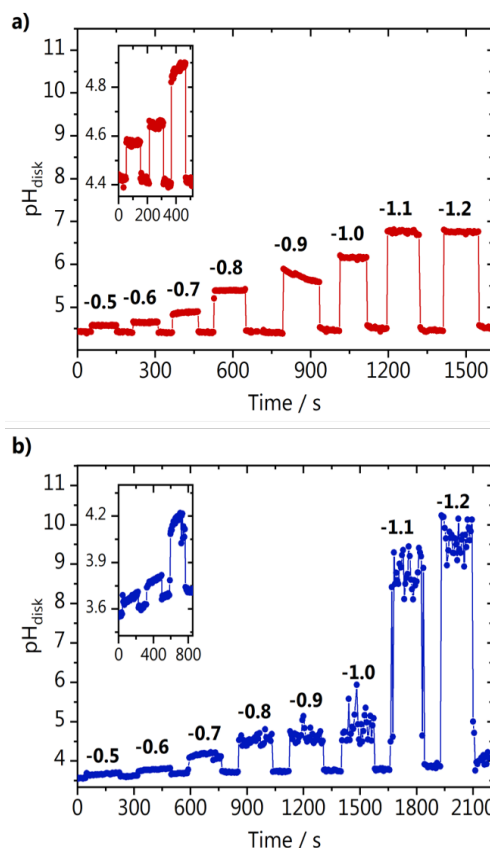


Figure 3. Interfacial pH measurement during chronoamperometry (potentials indicated in the graph in V vs. Ag/AgCl) in 0.1 M argon saturated a) KH_2PO_4 $\text{pH}_{\text{bulk}} = 4.4$ and b) K_2SO_4 $\text{pH}_{\text{bulk}} = 3.6$ at 1600 rpm.

corresponds to the detection of a change of less than a unit in the local ring pH. This also indicates how important it is that the pH sensor employed for RRDE measurements is sensitive and stable enough, to measure the local pH accurately.

We employed the modified ring electrode to measure the development of the interfacial pH during a cyclic voltammogram on the gold disc. Hydrogen evolution was carried out in phosphate and sulfate electrolyte and the correlation between the current density and the measured surface disc pH can be seen in Figure 2 a and Figure 2b, respectively. It is important to point out that the conversion from the measured ring pH to the disc pH is done differently for the experiment in unbuffered sulphate electrolyte in comparison to the phosphate buffer. For sulphate, the analytical description of Yokoyama et al.^[22] is used. In the case of phosphate, we add a correction to account for the homogeneous reactions involving the different phosphate species (H_2PO_4^- , HPO_4^{2-} , PO_4^{3-}) that take place upon increase in the local alkalinity (see the section “Calculating the local disc pH” in the Experimental Section). In Figure 2, we observe that the pH profiles are nearly a mirror image of the current density in both phosphate and sulphate electrolytes. In Figure 2a, we see a gradual increase in current and local pH from 0 to -0.9 V vs. Ag/AgCl. At more negative potentials there is steeper increase in current, likely due to the transition from proton reduction to water and biphenyl reduction as the main branch of HER taking place.^[34] Despite the high current, the interfacial disc pH does not go above 6, due to the buffer capacity of the phosphate electrolyte used. In sulphate electrolyte (Figure 2b) a more well-defined plateau is present due to diffusion limited proton reduction ($2\text{H}^+ + 2\text{e}^- \rightarrow \text{H}_2$) followed by a steep increase in current due to water reduction ($2\text{H}_2\text{O} + 2\text{e}^- \rightarrow \text{H}_2 + 2\text{OH}^-$). The activity for proton reduction starts to increase at about -0.55 V vs. Ag/AgCl and a consequent increase in the interfacial disc pH starts to be observed from -0.57 V vs. Ag/AgCl onwards. This slight delay of 20 mV in the pH response in comparison to the current response is likely because at the very low overpotentials the reaction is only limited by the rate of charge transfer at the electrode-solution interface and there are no pronounced changes in the local proton concentration. At potentials more negative than -0.57 V vs. Ag/AgCl a combination of charge and mass transfer processes control the reaction, and the interfacial pH starts increasing. In the potential window in which the diffusion limited proton reduction plateau is observed, the local disc pH remains around 6.5, until the activity for water reduction increases and consequently the interfacial pH gradually becomes more alkaline. The differences in activity between phosphate and sulphate electrolyte are likely due to the fact that it has been shown that phosphate can outcompete water as a proton donor for hydrogen evolution.^[34] We see that due to the high time resolution achieved with

the 4-HATP/4-NSTP sensor in combination with the low scan rate of the CV (2 mV s⁻¹), detailed information regarding the correlation between current and pH can be obtained. In principle, the disc voltammetry can also be recorded at higher scan rates, at the expense of the resolution of the pH measurement.

Next, we have performed interfacial pH measurements while applying different potentials to the disc electrode. In between potential steps, HER was turned “off” by applying 0 V vs. Ag/AgCl to the disc and the ring voltammetry was constantly recorded. The current and potential recorded in time can be seen in Figure S4 in the SI. Results are shown in Figure 3 for HER carried out in phosphate and sulphate electrolyte. The increase in interfacial disc pH as a function of potential here is slightly larger than what was observed for the cyclic voltammetry from Figure 2. This is due to the lower rotation rate (1600 rpm) employed during the chronoamperometry, slowing down the transport of species away from the electrode surface. At the low overpotentials, we can accurately detect differences in local pH as small as 0.1 pH unit, which has not been previously reported for RRDE pH measurements. This is due to the better sensitivity of the 4-HATP/4-NSTP redox couple used in this work compared to the commonly used pH sensors. The insets in Figure 3a and Figure 3b show the pH measured at -0.5, -0.6 and -0.7 V vs. Ag/AgCl, and highlight how the interfacial pH in the phosphate electrolyte always returns to the bulk pH value once the reaction is turned “off”. The same does not happen in sulphate, where the baseline keeps increasing due to the lower buffer capacity of the electrolyte. The phosphate electrolyte has different strong buffering regions, namely at pH values around the pK_a of the following reversible reactions: $H_3PO_4 \leftrightarrow H_2PO_4^-$ (pK_a = 2.3), $H_2PO_4^- \leftrightarrow HPO_4^{2-}$ (pK_a = 7.2) and $H_2PO_4^- \leftrightarrow PO_4^{3-}$ (pK_a = 12.1). In contrast, in the sulfate electrolyte, only one equilibrium reaction is present ($HSO_4^- \leftrightarrow SO_4^{2-}$) with pK_a = 1.8, considerably lower than the pH developed during HER. It is important to point out that fluctuations of the pH response as observed, for example, at large overpotentials in Figure 3b, occur due to bubbles accumulating near the ring electrode. Even though in this work this did not compromise the measurements, for more challenging systems (or working conditions) this can be circumvented by coating the spacer that separates the ring and the disc electrodes with dopamine.^[35]

The buffer capacity of the electrolyte, the current density, and especially the rotation rate, determine the magnitude of the pH gradients developed during RRDE experiments. Therefore, we have also probed to which extent enhancing mass transport affects the interfacial disc pH by performing chronopotentiometry measurements in the same phosphate and sulphate electrolytes. The reaction was turned “on” and “off” by applying a constant current density of -0.4 mA cm⁻² or -0.001 mA cm⁻² to the disc, at different rotation rates (see Figure S5 in the SI for the current and potential recorded). Figure 4 a shows the

interfacial disc pH during HER in phosphate electrolyte at different rotation rates. Although the changes in pH are not drastic, we see that between 500 and 1000 rpm, the convective flow of species is not high enough to avoid a larger increase in the local alkalinity, despite the buffer capacity of the electrolyte. Still, the interfacial pH when HER is “on” decreases by increasing the rotation rate. At rotations higher than 1250 rpm, a steady state is reached, i.e. the highest flux of species outwards is achieved and increasing rotation no longer decreases the local alkalinity. This happens because a maximum efficiency at which species move from the disc to the ring is reached, as also discussed in the work of Zimer et al.^[11] Due to the buffering species in the phosphate electrolyte, which have easier access to the

surface at the higher rotations, the interfacial disc pH in phosphate equilibrates at values

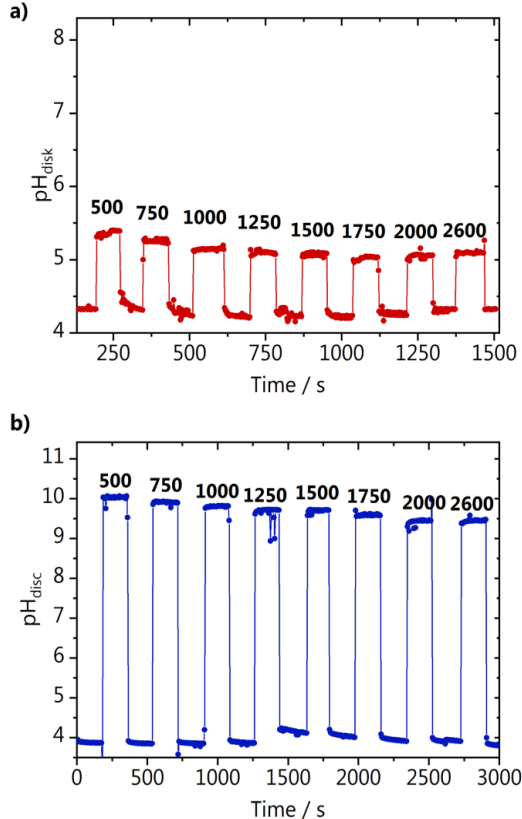


Figure 4. Interfacial pH measurements during chronopotentiometry (constant current density = -0.42 mA cm^{-2}) in 0.1 M argon saturated a) KH_2PO_4 $\text{pH}_{\text{bulk}} = 4.4$ and b) K_2SO_4 $\text{pH}_{\text{bulk}} = 4.0$ at the different rotations indicated in the graph in rpm.

around 5.2 at steady state. A different behaviour is observed in the sulphate electrolyte (Figure 4b). Here, although increasing rotation also gradually decreases the local disc pH, a stable pH is never reached at high rotation rates, due to the low buffer capacity of the electrolyte. Additionally, the interfacial disc pH never returns to the bulk value when the reaction is turned “off” (in between different rotations), similarly to what we observed in the chronoamperometry experiment in sulphate (inset of Figure 3b). It is important to point out that even though the calculated interfacial disc pH changes are relatively large, the differences in E_{peak} recorded at the ring electrode are rather small. Figure S6 in the SI exemplifies that with the E_{peak} recorded for the experiments shown in Figure 4. The changes in E_{peak} observed during the whole experiment are in the 15-40 mV range, highlighting once more how important it is to employ a sensitive pH sensor for RRDE pH measurements.

The results shown demonstrate that, even though RRDE systems are used to avoid (or minimize) concentration gradients during electrochemical reactions, the effectiveness of the enhancement in mass transport is highly dependent on the electrolyte buffer capacity and on the currents drawn. Assuming “well-defined mass transport conditions” when working with RRDE does therefore not imply absence of concentration gradients, as we see that (in our working conditions) the local disc pH can vary up to 6-7 pH units from the bulk pH. This has important consequences, for example, for measurements performed as a function of rotation rate going from low to high rotations. The local pH values will be significantly different, and their effect is difficult to deconvolute, unless proper quantification of the pH is carried out. In the electrolytes studied, even with a relatively high buffer capacity (phosphate electrolyte) and rotation rates (> 1250 rpm), the interfacial disc pH differed by 1 unit from the bulk. Operating in the steady state regime (strong buffer, high rotations) minimizes convoluted responses due to differences in the interfacial disc pH. However, as evidenced by our results, this regime is strongly dependent on the electrolyte and reaction activity, and has to be identified for each individual system studied. Using the 4-HATP/4-NSTP redox couple as pH sensor on the ring electrode, allows to do so with high temporal resolution and sensitivity. The synthesis of the functionalized gold ring shown in this work is much simpler than what was previously reported for IrOx^[11], highly reproducible, and the system is versatile in terms of disc materials that can be employed, and reactions to be studied.^[33] Finally, even though the analytical description from Albery and Calvo^[19-21] and Yokoyama et al.^[22] is accurate for calculating pH_{disc} for measurements performed in unbuffered electrolytes, here we present a method to correct the description when working in buffered solutions. This is crucial to avoid an overestimation of the interfacial disc pH in buffered systems.

2.4 Conclusion

In this work we have shown that RRDE interfacial pH measurements can be performed with high sensitivity and temporal resolution using a voltammetric pH sensor. A gold ring functionalized with the 4-HATP/4-NSTP redox couple has been used to study pH gradients developing during hydrogen evolution at a gold disc electrode. The interfacial disc pH is measured in phosphate or sulphate electrolyte during different electrochemical experiments: cyclic voltammetry, chronoamperometry and chronopotentiometry. We observed that the changes in interfacial pH at the disc strongly depend on the buffer capacity of the electrolyte and the current drawn (i.e. the activity). By varying the rotation rate at constant current density, we identify the minimum rotation required to achieve the maximum enhancement of mass transport possible and avoid strong concentration gradients during the electrocatalytic measurements. Using HER as a model system, we show that the 4-HATP/4-NSTP voltammetric pH sensor is a powerful tool for accurately measuring interfacial pH with RRDE, with high time resolution.

References

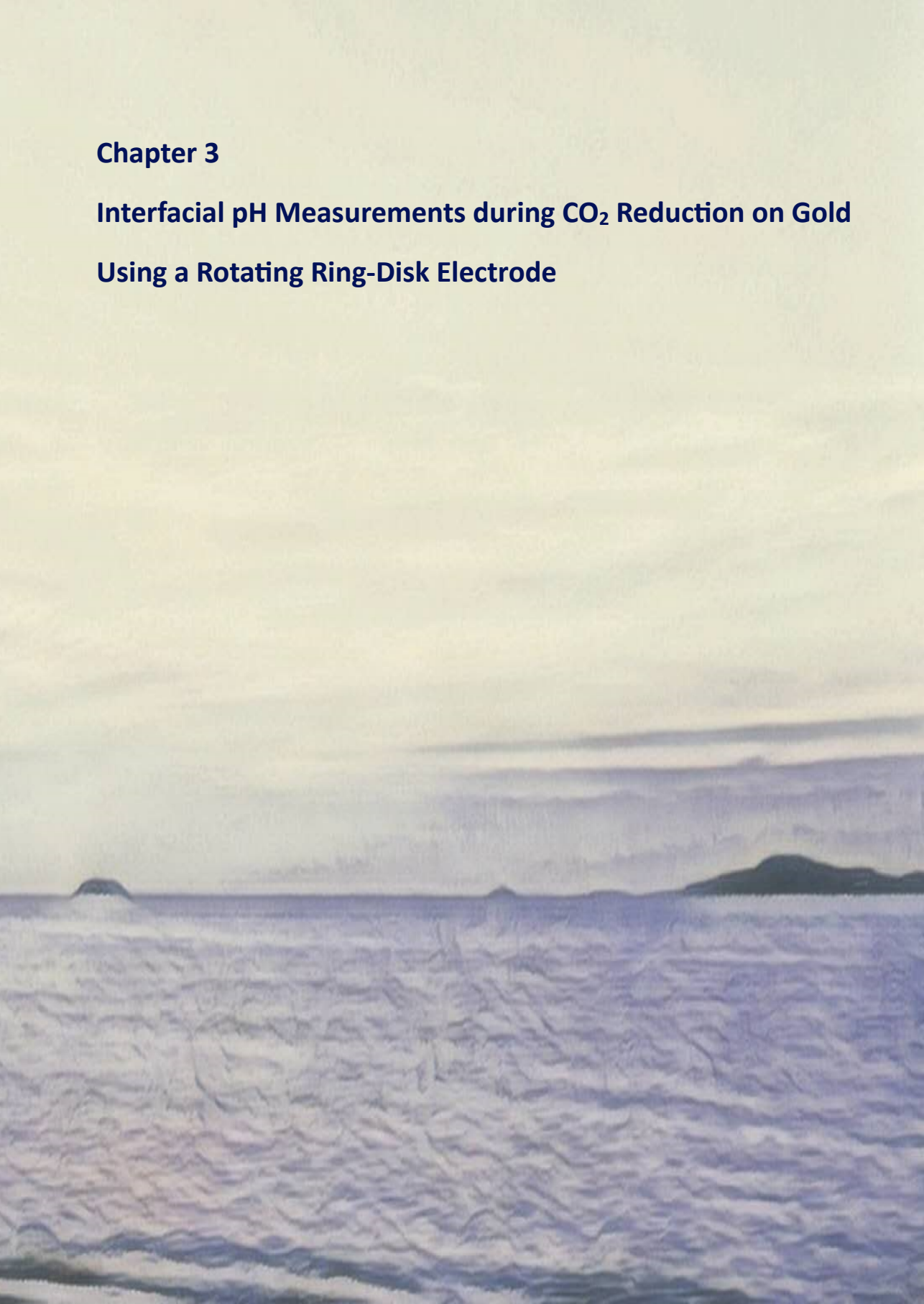
- [1] M. C. O. Monteiro, M. T. M. Koper, *Curr. Opin. Electrochem.* **2021**, *25*, 100649.
- [2] A. Goyal, M. T. M. Koper, *Angew. Chemie Int. Ed.* **2021**, *60*, 13452–13462.
- [3] Z. Zhang, L. Melo, R. P. Jansonius, F. Habibzadeh, E. R. Grant, C. P. Berlinguette, *ACS Energy Lett.* **2020**, *5*, 3101–3107.
- [4] L. Giordano, B. Han, M. Risch, W. T. Hong, R. R. Rao, K. A. Stoerzinger, Y. Shao-Horn, *Catal. Today* **2016**, *262*, 2–10.
- [5] M. F. Li, L. W. Liao, D. F. Yuan, D. Mei, Y.-X. Chen, *Electrochim. Acta* **2013**, *110*, 780–789.
- [6] M. C. O. Monteiro, L. Jacobse, T. Touzalin, M. T. M. Koper, *Anal. Chem.* **2020**, *92*, 2237–2243.
- [7] C. S. Santos, A. S. Lima, D. Battistel, S. Daniele, M. Bertotti, *Electroanalysis* **2016**, *28*, 1441–1447.
- [8] S. Dieckhöfer, D. Öhl, J. R. C. Junqueira, T. Quast, T. Turek, W. Schuhmann, *Chem. – A Eur. J.* **2021**, *27*, 5906–5912.
- [9] B. P. Nadappuram, K. McKelvey, R. Al Botros, A. W. Colburn, P. R. Unwin, *Anal. Chem.* **2013**, *85*, 8070–8074.
- [10] C. A. Morris, C. C. Chen, T. Ito, L. A. Baker, *J. Electrochem. Soc.* **2013**, *160*, H430–H435.
- [11] A. M. Zimer, M. Medina da Silva, E. G. Machado, H. Varela, L. H. Mascaro, E. C. Pereira, *Anal. Chim. Acta* **2015**, *897*, 17–23.
- [12] M. C. Figueiredo, R. M. Arán-Ais, V. Climent, T. Kallio, J. M. Feliu, *ChemElectroChem* **2015**, *2*, 1254–1258.
- [13] F. Zhang, A. C. Co, *Angew. Chemie - Int. Ed.* **2020**, *59*, 1674–1681.

- [14] P. Steegstra, E. Ahlberg, *J. Electroanal. Chem.* **2012**, *685*, 1–7.
- [15] A. J. Leenheer, H. A. Atwater, *J. Electrochem. Soc.* **2012**, *159*, H752–H757.
- [16] K. Yang, R. Kas, W. A. Smith, *J. Am. Chem. Soc.* **2019**, *141*, 15891–15900.
- [17] O. Ayemoba, A. Cuesta, *ACS Appl. Mater. Interfaces* **2017**, *9*, 27377–27382.
- [18] D. A. Henckel, M. J. Counihan, H. E. Holmes, X. Chen, U. O. Nwabara, S. Verma, J. Rodríguez-López, P. J. A. Kenis, A. A. Gewirth, *ACS Catal.* **2021**, *11*, 255–263.
- [19] W. J. Albery, E. J. Calvo, *J. Chem. Soc. Faraday Trans. 1 Phys. Chem. Condens. Phases* **1983**, *79*, 2583–2596.
- [20] W. J. Albery, A. R. Mount, *J. Chem. Soc. Faraday Trans. 1 Phys. Chem. Condens. Phases* **1989**, *85*, 1181.
- [21] W. J. Albery, A. R. Mount, *J. Chem. Soc. Faraday Trans. 1 Phys. Chem. Condens. Phases* **1989**, *85*, 3717.
- [22] Y. Yokoyama, K. Miyazaki, Y. Miyahara, T. Fukutsuka, T. Abe, *ChemElectroChem* **2019**, 4750–4756.
- [23] P. Steegstra, E. Ahlberg, *Electrochim. Acta* **2012**, *76*, 26–33.
- [24] A. J. Bard, M. V. Mirkin, *Scanning Electrochemical Microscopy*, CRC Press, **2012**.
- [25] X. Chen, I. T. McCrum, K. A. Schwarz, M. J. Janik, M. T. M. Koper, *Angew. Chemie - Int. Ed.* **2017**, *56*, 15025–15029.
- [26] G. García, *ChemElectroChem* **2017**, *4*, 459–462.
- [27] S. Xue, B. Garlyyev, S. Watzele, Y. Liang, J. Fichtner, M. D. Pohl, A. S. Bandarenka, *ChemElectroChem* **2018**, *5*, 2326–2329.
- [28] P. Rodriguez, M. T. M. Koper, *Phys. Chem. Chem. Phys.* **2014**, *16*, 13583–13594.
- [29] G. García, M. T. M. Koper, *ChemPhysChem* **2011**, *12*, 2064–2072.
- [30] H. Kita, K. Shimazu, K. Kunimatsu, *J. Electroanal. Chem.* **1988**, *241*, 163–179.
- [31] J. Rossmeisl, K. Chan, E. Skúlason, M. E. Björketun, V. Tripkovic, *Catal. Today* **2016**, *262*, DOI 10.1016/j.cattod.2015.08.016.
- [32] M. C. O. Monteiro, L. Jacobse, T. Touzalin, M. T. M. Koper, *Anal. Chem.* **2020**, *92*, 2237–2243.
- [33] M. C. O. Monteiro, L. Jacobse, M. T. M. Koper, *J. Phys. Chem. Lett.* **2020**, *11*, 9708–9713.
- [34] M. N. Jackson, Y. Surendranath, *J. Am. Chem. Soc.* **2016**, *138*, 3228–3234.
- [35] J. G. Vos, M. T. M. Koper, *J. Electroanal. Chem.* **2019**, *850*, 113363.
- [36] M. C. O. Monteiro, M. T. M. Koper, *Electrochim. Acta* **2019**, *325*, 134915.
- [37] U. P. Do, F. Seland, E. A. Johannessen, *J. Electrochem. Soc.* **2018**, *165*, 219–228.



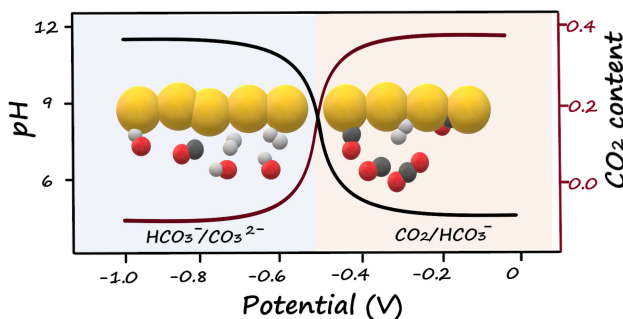
Chapter 3

Interfacial pH Measurements during CO₂ Reduction on Gold Using a Rotating Ring-Disk Electrode



Abstract

Insights into how to control the activity and selectivity of the electrochemical CO₂ reduction reaction are still limited because of insufficient knowledge of the reaction mechanism and kinetics, which is partially due to the lack of information on the interfacial pH, an important parameter for proton-coupled reactions like CO₂ reduction. Here, we used a reliable and sensitive pH sensor combined with the Rotating Ring-Disk Electrode technique, in which a functionalized Au ring electrode works as a real-time detector of the OH⁻ generated during the CO₂ reduction reaction at a gold disk electrode. Variations of the interfacial pH due to both electrochemical and homogeneous reactions are mapped and the correlation of the interfacial pH with these reactions is inferred. The interfacial pH near the disk electrode increases from 7 to 12 with increasing current density, with a sharp increase at around -0.5 V vs RHE, which indicates a change of the dominant buffering species. Through scan rate-dependent voltammetry and chronopotentiometry experiments, the homogenous reactions are shown to reach equilibrium within the time scale of the pH measurements, so that the interfacial concentrations of different carbonaceous species can be calculated using equilibrium constants. Furthermore, pH measurements were also performed under different conditions to disentangle the relationship between the interfacial pH and other electrolyte effects. The buffer effect of alkali metal cations is confirmed, showing that weakly hydrated cations lead to less pronounced pH gradients. Finally, we probe to which extent increasing mass transport and the electrolyte buffer capacity can aid in suppressing the increase of the interfacial pH, showing that the buffer capacity is the dominant factor in suppressing interfacial pH variations.

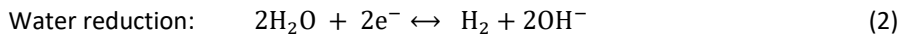
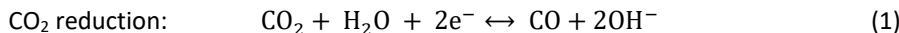


This chapter is based on Liu, X.; Monteiro, M. C. O.; Koper, M. T. M., Interfacial pH measurements during CO₂ reduction on gold using a rotating ring-disk electrode. *Phys. Chem. Chem. Phys.* 2023, 25 (4), 2897-2906.

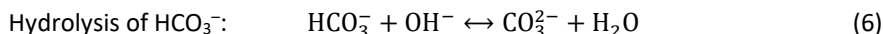
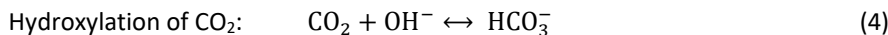
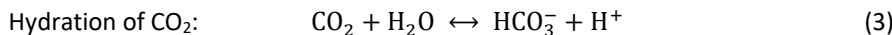
3.1 Introduction

The electrochemical conversion of CO₂ into high value-added feedstocks is believed to be a promising method to deploy renewable electricity and convert CO₂ into useful products. To enhance the reaction activity and selectivity of the electrochemical CO₂ reduction reaction (CO₂RR) and to suppress the major competing hydrogen evolution reaction (HER), numerous efforts to catalyst improvement have been made over the past decade.^{1, 2} The electrolyte composition is also an important factor to be reckoned with.³⁻⁵ CO₂RR is generally carried out in an alkali bicarbonate electrolyte. Alkali cations,⁶⁻⁸ bicarbonate,⁹⁻¹¹ and the pH of the electrolyte¹²⁻¹⁴ are recognized to influence both CO₂RR and HER significantly, and all these variables have been reported to influence the interfacial pH. Therefore, specific information about the near-surface pH is highly desired to better understand the CO₂RR.

Due to the production of OH⁻ at the interface in neutral and alkaline media (eqs 1-2),



the thermodynamics and kinetics of both CO₂RR and HER change with pH.^{15, 16} Moreover, there is also a sequence of pH-dependent homogenous reactions taking place, as displayed in Eqs 3-6:^{17, 18}



These homogeneous reactions primarily function as buffer reactions, as CO₂ and HCO₃⁻ can partially consume OH⁻ generated from CO₂RR and HER. Still, because of mass transport limitations, OH⁻ accumulates near the electrode interface, leading to a higher interfacial pH than the bulk value.¹⁹⁻²¹ As a result, the interfacial pH determines the interfacial CO₂ concentration, which is directly connected with the CO₂RR rate. Moreover, the local high OH⁻ concentration affects the local cation concentration, by electroneutrality.^{15, 22} This local cation concentration has a strong influence on both the CO₂RR and HER rates: alkali cations have been proposed to stabilize certain intermediates of CO₂RR⁸ and HER,^{15, 26} buffer the interfacial pH^{7, 23} and modify the local electric field.^{24, 25} The activity for CO₂RR and HER has been reported to increase in the order Li⁺ < Na⁺ < K⁺ < Cs⁺, which has been attributed to a larger accumulation of Cs⁺ at the reaction interface^{7, 23}. Finally, the interfacial pH determines the local HCO₃⁻ concentration, and this species contributes to the total hydrogen production through reaction 7:²⁷



However, since it is difficult to determine the interfacial pH accurately, comprehensive understanding and deconvolution of pH effects from other electrolyte effects are still lacking. On account of the decisive role of the interfacial pH, various techniques have been used throughout the years to measure this key variable,²⁸ with Scanning Probe Microscopy (SPM) and *in situ* spectroscopy being the most common ones. Due to the high spatial resolution that can be obtained, SPM techniques are very good candidates for measuring the local pH.²⁹⁻³³ Still, depending on, for example, the feedback used for approaching the surface, pH sensing components may suffer from instability issues.^{34, 35} Besides, the probe can significantly hinder mass transport, leading to an overestimation of the local pH.²⁰ Surface-enhanced spectroscopies such as attenuated total reflectance surface-enhanced infrared absorption spectroscopy (ATR-SEIRAS) and surface-enhanced Raman spectroscopy (SERS) are also powerful tools for measuring the local pH, in addition to their ability to detect reaction intermediates.^{21, 36, 37} Here, the local pH is normally determined by the ratio of the integrated peak areas between buffer species, i.e. CO₂ and HCO₃⁻. It would be a reliable pH indicator only if the equilibrium between CO₂ and HCO₃⁻ was indeed established. However, this is the slowest buffering reaction taking place at the interface, as we will discuss further below. Other pH-sensitive molecules can also be introduced as pH probes, though with a risk of perturbing the reactions under consideration.³⁸

Developed by Frumkin years ago, the Rotating Ring-Disk Electrode (RRDE) has long been applied as a powerful electroanalytical tool³⁹ and an ideal real-time detector of products.⁴⁰⁻⁴² Moreover, due to the convective flow of species induced by the electrode rotation, high rates of mass transport can be well-controlled, facilitating deconvolution of mass transport effects from other electrolyte effects. Albery and Calvo⁴³ performed pioneering pH measurements using RRDE and developed the corresponding theory as early as 1982. Since then, RRDE pH measurements have been applied to different electrochemical systems.⁴⁴⁻⁴⁶ Still, the accuracy and sensitivity of the RRDE pH sensor is highly dependent on the pH-sensitive material. Zhang et al.⁴⁷ reported pH measurements based on RRDE using the peak potential of CO oxidation on a Pt ring as pH indicator during CO₂RR on the disk. However, there are multiple factors affecting the oxidation of CO on Pt, making it complicated to interpret shifts of the peak potential solely in terms of pH effects.^{31, 48} More recently, Tackett et al.⁴⁵ reported a simulation model incorporating electrochemical and buffering reactions to quantify the relationship between the interfacial pH near the ring and the disk electrode of RRDE during CO₂RR. However, each pH data point was measured by recording the open circuit potential (OCP) of an IrO_x-modified ring for 120s, so that the sensitivity and time

resolution of their pH sensor was limited. Besides, the response of the IrO_x pH sensor is largely dependent on the thickness and oxidation state of the IrO_x film⁴⁹ and the working conditions, e.g., current density.⁴⁴ As a result, only a few pH data points were obtained under steady-state chronopotentiometry conditions on the disk.

To overcome limitations in previous pH measurements, we have developed a highly sensitive voltammetric pH sensor, based on the 4-hydroxylaminothiophenol/4-nitrosothiophenol (4-HATP and 4-NSTP) redox couple, whose peak potential shows a Nernstian shift with pH over a broad pH range.^{20,31,32} The time scale of the pH sensor depends on the scan rate with which the redox couple is measured. In this work, the redox couple was cycled within a 400 mV potential window at 200 mV s⁻¹, so that the pH is measured every 4 s. Recently, we have combined this redox couple to a RRDE system by modifying a gold ring with the pH probe. Feasibility and versatility of the 4-HATP/4-NSTP modified RRDE pH probe in different electrolytes were validated by measuring the interfacial pH during HER on a gold disk.⁴² Here, we apply the RRDE pH probe to estimate the interfacial pH during CO₂RR on a gold electrode. Coupled with the highly sensitive and stable voltammetric pH sensor (4-HATP/4-NSTP), with RRDE we can record the variation of interfacial pH in a broad potential range with high accuracy. We have compiled the advantages of our pH sensor compared to previous literature in the Supporting Information (Table S1). Because of the good time resolution of our sensor, we can test the level of equilibration of the homogeneous buffer reactions during cyclic voltammetry. This unique method provides a definite correlation of interfacial pH with mass transport, and other electrolyte effects such as ionic strength and cation identity. Our measurements in different electrolytes prove the buffering effect of cations, and show how the role of mass transport and buffer capacity on CO₂RR is closely related to interfacial pH changes. We will argue that the insights obtained here are relevant to other electrode materials and geometries as well.

3.2 Experimental section

Chemicals and Materials. Electrolytes were prepared using ultrapure water (>18.2 MΩ cm, Millipore Milli-Q) and the following chemicals: Li₂CO₃ (>99.999%, trace metal basis, Thermo Fisher), NaHCO₃ (>99.7%, metal basis, anhydrous, Alfa Aesar), KHCO₃ (>99.9%, metal basis, Alfa Aesar), Rb₂CO₃ (>99.8%, metal basis, Merck), NaClO₄(H₂O)_x (>99.99%, trace metal basis, Sigma-Aldrich), H₂SO₄ (96%, Merck, Suprapur). All carbonate and bicarbonate electrolytes were pre-purified in Chelex (particle size: 50-100, Merck) overnight to eliminate possible metal impurities⁵⁵ and purged with either Ar (6.0 purity, Linde, 20 min) or CO₂ (4.5 purity, Linde, 20 min for bicarbonates and 1h for carbonates) before experiments. All the

electrochemical experiments were conducted with a 4-channel Biologic potentiostat (VSP-300) and Modulated Speed Rotator (Pine Research) in a home-made single compartment electrochemical cell. The electrochemical cell and other glassware were kept in KMnO_4 solution (1 g L^{-1} KMnO_4 in 0.5 M H_2SO_4) overnight and then immersed in dilute piranha solution to remove the generated MnO_x and the residual KMnO_4 . Before using, they were rinsed and boiled with ultrapure water five times. A ring-disk electrode (Au ring and Au disk, E6/E5 ChangeDisk, Pine Research), a Au wire (0.5 mm diameter, MaTeck, 99.9%) and a Ag/AgCl electrode (RE-1B, 3 M NaCl, Biologic, inserted in a Luggin capillary) were used as working electrode, counter electrode and reference electrode, respectively. Before being put in contact with the electrolyte, the Au counter electrode was flame annealed using a butane torch.

Preparation and modification of the electrodes. After inserting the Au disk (5.0 mm diameter) in the Au ring matrix, the RRDE tip was polished with 3 μm , 1 μm , 0.25 μm diamond suspension (MetaDi, Buehler), respectively, and sonicated in ethanol and ultrapure water for 5 min in between polishing steps. Before measurements, both ring and disk electrodes were characterized in Ar-saturated 0.1 M H_2SO_4 by cyclic voltammetry at 100 mV s^{-1} between 0 and 1.75 V vs RHE (see Figure S1a in the Supporting Information). The electrochemical surface area (ECSA) of the disk electrode was calculated by the ratio of the charge of the Au oxide reduction peak and the charge density of a Au oxide monolayer (386 $\mu\text{C cm}^{-2}$). Then, the Au disk was changed into a Teflon counterpart and the RRDE tip was dipped into a 1 mM 4-NTP (4-nitrothiophenol (4-NTP, Merck, 80%) dissolved in ethanol (96%, absolute, VWR) solution for 20 min, during which the thiol-containing compound would self-assemble as a monolayer on the Au ring electrode. After that, the tip is rinsed with ethanol and water respectively, and dried in a N_2 flow. The Au disk was reassembled carefully and the 4-NTP on the ring was further converted to the pH sensing redox couple 4-NSTP/4-HATP via cyclic voltammetry in 0.1 M H_2SO_4 from 0.68 to 0.11 V vs RHE at 100 mV s^{-1} . The lower vertex potential of 0.11 V vs RHE is set so that the conversion efficiency is maximized (see Figure S1b-d).

RRDE pH measurements. The Au disk was cycled from 0 to -1.0 V vs RHE in different electrolytes with a 2 mV s^{-1} scan rate while the cyclic voltammograms of the 4-HATP/4-NSTP pH sensing couple were continuously recorded with a scan rate of 200 mV s^{-1} . The potential window was adjusted when necessary, as the interfacial pH increased. Specifically, the cycling range on the ring in CO_2 -saturated bicarbonate (pH 6.8) was kept to be -0.25 V to 0.15 V vs Ag/AgCl until the potential on the disk reached -0.5 V vs RHE. It was then changed to -0.35 V to 0.05 V vs Ag/AgCl when the interfacial pH was around 9. To avoid any

interference from oxygen, the gases (CO₂ or Ar) were continuously purged into the electrolyte during the measurements. Details of the calculations of the interfacial pH are given in the Supporting Information.

3.3 Results and discussion

Interfacial pH measurement with RRDE. The details of using RRDE with the voltammetric pH sensor on the ring are given in our previous paper⁴² and in the Supporting Information. Briefly, the interfacial pH measured at the ring can be converted to the corresponding interfacial pH at the disk using the equations developed by Albery and Calvo, also taking into account the buffering reactions taking place in the electrolyte. The relevant mathematical equations are given in the Supporting Information, as well as a discussion of the expected accuracy of the calculated disk pH. We also note that our aim with this method is not to claim absolute accuracy of individual pH values (also because in reality the pH near the disk is not a constant as there is not a perfectly homogeneous current distribution), but rather to evaluate semi-quantitative changes in the interfacial pH values during cyclic voltammetry in different electrolytes with different parameters, such as buffering strength, cation identity, and rate of mass transport. As mentioned in the Introduction, the very distinct advantage of using RRDE for performing such measurements is that in this setup, the pH measurement does not disturb the interfacial environment as the pH probe is remote from the interface itself (a typical diffusion layer thickness under our conditions is 12.24 μm (detailed calculation in the supporting information), while the ring electrode is 1.5 mm away from the disk electrode.). Therefore, we expect the results to be identical to configurations where the pH probe is absent.

Variation of the interfacial pH during CO₂RR. The interfacial pH of the Au disk is measured while cycling the electrode slowly at 2 mV s⁻¹ from 0 to -1.0 V vs RHE. The increase in current density with potential leads to an increasing generation of OH⁻ near the surface of the electrode (Figure 1a). As a result, the interfacial pH rises considerably with current density (Figure 1b), despite the high electrode rotation rate (2500 rpm) and the buffering from both CO₂ and HCO₃⁻. According to the pH recorded, the potential and current density range from Figure 1 can be divided into two regions, each dominated by a different buffer. At less negative potentials and lower current densities (red shaded region in Figure 1), only a small change in pH is detected and the interfacial pH stabilizes around 7 (bulk pH 6.8). With the rise in current density at around -0.5 V, the pH increases drastically from 7 to 9, suggesting a change in interfacial environment. At even more negative potentials and current densities (blue shaded region in Figure 1), the pace of the pH variation slows down again despite the

high and increasing current. This is in agreement with the results from Tackett et al.⁴⁵, though our measurements have a higher resolution owing to the advantages mentioned above.

There are two buffers in CO_2 -saturated bicarbonate electrolyte: according to the Henderson-Hasselbalch equation ($\text{pH} = \text{pK}_a + \log([\text{A}^-]/[\text{HA}])$, where HA is the acid and A^- is its conjugated base),⁵⁰ the buffer range of $\text{CO}_2/\text{HCO}_3^-$ is 5.35-7.35 ($\text{pK}_{\text{CO}_2/\text{HCO}_3^-} = 6.35$), while it is 9.33 - 11.33 for $\text{HCO}_3^-/\text{CO}_3^{2-}$ ($\text{pK}_{\text{HCO}_3^-/\text{CO}_3^{2-}} = 10.33$). Once the interfacial pH during CO_2RR exceeds the buffer range, $[\text{HA}]$ is too low and the buffer breaks down. Therefore, the increase of interfacial pH from 7 to 9 marks the breakdown of the $\text{CO}_2/\text{HCO}_3^-$ buffer and the onset of the $\text{HCO}_3^-/\text{CO}_3^{2-}$ buffer. Since the interfacial pH influences the corresponding reactions and their kinetics (see Introduction), this substantial pH change is expected to be a turning point for both the homogenous reactions and the electrochemical reactions.

Equilibrium of the homogenous reactions. As mentioned above, the $\text{CO}_2/\text{HCO}_3^-$ couple buffers through either the hydration or hydroxylation pathways (Eqs. 3-4), while $\text{HCO}_3^-/\text{CO}_3^{2-}$ buffers through either the protolysis or the hydrolysis pathways (Eqs. 5-6).^{17, 18} By comparing the reaction rates given by Eqs. 8-11,

$$r_{3+} = k_{3+}[\text{CO}_2] \quad (8)$$

$$r_{4+} = k_{4+}[\text{CO}_2][\text{OH}^-] \quad (9)$$

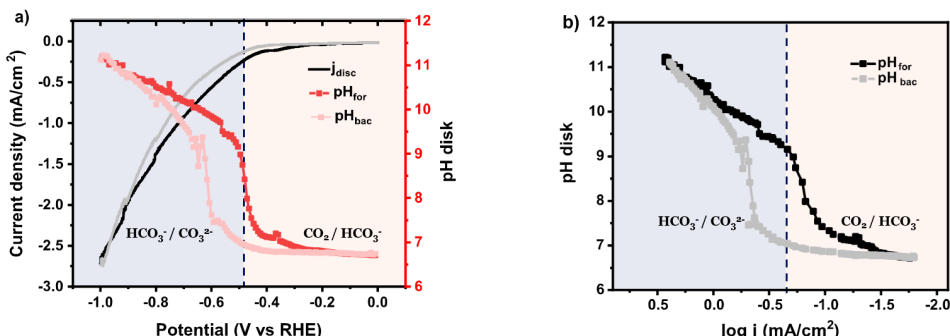


Figure 1. a) Variation of the interfacial pH recorded during cyclic voltammetry in CO_2 -saturated 0.1 M NaHCO_3 at 2 mV s⁻¹ and a rotation rate of 2500 rpm: the solid line is the current density with the forward and backward scans in black and grey, respectively, while the red and pink curves refer to the corresponding interfacial pH during the forward and backward scan, respectively. b) Interfacial pH as function of the logarithm of the current density during the cyclic voltammetry from a). Potentials in all figures have been converted to the RHE scale using the bulk pH.

$$r_{5+} = k_{5+}[\text{HCO}_3^-] \quad (10)$$

$$r_{6+} = k_{6+}[\text{HCO}_3^-][\text{OH}^-] \quad (11)$$

the hydration reaction (Eq. 3) is the main buffering reaction in the CO₂/HCO₃⁻ working region here (at pH 5-7), while the hydrolysis pathway (Eq. 6) dominates in the HCO₃⁻/CO₃²⁻ buffering region here (at pH 9-11) (k₃₊ to k₆₊ have been reported as 0.037 s⁻¹, 2.23×10³ M⁻¹s⁻¹, 59.4 s⁻¹, 6.0×10⁶ M⁻¹s⁻¹, respectively).¹⁸

Based on these rate constants, the equilibrium between HCO₃⁻ and CO₃²⁻ should be established within microseconds,^{17,20} while it takes on the order of 10 s to reach equilibrium for the CO₂/ HCO₃⁻ buffer at pH 5.35-7.35 due to the slow hydration of CO₂ (these equilibration times are estimated from literature parameters.¹⁷). During the measurements, a slow scan rate of 2 mV s⁻¹ is applied to the disk electrode to minimize the disturbance of the system and the pH is recorded every 4 s, which is compatible with this timescale. This makes it reasonable to assume that all buffering reactions are in equilibrium at this scan rate. To confirm the validity of this equilibrium assumption, variations of interfacial pH were recorded as a function of the scan rate of the disk electrode, in CO₂-saturated bicarbonates. As shown in Figure S4b, the interfacial pH increases with the scan rate. However, since the current density increases with the scan rate as well (Figure S4a), this also contributes to the increase of interfacial pH. To deconvolute the impact from current density and scan rate, similar experiments were performed in CO₂-saturated acidic perchlorates. As shown in Figure 2, the proton reduction reaction reaches its diffusion limited plateau (Figure 2a) from -0.6 V vs RHE. The current densities of these diffusion-controlled plateaus are independent of scan rates, so that interference from current density is avoided. Besides, the corresponding interfacial pH of these plateaus is around 7 (Figure 2b), which is within the buffer range of CO₂/HCO₃⁻, making the plateau a window to study the CO₂ hydration pathway at different time scales (using different scan rates). As the scan rate is increased from 2 mV s⁻¹ to 20 mV s⁻¹, no obvious change in the interfacial pH plateaus is found, in agreement with the corresponding current density plateaus. However, at scan rates higher than 10 mV s⁻¹, the first few data points of interfacial pH, recorded just before reaching the plateau, are slightly higher, which indicates that the homogeneous reactions have not yet reached equilibrium. This agrees well with the relaxation times mentioned above: it takes ~12 seconds (3 data points, corresponding to 24 mV for 2 mV s⁻¹, but to 120 mV for 10 mV s⁻¹) for the interfacial pH to equilibrate to the plateau value (pH = 7). For scan rates lower than 5 mV s⁻¹, this slow equilibration is not observed, demonstrating that the homogeneous reactions can be considered to be in equilibrium in the CO₂/HCO₃⁻ buffering region.

Chronopotentiometry experiments at different current densities were also conducted,

under the same conditions. CO₂RR on the disk is turned “on” and “off” every 2 minutes while the variation of pH is constantly measured at the ring. Since CO₂/HCO₃⁻ buffers until pH 7.35, according to Figure 2c, CO₂/HCO₃⁻ buffers when the current density is smaller than 2.8 mA cm⁻² (pink region), while HCO₃⁻/CO₃²⁻ buffering becomes dominating thereafter. At current densities between 0.3-2.3 mA cm⁻² an initial increase of the interfacial pH is observed, followed by a decrease reaching a plateau. This is highlighted in the insets of Figure 2c. This illustrates that CO₂/HCO₃⁻ takes a few seconds to equilibrate and, remarkably, this process is recorded by the pH sensor. In fact, this transient increase in local pH has also been detected using SECM in our previous work.²⁰ By contrast, for HCO₃⁻/CO₃²⁻ buffering region (current density equal or higher than 2.8 mA cm⁻²), such transient increase is not expected, as the HCO₃⁻/CO₃²⁻ equilibrium is reached within microseconds. However, we could not observe that in the data here due to the disturbance caused by H₂ bubbles at these currents.

Speciation of the electrolyte at the CO₂RR interface. As CO₂ is continuously purged into the electrolyte during the measurements, the total carbon concentration (TC, Eq. S7 in the Supporting Information), which is the sum of the concentrations of the intrinsic (bi-)carbonate electrolyte and the saturated CO₂ concentration from extrinsic bubbling, stays constant.⁵¹ However, the distribution of the various carbonaceous species (i.e. CO₂, HCO₃⁻, and CO₃²⁻) near the surface alters as a function of the interfacial pH, which is in turn a consequence of the CO₂RR and the concurrent homogeneous reactions. As the homogeneous reactions can be considered to be in equilibrium, the interfacial concentrations of the carbonaceous species can be obtained by working out the equilibrium equations (Eqs. S8-S10 in the Supporting Information), so that variation of these concentrations during CO₂RR can be traced in real time (Figure 3). In the CO₂/HCO₃⁻ buffering region, the concentration of CO₂ decreases sharply as it is consumed both as an electrochemical reactant and as a buffer reagent. The concentration of HCO₃⁻ increases, while there is only a trace amount of CO₃²⁻. As the interfacial pH rises, the interfacial CO₂ becomes exhausted, the concentration of HCO₃⁻ near the electrode starts to decay, while the concentration of CO₃²⁻ increases, as illustrated in Figure 3. Noteworthily, the depletion of interfacial CO₂ by the end of the CO₂/HCO₃⁻ buffering region does not mean that the CO₂RR is diffusion limited. Instead, as a bifunctional species, a significant amount of CO₂ is consumed by the buffering reactions instead of by CO₂RR. For every CO₂ molecule reduced, two OH⁻ are produced, which consume CO₂ for buffering. Simultaneously, the competing water reduction reaction also produces 2OH⁻ and consumes CO₂ for buffering. This self-consumption of CO₂ largely limits the reaction rate of CO₂RR, which explains why the

reaction never reaches its theoretical diffusion limited current density (101.4 mA cm⁻² in the case of 2500 rpm, detailed calculations are in the Supporting Information). This is a key intermediate conclusion, which we have drawn previously and now have quantitative pH data supporting it:⁵² under conditions of high mass transport, CO₂RR is never close to being mass transport limited. All relevant mass transport effects under these conditions are related to interfacial pH gradients. Therefore, the local concentrations of the carbonaceous species can be estimated from the local pH.

Interfacial pH and mass transport. Previous work has shown that the faradaic efficiency of CO₂RR on Au increases with rotation rate, mainly because of suppression of the competing

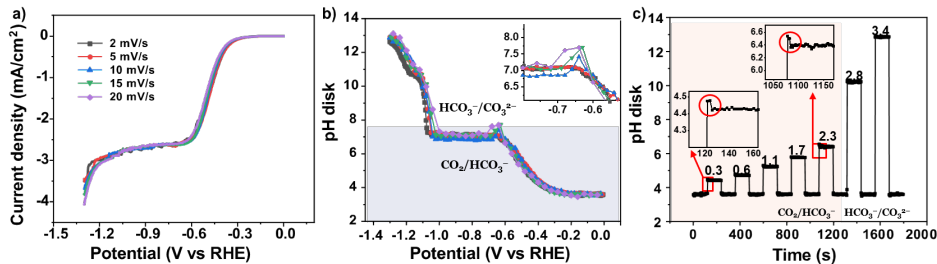


Figure 2. a) Cyclic voltammograms in CO₂-saturated 30 mM NaClO₄ (pH=3, acidified with 1mM HClO₄) at different scan rates. b) Variation of the interfacial pH as a function of potential during the cyclic voltammetry from a). c) Variation of the interfacial pH during chronopotentiometry in the same electrolyte, where CO₂RR on the disk electrode is turned “on” and “off” at different current densities (shown above the plot, in mA cm⁻²) every 2 minutes. The rotation rate of RRDE is 2500 rpm.

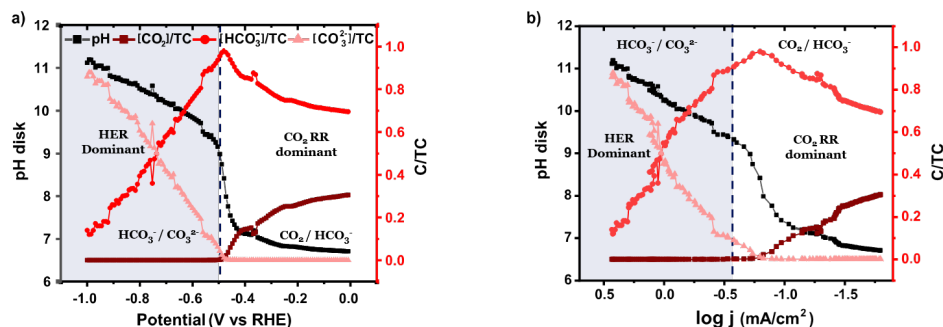


Figure 3. Variation of concentrations of carbonaceous species with a) potential and b) logarithm of the current density. The concentrations are calculated from the measured pH from Figure 1, using the equilibrium equations. TC is the total concentration of all the carbonaceous species. The black curve reports the measured pH and the red shades the concentrations of each species normalized to TC.

water reduction reaction.¹¹ A decrease in the interfacial pH by enhanced mass transport has been assumed to be the underlying reason, since the water reduction reaction is favored by alkalinity.^{15, 53} To verify this effect, variation of the interfacial pH is recorded under different rotation rates. The results show that the interfacial pH lowers by one unit as the rotation increases from 1000 rpm to 2500 rpm (Figure 4b-c), as the OH⁻ generated by CO₂RR and HER is transported away from the interface faster with the increasing rotation rate. It is illustrated that increasing mass transport decreases the interfacial pH, and thereby enhances the selectivity towards CO₂RR by slowing down the water reduction reaction. This explains the subtle change of total current density with increasing rotation rate (Figure 4a): both CO₂RR and water reduction are affected by the decreased interfacial pH. The water reduction reaction is slowed down while CO₂RR is slightly favored.²⁶ Remarkably, as a result of the fast generation of OH⁻, the interfacial pH is still 4 units larger than the bulk value under the highest rotation rate, highlighting the large difference between the interfacial environment and the bulk phase, and the relatively limited effect that enhancing mass transport has in suppressing this difference.

Interfacial pH and buffer capacity. As mentioned before, the concentration of bicarbonate buffer is expected to strongly affect the interfacial pH. To probe the variation of the interfacial pH in electrolytes with different buffer capacities, measurements were performed in CO₂-saturated bicarbonate electrolyte containing different bicarbonate concentrations. The cation concentration is kept constant at 0.5 M by adding appropriate amounts of sodium perchlorate, to deconvolute the effects from bicarbonate and cation concentration. Figure 5a shows that the current density is largely enhanced with increasing bicarbonate concentration, which is primarily due to the increasing bicarbonate reduction (Eq.7).²⁷ Still, thanks to the competent buffer ability of bicarbonate, the interfacial pH decreases significantly from 11 to 9 in the HCO₃⁻/CO₃²⁻ buffering range with increasing buffer capacity (Figure 5b), even with more OH⁻ generated from the higher current density. This is in agreement with the results from Tackett et al.⁴⁵: the variation of the interfacial pH becomes less pronounced and less intense in 0.5 M KHCO₃. When plotting as a function of current density (Figure 5c), the decrease of interfacial pH with increasing buffer capacity is even more pronounced. Instead of a sudden change in pH as observed in a weakly buffered environment, the variation of pH happens at a lower rate with a higher concentration of bicarbonate. Figure 5d displays the evolution of the relative concentration of CO₂ compared to total carbon with current density. Despite a similar interfacial concentration of CO₂ at low potentials, compared with more weakly buffered electrolytes, the pH in strongly buffered electrolytes evolves much slower, so the exhaustion of interfacial CO₂ is

postponed. Importantly, by comparing Figures 4 and 5, we can conclude that a suppression of interfacial pH gradients is more effectively achieved by buffering than by improving mass transport. However, as mentioned above, a higher bicarbonate concentration will also

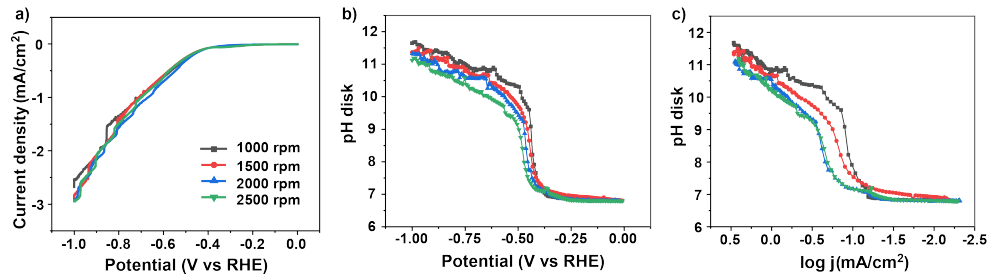


Figure 4. a) Cyclic voltammograms under different rotation rates in CO₂ saturated 0.1 M NaHCO₃ at 2 mV s⁻¹. Variation of the interfacial pH as a function of b) potential and c) the logarithm of the current density during the cyclic voltammetry from a).

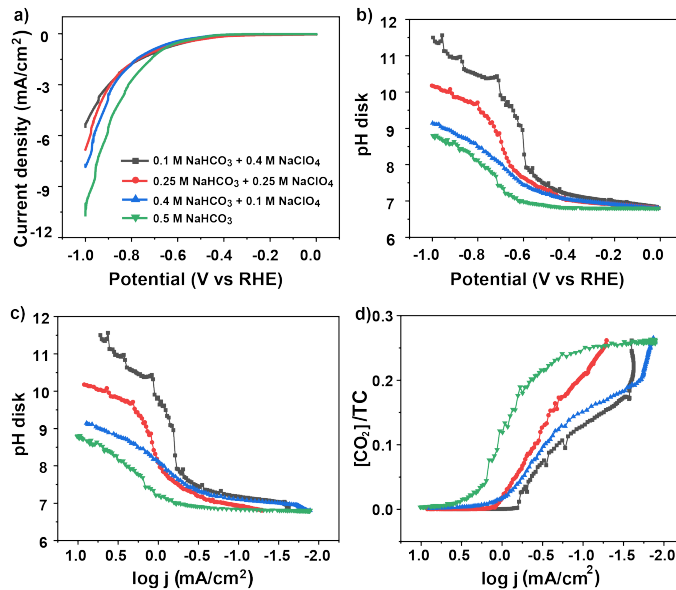


Figure 5. a) Cyclic voltammograms in CO₂-saturated bicarbonate electrolytes with increasing buffer capacity, at 2 mV s⁻¹ and a rotation rate of 2500 rpm. Variation of the interfacial pH as a function of b) potential and c) the logarithm of the current density. d) The calculated concentrations of CO₂ during the cyclic voltammetry from a).

promote H₂ production, due to Eq.7, and hence the FE towards CO₂RR products may still be negatively affected.

Interfacial pH and cation effect. As mentioned in the Introduction, the rate of CO₂RR varies with different alkali cations, which has been suggested to be related to their different buffering ability.²³ To verify this, the interfacial pH is monitored during CO₂RR in CO₂ saturated bicarbonates with different alkali cations. The current density here increases in the order: Li⁺ < Na⁺ < K⁺ < Rb⁺ < Cs⁺ (Figure 6a), in agreement with the results reported in the literature. This increase from Li⁺ to Cs⁺ is ascribed to the enhancement of both CO₂RR and HER, due to a stronger tendency to interact and stabilize the negatively charged reaction intermediate of CO₂RR and HER and a higher interfacial concentration of Cs⁺.^{8,15} The results in Figure 6b show that the interfacial pH decreases from Li⁺ to Cs⁺, demonstrating the different buffering effect of the cations with high sensitivity and pH resolution. According to Singh et al,²³ the buffering ability of cations originates from the hydrolysis of the water

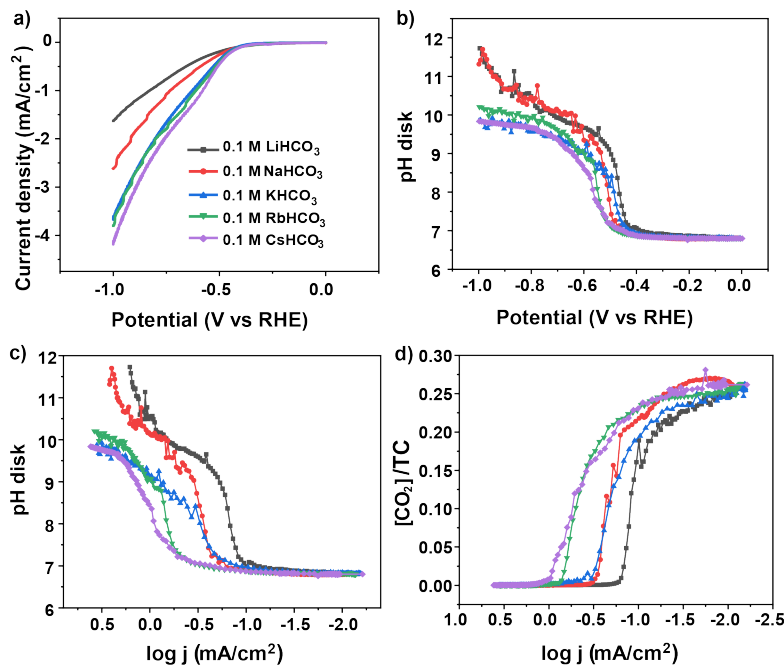


Figure 6. a) Cyclic voltammograms in 0.1 M CO₂-saturated bicarbonate electrolytes with different cations, at 2 mV s⁻¹ and a rotation rate of 2500 rpm. Variation of the interfacial pH as a function of b) potential and c) the logarithm of the current density. d) The calculated concentrations of CO₂ during the cyclic voltammetry from a).

molecules from the cation's hydration shell: once the pH around the cation reaches its pK_a , a hydronium ion will be generated. However, the trend in Figure 6b is clearly less pronounced compared to, for example, the effect of the bicarbonate buffer. Further increase of pH at high current densities is found for Li⁺ and Na⁺ (Figure 6c), attributed to a breakdown of the weak buffering capacity of Li⁺ and Na⁺ compared with the other cations. The variation of CO₂ concentration is shown in Figure 6d. Starting at a nearly identical initial value, a larger cation such as Cs⁺ exhibits a stronger resistance to the pH variation, leading to a longer retention of the interfacial CO₂ concentration.

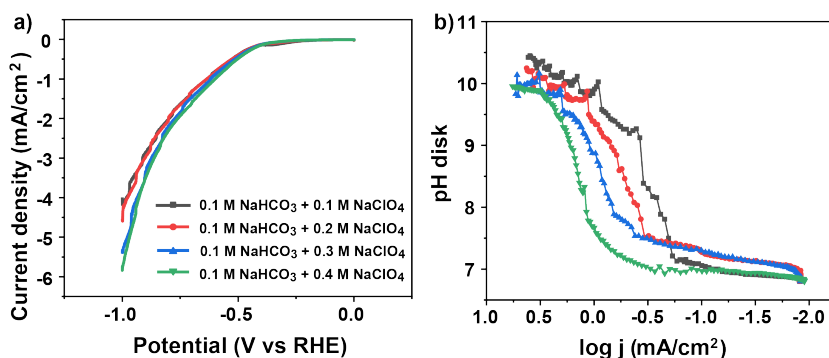


Figure 7. a) Cyclic voltammograms in CO₂-saturated electrolytes with different concentrations of Na⁺ at 2 mV s⁻¹ and a rotation rate of 2500 rpm. **b)** Variation of the interfacial pH as a function of the logarithm of the current density during the cyclic voltammetry from a).

To further test the buffer ability of alkali cations, the same experiments were conducted in a 0.1 M bicarbonate electrolyte with independently increasing the concentration of Na⁺ by adding NaClO₄. The results illustrate that the current density increases with the cation concentration while the interfacial pH decreases by the enhanced buffering ability (Figure 7a-b). However, comparing Figure 7 to Figure 5, the effect is clearly less than the effect of a “real” buffer like bicarbonate.

3.4 Conclusions

In this work, we have studied the variation of the interfacial pH during CO₂RR using a real-time pH sensor based on RRDE, which has been employed to follow the interfacial pH as a function of various electrolyte parameters. CO₂RR and HER lead to accumulation of OH⁻ near the electrode while the concurrent homogenous (buffer) reactions resist the corresponding pH changes.

It is observed that at low current density, the interfacial pH is close to 7, whereas with increasing current density there is a quick shift to an interfacial pH near 10-11, as expected from the pK_a 's of the two buffers. Scan rate dependent experiments show that the equilibrium of the $\text{CO}_2/\text{HCO}_3^-$ buffer is reached within ca. 10 s, such that at low scan rates ($\sim 2 \text{ mV s}^{-1}$) the buffering reactions can be considered in equilibrium and therefore the interfacial concentrations of different carbonaceous species can be calculated from the measured interfacial pH using equilibrium expressions. The experiments show that increasing mass transport, buffer capacity and the size and concentration of the cation can all help suppressing pH gradients near the electrode surface. Still, increasing buffer capacity has by far the largest effect. Increasing mass transport is not as efficient in resisting interfacial pH changes; in fact, the effect of mass transport by changing the disk rotation rate appears to be the smallest, at least in our experiments. The interfacial pH is still as high as 11 under strong forced convection (2500rpm). Moreover, CO_2RR may not benefit from increasing buffer or cation concentration, since the competing HER is typically more enhanced by that than the CO_2RR .

We chose here to study a relatively simple system (Au electrocatalyst, producing only CO and H_2) so that we could fully focus on the influence of the electrolyte parameters. Complementing previous work from our group regarding electrolyte effects on CO_2 reduction on gold, which have been summarized in a recent review,⁵² this study provides valuable new qualitative and quantitative insights on the role of the interfacial pH in the competition between CO_2 reduction and HER, and how it is affected by electrolyte properties. A key conclusion is that at on the (R)RDE, CO_2 reduction is never mass transport limited. The relevant concentration gradient in the system is built up due to the pH gradient existing between the electrode and the bulk electrolyte, and the most effective way to control this gradient is by buffering, not by improving mass transport. We expect this conclusion to be general, and transferable to more practical electrode geometries, such as gas diffusion electrodes. This conclusion should also be applicable to Cu electrodes at similar current densities and electrolyte conditions. Although the RRDE setup requires the use of a flat electrode, we have shown previously how learnings on the RDE can help in interpreting results obtained with a nanoporous electrode.⁵⁴

Summarizing, our research illustrates a remarkable difference between the interface and the bulk, even under strong forced convection. The 4-HATP/4-NSTP modified RRDE pH probe functions as an effective tool to probe the interfacial environment, which can also be applied in other electrochemical reactions. The cation effect, anion effect, and buffering effects and their influence on the local pH, are strongly coupled with each other, and the

RRDE pH probe presented here offers an excellent means for their deconvolution.

References

1 Y. Y. Birdja, E. Pérez-Gallent, M. C. Figueiredo, A. J. Göttle, F. Calle-Vallejo and M. T. M. Koper, *Nature Energy*, 2019, 4, 732-745.

2 B. A. Zhang, T. Ozel, J. S. Elias, C. Costentin and D. G. Nocera, *ACS Cent Sci*, 2019, 5, 1097-1105.

3 B. Deng, M. Huang, X. Zhao, S. Mou and F. Dong, *ACS Catalysis*, 2021, 12, 331-362.

4 Y. J. Sa, C. W. Lee, S. Y. Lee, J. Na, U. Lee and Y. J. Hwang, *Chem Soc Rev*, 2020, 49, 6632-6665.

5 A. Wagner, C. D. Sahm and E. Reisner, *Nature Catalysis*, 2020, 3, 775-786.

6 A. S. Malkani, J. Anibal and B. Xu, *ACS Catalysis*, 2020, 10, 14871-14876.

7 M. C. O. Monteiro, F. Dattila, N. Lopez and M. T. M. Koper, *J Am Chem Soc*, 2022, 144, 1589-1602.

8 M. C. O. Monteiro, F. Dattila, B. Hagedoorn, R. García-Muelas, N. López and M. T. M. Koper, *Nature Catalysis*, 2021, 4, 654-662.

9 H. Hashiba, L.-C. Weng, Y. Chen, H. K. Sato, S. Yotsuhashi, C. Xiang and A. Z. Weber, *The Journal of Physical Chemistry C*, 2018, 122, 3719-3726.

10 G. Marcandalli, A. Goyal and M. T. M. Koper, *ACS Catal*, 2021, 11, 4936-4945.

11 G. Marcandalli, M. Villalba and M. T. M. Koper, *Langmuir*, 2021, 37, 5707-5716.

12 K. J. P. Schouten, E. Pérez Gallent and M. T. M. Koper, *Journal of Electroanalytical Chemistry*, 2014, 716, 53-57.

13 A. S. Varela, M. Kroschel, N. D. Leonard, W. Ju, J. Steinberg, A. Bagger, J. Rossmeisl and P. Strasser, *ACS Energy Letters*, 2018, 3, 812-817.

14 Z. Zhang, L. Melo, R. P. Jansonius, F. Habibzadeh, E. R. Grant and C. P. Berlinguette, *ACS Energy Letters*, 2020, 5, 3101-3107.

15 A. Goyal and M. T. M. Koper, *Angew Chem Int Ed Engl*, 2021, 60, 13452-13462.

16 X. Lu, C. Zhu, Z. Wu, J. Xuan, J. S. Francisco and H. Wang, *J Am Chem Soc*, 2020, 142, 15438-15444.

17 R. E. Zeebe and D. Wolf-Gladrow, *CO₂ in seawater: equilibrium, kinetics, isotopes*, Gulf Professional Publishing, 2001.

18 K. G. Schulz, U. Riebesell, B. Rost, S. Thoms and R. E. Zeebe, *Marine Chemistry*, 2006, 100, 53-65.

19 M. Dunwell, X. Yang, B. P. Setzler, J. Anibal, Y. Yan and B. Xu, *ACS Catalysis*, 2018, 8, 3999-4008.

20 M. C. O. Monteiro, A. Mirabal, L. Jacobse, K. Doblhoff-Dier, S. C. Barton and M. T. M. Koper, *JACS Au*, 2021, 1, 1915-1924.

21 K. Yang, R. Kas and W. A. Smith, *J Am Chem Soc*, 2019, 141, 15891-15900.

22 M. C. O. Monteiro, A. Goyal, P. Moerland and M. T. M. Koper, *ACS Catal*, 2021, 11, 14328-14335.

23 M. R. Singh, Y. Kwon, Y. Lum, J. W. Ager, 3rd and A. T. Bell, *J Am Chem Soc*, 2016, 138, 13006-13012.

24 L. D. Chen, M. Urushihara, K. Chan and J. K. Nørskov, *ACS Catalysis*, 2016, 6, 7133-7139.

25 A. Frumkin, *Transactions of the Faraday Society*, 1959, 55, 156-167.

26 A. Goyal and M. T. M. Koper, *J Chem Phys*, 2021, 155, 134705.

27 G. Marcandalli, K. Boterman and M. T. M. Koper, *Journal of Catalysis*, 2022, 405, 346-354.

28 M. C. O. Monteiro and M. T. M. Koper, *Current Opinion in Electrochemistry*, 2021, 25, 100649.

29 B. P. Nadappuram, K. McKelvey, R. Al Botros, A. W. Colburn and P. R. Unwin, *Anal Chem*, 2013, 85, 8070-8074.

30 V. S. Joshi, P. S. Sheet, N. Cullin, J. Kreth and D. Koley, *Anal Chem*, 2017, 89, 11044-11052.

31 M. C. O. Monteiro, L. Jacobse and M. T. M. Koper, *J Phys Chem Lett*, 2020, 11, 9708-9713.

32 M. C. O. Monteiro, L. Jacobse, T. Touzalin and M. T. M. Koper, *Anal Chem*, 2020, 92, 2237-2243.

33 R. Song, Q. Xiong, T. Wu, X. Ning, F. Zhang, Q. Wang and P. He, *Anal Bioanal Chem*, 2020, 412, 3737-3743.

34 M. Etienne, P. Dierkes, T. Erichsen, W. Schuhmann and I. Fritsch, *Electroanalysis*, 2007, 19, 318-323.

35 C. Lindino and L. Bulhoes, *Analytica chimica acta*, 1996, 334, 317-322.

36 H. E. Lackey, G. L. Nelson, A. M. Lines and S. A. Bryan, *Anal Chem*, 2020, 92, 5882-5889.

37 O. Ayemoba and A. Cuesta, *ACS Appl Mater Interfaces*, 2017, 9, 27377-27382.

38 C. Zong, M. Xu, L. J. Xu, T. Wei, X. Ma, X. S. Zheng, R. Hu and B. Ren, *Chem Rev*, 2018, 118, 4946-4980.

39 W. Albery, *Transactions of the Faraday Society*, 1966, 62, 1915-1919.

40 A. M. Zimer, M. Medina da Silva, E. G. Machado, H. Varela, L. H. Mascaro and E. C. Pereira, *Anal Chim Acta*, 2015, 897, 17-23.

41 Y. Yokoyama, K. Miyazaki, Y. Miyahara, T. Fukutsuka and T. Abe, *ChemElectroChem*, 2019, 6, 4750-4756.

42 M. C. O. Monteiro, X. Liu, B. J. L. Hagedoorn, D. D. Snabilié and M. T. M. Koper, *ChemElectroChem*, 2021, 9.

43 W. J. Albery and E. J. Calvo, *Journal of the Chemical Society, Faraday Transactions 1: Physical Chemistry in Condensed Phases*, 1983, 79, 2583-2596.

44 P. Steegstra and E. Ahlberg, *Journal of Electroanalytical Chemistry*, 2012, 685, 1-7.

45 B. M. Tackett, D. Raciti, N. W. Brady, N. L. Ritzert and T. P. Moffat, *The Journal of Physical Chemistry C*, 2022, 126, 7456-7467.

46 Y. Yokoyama, K. Miyazaki, Y. Kondo, Y. Miyahara, T. Fukutsuka and T. Abe, *Chemistry Letters*, 2020, 49, 195-198.

47 F. Zhang and A. C. Co, *Angewandte Chemie International Edition*, 2020, 59, 1674-1681.

48 G. Marcandalli, M. C. O. Monteiro and M. T. M. Koper, *Phys Chem Chem Phys*, 2022, 24, 2022-2031.

49 P. Steegstra and E. Ahlberg, *Electrochimica Acta*, 2012, 76, 26-33.

50 L. J. Henderson, *American Journal of Physiology-Legacy Content*, 1908, 21, 173-179.

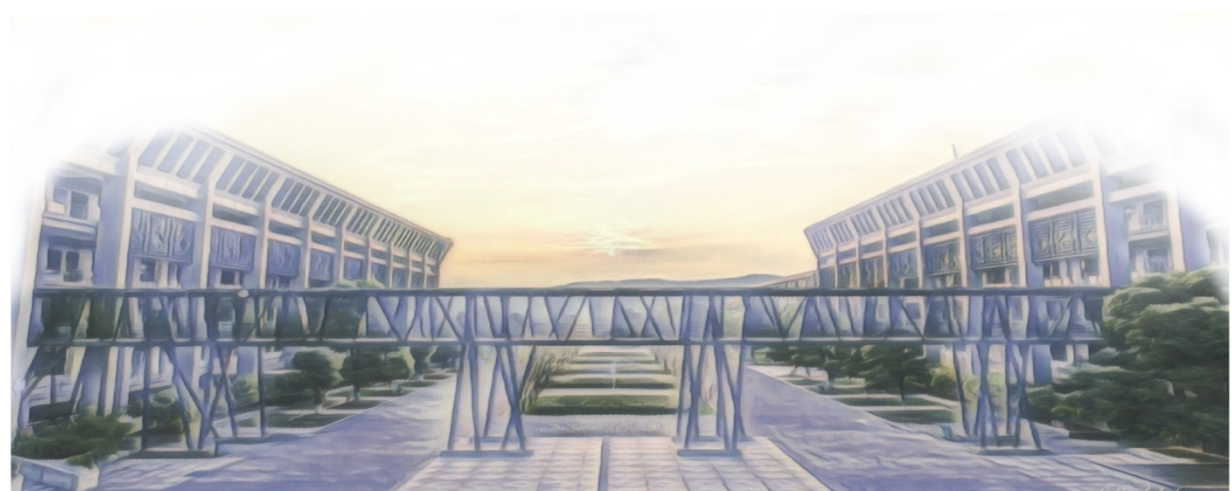
51 H. Zhong, K. Fujii, Y. Nakano and F. Jin, *The Journal of Physical Chemistry C*, 2014, 119, 55-61.

52 G. Marcandalli, M. C. O. Monteiro, A. Goyal and M. T. M. Koper, *Acc Chem Res*, 2022, 55, 1900-1911.

53 A. Goyal, G. Marcandalli, V. A. Mints and M. T. M. Koper, *J Am Chem Soc*, 2020, 142, 4154-4161.

54 A. Goyal, C. J. Bondue, M. Graf and M. T. M. Koper, *Chem Sci*, 2022, 13, 3288-3298.

55 E. W. Davey, J. H. Gentile, S. J. Erickson and P. Betzer, *Limnology and Oceanography*, 1970, 15, 486-488.



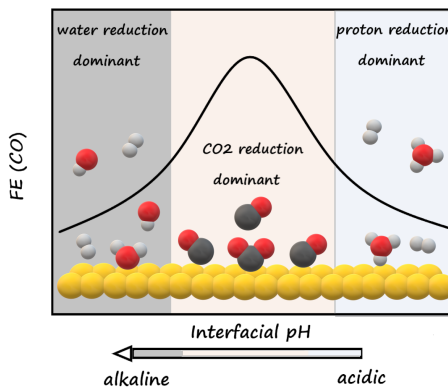
Chapter 4

Tuning the Interfacial Reaction Environment for CO₂ Electroreduction to CO in Mildly Acidic Media



Abstract

A considerable carbon loss of CO_2 electroreduction in neutral and alkaline media severely limits its industrial viability, as a result of the homogeneous reaction of CO_2 and OH^- under interfacial alkalinity. Here, to mitigate homogeneous reactions, CO_2 electroreduction is conducted in mildly acidic media. By modulating the interfacial reaction environment *via* multiple electrolyte effects, the parasitic hydrogen evolution reaction is suppressed, leading to a faradaic efficiency over of 80% for CO on the planar Au electrode. Using the Rotating Ring-Disk Electrode technique, the Au ring constitutes an in-situ CO collector and pH sensor, enabling the recording of the Faradaic efficiency and monitoring of interfacial reaction environment while CO_2 reduction takes place on the Au disk. The dominant branch of hydrogen evolution reaction switches from the proton reduction to the water reduction as the interfacial environment changes from acidic to alkaline. By comparison, CO_2 reduction starts within the proton reduction region as the interfacial environment approaches near-neutral conditions. Thereafter, proton reduction decays while CO_2 reduction takes place, as the protons are increasingly consumed by the OH^- electrogenerated from CO_2 reduction. CO_2 reduction reaches its maximum Faradaic efficiency just before the water reduction initiates. Slowing the mass transport lowers the proton reduction current while CO_2 reduction is hardly influenced. In contrast, appropriate protic anion, e.g. HSO_4^- in our case, and weakly hydrated cations, e.g. K^+ , accelerate CO_2 reduction, with the former providing extra proton flux but higher local pH, and the latter stabilizing the $^*\text{CO}_2^-$ intermediate.



This chapter is based on Liu, X.; Koper, M. T. M., Tuning the Interfacial Reaction Environment for CO_2 Electroreduction to CO in Mildly Acidic Media. *J Am Chem Soc*, 2024, 146 (8), 5242-5251

4.1 Introduction

The electroreduction of CO₂ driven by sustainable energy is envisaged to be an important stride towards a carbon-neutral cycle.¹⁻⁴ In such a cycle, waste or air-captured CO₂ is reduced back to a broad spectrum of valuable feedstocks, among which carbon monoxide (CO) is of primary interest, due to its economic viability and spectrum of chemical applications.⁵ As an important intermediate and building block, CO can be readily reduced to multi-carbon products, either by electroreduction⁶ or by the thermocatalytic Fischer-Tropsch process.⁷

The electrocatalytic CO₂ Reduction Reaction (CO₂RR) to CO is commonly operated in neutral or alkaline bicarbonate electrolytes, to suppress the parasitic Hydrogen Evolution Reaction (HER). Extensive efforts have been devoted to designing better CO₂RR catalysts.³⁻⁴ Still, considerable carbon loss during CO₂RR due its conversion to carbonate in an alkaline reaction environment severely limits its practical feasibility. According to various studies so far, it is commonly believed that HCO₃⁻ and CO₃²⁻ are not directly reduced on a bare gold electrode,⁸⁻⁹ but rather function as a potential carbon supply⁸ for CO₂RR and as proton donor¹⁰⁻¹¹ for HER. Hence, the generation of HCO₃⁻ and CO₃²⁻ by homogeneous reactions severely compromises the carbon efficiency of CO₂RR. This “carbonate problem” has been considered by Kanan et al¹² to be the biggest obstacle to real-world applications of CO₂RR. The “carbonate problem” means that, in addition to being reduced on the electrode surface, CO₂ is also consumed by the electrogenerated OH⁻ to produce HCO₃⁻ or CO₃²⁻ according to reaction eqs. 1-2, which are thermodynamically favorable in alkaline media:



Due to the proton-coupled electron transfer nature of CO₂RR and HER, every electron transferred at the interface generates one OH⁻, resulting in a local alkaline environment and the conversion of CO₂ to HCO₃⁻ or CO₃²⁻ in the electrolyte, decreasing the carbon efficiency and multiplying the cost for downstream processing, e.g. regenerating CO₂ from carbonate. In that sense, the larger the current density, the lower carbon efficiency, thereby largely limiting the industrial practicality of CO₂RR.

To circumvent the “carbonate problem”, CO₂RR in acidic media has recently emerged as a possibly attractive alternative.¹³⁻¹⁴ However, the low bulk pH brings about the strong competition from HER due to proton reduction (as opposed to HER from water reduction in neutral and alkaline media), lowering the FE of CO₂RR. Studies on acidic CO₂RR have focused on promoting CO₂RR and suppressing HER in acidic media, mainly by suitable design of the electrolyzer configuration,¹⁵ catalyst engineering,¹⁶⁻²¹ and electrolyte modification.^{13,22-25} Oßkopp et al¹⁵ studied the FE and the local pH of a tin-oxide catalyst on

gas diffusion electrodes (GDEs) in different cell configurations, and found that a divided cell with a zero-gap anode is capable to producing undissociated formic acid, suggesting that the (local) pH remains lower than the pKa of formic acid (pKa = 3.77). Also, tuning the structure and composition of catalysts may effectively enhance the activity and selectivity of CO2RR. Confinement in nanostructures has been suggested to increase the local concentration of alkali cations and inhibit proton diffusion or kinetically reduce the local proton concentration, leading to a higher FE of CO2RR,¹⁶⁻¹⁷ while bimetallic catalysts have been suggested to weaken H binding which combined with a high affinity for CO2RR reaction intermediates promotes C–C coupling.¹⁹ Organic polymer-modified electrodes change the hydrophobicity of the electrode and the proton activity near the surface, hence tailoring the proton transfer rates at the interface.^{21,26} Besides, electrolyte conditions have a profound effect on the interfacial reaction environment.^{6,27-29} Weakly hydrated cations such as K⁺ and Cs⁺ are indispensable for CO2RR in acidic media^{14,17,30-31} due to their stabilization of reaction intermediates through electrostatic interaction.^{25,30,32} Alkali cations have also been proposed to modify the local electric field in the double layer,^{23,32} buffer the interfacial pH under an alkaline local environment,³³⁻³⁵ and suppress the migration of hydronium ions to the surface.²³⁻²⁴ Indeed, mass transport crucially influences the competition between CO2RR and HER. Bondue et al¹³ used Differential Electrochemical Mass Spectroscopy (DEMS) with a dual-compartment flow cell to study CO2RR on Au electrodes in mildly acidic media and proposed that HER can be suppressed if the rate of CO2RR matches the mass transport rate of protons, as OH⁻ formation from CO2RR is then sufficient to neutralize protons near the electrode before they discharge to produce hydrogen. The applicability of this idea in practical gas-diffusion electrode (GDE) geometries has been verified by Monteiro et al.²²: the FE of CO2RR reaches over 80% at current densities up to 200mA cm⁻² on 10 cm² Au GDEs in acidic media.

Given the great importance of the near-electrode electrolyte conditions, and especially interfacial pH, during acidic CO2RR, systematic studies with *operando* techniques are important to uncover real-time information about the interfacial reaction environment and devise suitable strategies to tune the local environment. The Rotating Ring-Disk Electrode (RRDE) technique is a powerful electroanalytical tool in studies of CO2RR. The well-defined mass transport conditions of RRDE renders the ring electrode a quantitative collector of the two main products generated from the disk electrode during CO2RR, namely CO and OH⁻, as has been shown in our previous works.^{34,36-38} As a selective CO-producing⁹ and an excellent CO-oxidation³⁹ catalyst, a Au ring and disk were used throughout the study, so that only CO and H₂ were generated on the disk and CO was oxidized exclusively on the Au ring,³⁶ enabling us to deconvolute CO2RR and HER in the RRDE setup. Furthermore, we

believe that the pH (and CO) sensor being remote from the reaction interface is one of the advantages of our device, as the measurements are conducted without disturbing the reaction environment. Due to the good time resolution of the RRDE pH sensor, we are able to trace the evolution of the interfacial environment during transient techniques, e.g. cyclic voltammetry,^{34,37} in combination with well-defined mass transport conditions. It is very difficult to detect the interfacial pH under the same reaction conditions as RRDE by other techniques such as *in situ* spectroscopies. pH measurements by *in situ* spectroscopy are mostly performed with special electrochemical cells, which greatly impacts the mass transport. Moreover, in spectroscopy, the ratio of the integrated peak areas between CO₂ and HCO₃⁻ is commonly used to determine the interfacial pH during CO₂RR.^{35,40} This compromises the time resolution of the measurements, as the equilibrium between CO₂ and HCO₃⁻ is established slowly,⁴¹ making it more difficult to record the interfacial pH accurately during cyclic voltammetry. A disadvantage of the RRDE technique is that it measures the pH at the ring, which then needs to be converted mathematically to the pH at the disk. This requires a model, i.e. knowledge of all relevant acid-base equilibria in the system, which in a complex environment may lead to inaccuracies if certain equilibria are not included. An additional disadvantage of the RRDE method may be that it is less local or interface specific than vibrational methods. For instance, Sum Frequency Generation spectroscopy can estimate the local pH on a molecular length scale.⁴² RRDE averages out the pH gradients in the lateral directions. In the direction perpendicular to the electrode, RRDE measures the pH on a local scale that is consistent with a continuum description, which is certainly less than molecular, but still relevant to describe local concentration gradients.

In this work, we probe the interfacial pH using a modified Au ring electrode and measure both the FE of CO and the interfacial pH during acidic CO₂RR on a Au disk electrode. The measurement of reaction selectivity and interfacial pH allows us to study in quantitative detail the relation between interfacial environment and the relevant reactions: specifically, the interaction between CO₂RR and two main branches of HER, namely proton reduction and water reduction, can be elucidated. Additionally, the influence of different electrolyte conditions such as anion identity, cation identity, and mass transport rate on the interfacial environment and the reaction selectivity can be explored quantitatively. A proper protic anion, a weakly hydrated cation and slow mass transport conditions are demonstrated to improve the FE of CO₂RR on a Au electrode in acidic media. Since these parameters primarily reflect the electrolyte, we expect these conclusions to generalize to other electrode materials and structures.

4.2 Experimental section

Chemicals and Materials. Electrolytes were prepared with ultrapure water (>18.2 MΩ cm, Millipore Milli-Q) and the following chemicals: Li₂SO₄ (>99.99%, trace metal basis, Sigma-Aldrich), Na₂SO₄ (anhydrous, 99.99% Suprapur, Sigma-Aldrich), K₂SO₄ (>99.99%, trace metal basis, Sigma-Aldrich), NaClO₄·H₂O (>99.99%, trace metal basis, Sigma-Aldrich), NaH₂PO₄ (99.998%, trace metals basis, Sigma-Aldrich) and H₂SO₄ (96% Suprapur, Merck). The pH of the electrolytes was adjusted by H₂SO₄ (96% Suprapur, Merck) and HClO₄ (70% Suprapur, Merck.). All electrolytes were purged with either Ar (6.0 purity, Linde, 20 min) or CO₂ (4.5 purity, Linde, 20 min) before experiments. All the electrochemical experiments were performed in home-made single compartment electrochemical cells, controlled by a four-channel Biologic potentiostat (VSP-300) and a Modulated Speed Rotator (Pine Research). A three-electrode system was employed in all the electrochemical measurements with a ring-disk electrode (E6/E5 ChangeDisk, PEEK Shroud, Pine Research), a Au wire (0.5 mm diameter, MaTeck, 99.9%) and a Ag/AgCl electrode (RE-1B, 3 M NaCl, Biologic, inserted in a Luggin capillary) as the working electrode, counter electrode and reference electrode, respectively. The electrochemical cells and other glassware were kept in KMnO₄ solution (1 g L⁻¹ KMnO₄ in 0.5 M H₂SO₄) overnight. Before experiments, they were immersed in dilute piranha to remove the generated MnO_x and the residual KMnO₄, followed by rinsing and boiling in ultrapure water five times.

Preparation and modification of the electrodes. The RRDE tip was polished with 3 µm, 1 µm, 0.25 µm diamond suspension (MetaDi, Buehler) respectively with the Au disk (D = 5mm) inserted in the Au ring matrix (D_{inner} = 6.5 mm, D_{outer} = 7.5 mm). It was sonicated in ethanol and ultrapure water for 5 min in between each polishing step. Then, the Au ring and disk electrodes were short-circuited and electropolished in 0.1 M H₂SO₄ by cycling between 0 and 1.75 V vs RHE at 1 V s⁻¹ (Ar-saturated) for 200 times, followed by cyclic voltammetry under the same condition at 100 m V s⁻¹ on Au ring and disk electrode separately, to characterize the surface and calculate the electrochemical surface area (ECSA) by dividing the charge of the Au oxide reduction peak by the charge density of a Au oxide monolayer (386 µC cm⁻²) (see Figure S1 in the Supporting Information).

Interfacial pH measurements. The pH sensor coupled with RRDE has been developed in our group, the details are given in our previous works.^{34,37} Briefly, the Au ring electrode was modified by a monolayer of 4-nitrothiophenol (4-NTP) by dipping the RRDE tip (with a Au ring and a Teflon disk) in a 1 mM ethanal-dissolved 4-NTP (80%, Merck) solution for 20 min. The 4-NTP is then converted to the pH sensing couple 4-hydroxylaminothiophenol/4-nitrosothiophenol (4-HATP / 4-NSTP), whose redox potential is pH dependent, by cyclic voltammetry in 0.1 M H₂SO₄ from 0.68 to 0.11 V vs RHE at 100 mV s⁻¹.

During the pH measurements, the potential of the Au disk was swept negatively from 0 V vs RHE in different electrolytes at 2 mV s⁻¹. Simultaneously, the peak potentials of the 4-HATP/4-NSTP redox couple on the ring were continuously monitored by cyclic voltammetry at 200 mV s⁻¹. The peak potentials shift as the interfacial environment of the ring electrode evolves with the reactions occurring on the disk electrode. Hence, the cycling range of pH sensor was tuned if necessary. For instance, during the measurements in 0.1 M Na₂SO₄ (pH=3), the potential window on the ring was kept as -0.05 V to 0.35 V vs Ag/AgCl from the start to -0.5 V vs RHE on the disk. It was then changed to -0.15 V to 0.25 V vs Ag/AgCl as the interfacial environment became less acidic. The gases (CO₂ or Ar) were kept purging into the electrolyte during the measurements to eliminate any interference from oxygen. Details of the calculations of the interfacial pH at the disk are explained in the Supporting Information. All pH data reported in the following Figures are calculated pH data for the disk electrode. The actually measured ring pH data are collected in the Supporting Information section "Ring pH data".

Faradaic Efficiency measurements. The CO sensing method based on RRDE has been developed by our group and has been applied in multiple investigations. The detailed procedure is described in the previous publications.^{11,36,38} In this work, the Faradaic Efficiency measurement was carried out subsequently to the interfacial pH measurement on the same Au disk electrode. After the pH measurement, the Au disk was disassembled from the RRDE tip, and the Au ring matrix was coupled with a Teflon disk to be repolished and sonicated following the procedure mentioned above, to remove the pH sensing monolayer. Next, the Au disk was reassembled in the Au ring matrix, followed by electropolishing and characterization as aforementioned. To eliminate the interference from bubbles during measurements, the PEEK shroud and the Teflon spacer between the ring and disk electrode were coated with dopamine, to increase their hydrophilicity, by immersing the RRDE tip in 0.1 M NaHCO₃ dissolved 2 g/L dopamine hydrochloride for 1 hour at about 55°C, with the rotation rate at 450 rpm. Then, the Au ring and disk electrode were electropolished in 0.1 M H₂SO₄ again to remove the dopamine residue from the Au electrode surface. Subsequently, the Au ring and disk electrode were characterized again in 0.1 M H₂SO₄. The cyclic voltammograms derived agree well with the ones obtained before the dopamine coating and the ones before interfacial pH measurements, suggesting the complete elimination of the dopamine residue and no detectable variation of the electrode surface during the process (Figure S1). During the FE measurement, the Au disk was cycled from 0 to around -1.5 V vs RHE in different electrolytes at 2 mV s⁻¹, while the Au ring potential was set as 1 V vs RHE to oxidize the CO generated on the disk electrode. At this potential, CO oxidation is diffusion limited in bicarbonate solution. In phosphate-containing

solution, the current is slightly below the diffusion-limited current at 1 V, approaching diffusion limitation at higher (interfacial) pH.⁴³ This means that in solution with more strongly adsorbing anions (such as sulfate and phosphate), the actual CO concentration may be slightly underestimated, though we expect the error to be small if the interfacial pH is high. The apparent collection efficiency of the ring was determined at the end of the measurements, to inspect if there was any deviation from the theoretical value due to changes in geometry during assembling of the tip. The apparent collection efficiency was measured in 5 mM K₃Fe(CN)₆ dissolved in 0.1 M NaHCO₃, during which the disk was cycled from 0.27 to 1.27 V vs RHE, while the ring potential was set to 0.96 V vs RHE. The collection efficiency was determined for each rotation rate and was calculated according to Eq. 3.

$$N = \left| \frac{i_{ring}}{i_{disk}} \right| \quad (3)$$

Details of the calculations of the Faradaic Efficiency are explained in the Supporting Information.

4.3 Results and discussion

For each interfacial pH measurement, the pH is recorded by the highly sensitive pH sensor on the ring, and then converted to the pH disk according to the equations originally derived by Albery and Calvo.⁴⁴ We have also introduced a buffering correction in the calculation to compensate for the deviation caused by the presence of buffering species. Detailed calculations and the pH profiles of RRDE in different electrolytes are explained in the Supporting Information. We note that in this work we semi-quantitatively correlate the changes in the interfacial pH values during cyclic voltammetry with different electrolyte parameters, such as anion identity, cation identity, and rate of mass transport, instead of asserting absolute accuracy of individual pH values.

Interfacial pH and FE measurements were first carried out in 0.1M NaClO₄ with the bulk pH adjusted to 3. As depicted in Figure 1a, an increase in current density is observed at around -0.3 V, which is ascribed to the proton reduction. Depending on the proton source, HER in an aqueous solution takes place through either the proton reduction reaction (eq. 4) or the water reduction reaction (eq. 5).



As only traces of CO are detected there (Figure 1b), the first region is dominated by the proton reduction reaction. Between -0.6 V and -1.1 V, the current corresponds to mass transport limited proton reduction. However, as illustrated in Fig.1b, the current due to CO₂RR discernibly increases, with a corresponding decrease in HER current. Interestingly, the total current remains constant. During the mass transport limited proton reduction, the

interfacial pH near the disk electrode is ca.5. This pH is lower than the pH of 7 measured previously in the absence of CO₂ (though in sulfate electrolyte), which must be due to a buffering effect of the CO₂. Since CO₂RR is a cation-coupled electron transfer reaction,³⁰ Bondue et al.¹³ have previously argued that OH⁻ is generated from CO₂RR (Eq. 6),



which reacts with “incoming” protons. This explains the correspondence between the CO₂RR increase and HER decrease. With increasingly negative potential, the CO₂RR rate increases and more protons are neutralized by OH⁻ before reaching the surface, thereby suppressing the proton reduction further. At around -1.2 V, water reduction initiates, causing a sharp increase in the total current density and a decay of the FE for CO (Figure 1c), even though the partial current density of CO₂RR still rises.

With increasing current density in water reduction region, the interfacial pH rises rapidly from -1.3 V, due to the small buffer capacity of the electrolyte, as there is only 35 mM carbonaceous buffering species (CO₂: buffer range 5.3-7.3; HCO₃⁻: buffer range: 9.3-11.3) in the bulk phase. This is in agreement with previous studies^{19,45-47} showing that the interfacial environment during CO₂RR and HER in weakly-buffered acid turns highly alkaline. The interfacial pH is most effectively lowered by increasing concentration of buffering species. Our previous work³⁴ showed that the interfacial pH during CO₂RR decreases from 11 to 9 as the concentration of HCO₃⁻ increases from 0.1 M to 0.5 M. The decline in the FE for CO is in agreement with the studies in neutral bicarbonate media: the FE of CO on a planar Au electrode reaches its maximum just before the onset potential of water reduction, with the interfacial environment turning alkaline.^{11,36} While CO₂RR can suppress proton reduction under appropriate conditions, it does not compete effectively with water reduction at these negative potentials. This is partially due to the substantial consumption of CO₂ by chemical reactions *via* Eqs. 1-2 under the highly alkaline interfacial environment during water reduction.

Interfacial pH and FE measurements were also performed in 0.1M Na₂SO₄ (acidified to pH=3), to study the effect of a different anion. As in NaClO₄, there are discernable regions for proton and water reduction, as shown in Figure 2a. Compared to results in NaClO₄, the onset potential of proton reduction in Na₂SO₄ has shifted slightly negatively, likely related to the specific adsorption of SO₄²⁻ on the Au surface.⁴⁸ Surprisingly, a higher limiting current density is obtained in Na₂SO₄, with an identical bulk pH as NaClO₄. Due to this larger current density, by the end of the proton reduction region, the interfacial pH has increased up to 7, indicating a closely neutral interfacial environment, which could be beneficial for CO₂RR. This is illustrated in Figure 2b: the current density of CO₂RR in Na₂SO₄ is nearly four times larger than that in NaClO₄, leading to a faster consumption of protons and a remarkable

decay in the proton reduction. By the end of mass transport limited region, the FE of CO reaches 60% in Na_2SO_4 , which is about 1.5 x larger than that in NaClO_4 , but it drops quickly as the water reduction starts (Figure 2c).

To carefully inspect this increasing limiting current density in SO_4^{2-} , measurements were performed in electrolytes containing different SO_4^{2-} concentrations from 0 to 200 mM with a bulk pH of 3. The cation concentrations were kept to be 0.2 M by adding different amounts of NaClO_4 . Figure 3a-b depicts the variation of the current densities with SO_4^{2-} concentration in Ar and CO_2 atmosphere respectively. As the limiting current density is determined by the

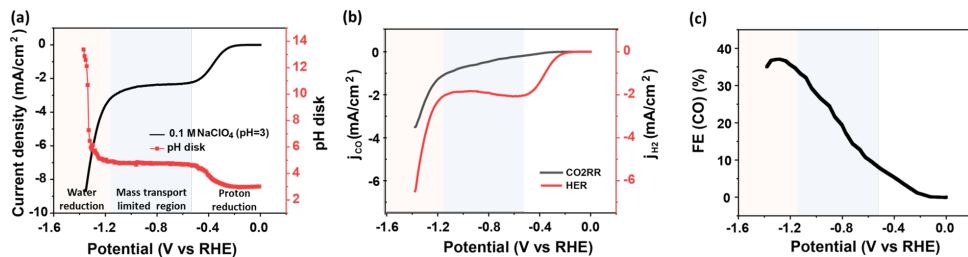


Figure 1. a) Variation of the interfacial pH recorded during cyclic voltammetry in 0.1 M CO_2 -saturated NaClO_4 with a bulk pH of 3, at 2 mV s^{-1} and a rotation rate of 2500 rpm: the black line and the red curve refer to the current density and to the corresponding interfacial pH during the negative-going scan, respectively. b) The partial current density of CO2RR (black curve) and HER (red curve) during the cyclic voltammetry from a) c) The Faradaic efficiency of CO during the cyclic voltammetry as derived from a). The potentials in all figures have been converted to the RHE scale using the bulk pH.

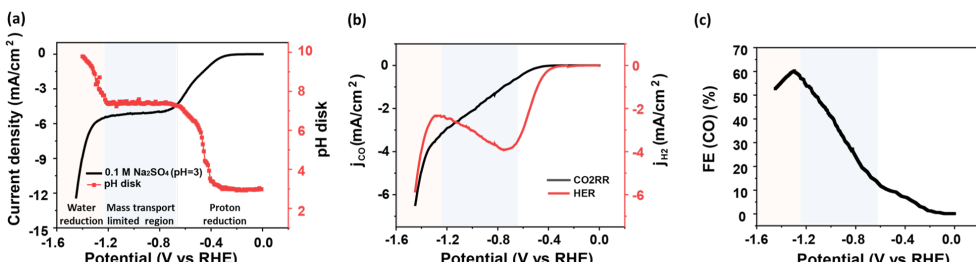


Figure 2. a) Variation of the interfacial pH recorded during cyclic voltammetry at 2 mV s^{-1} and a rotation rate of 2500 rpm in 0.1 M CO_2 -saturated Na_2SO_4 with a bulk pH of 3: the black line and the red curve refer to the current density and to the corresponding interfacial pH during the negative-going scan, respectively. b) The partial current density of CO2RR (black curve) and HER (red curve) during the cyclic voltammetry from a). c) The Faradaic efficiency of CO during the cyclic voltammetry as derived from a).

total concentration of the proton sources in the bulk phase, the increase in limiting current density with SO₄²⁻ concentration in Figure 3a signifies a higher concentration of proton donors in solution, which are not only the hydronium cations, but also any conjugated acid in the electrolyte that is able to deprotonate and release protons. Coupling to acid-base equilibria in solution has been shown to give higher mass-transport limited currents; for a mathematical treatment, see the original work of Koutecky and Levich⁴⁹ and of Rebouillat et al.⁵⁰ In 0.1 M CO₂-saturated Na₂SO₄ at a bulk pH of 3, other than 1 mM hydronium cations, there are 9 mM of HSO₄⁻ in the bulk electrolyte. The effective buffer range of HSO₄⁻/SO₄²⁻ is 0.99–2.99. The interfacial pH increases out of this pH range after -0.3 V, making the HSO₄⁻ here behave more like a proton donor rather than an effective buffer. As the potential shifts negatively, the concentration of protons and HSO₄⁻ near the interface consistently decrease. As a result of this pH gradient, HSO₄⁻ dissociates and releases a proton *via* eq. 7.



When reaching the vicinity of the surface, the proton flux from HSO₄⁻ adds to the overall proton reduction or neutralization of OH⁻ generated from CO₂RR. With the added proton flux from HSO₄⁻, larger proton reduction currents are observed accordingly. Interestingly,

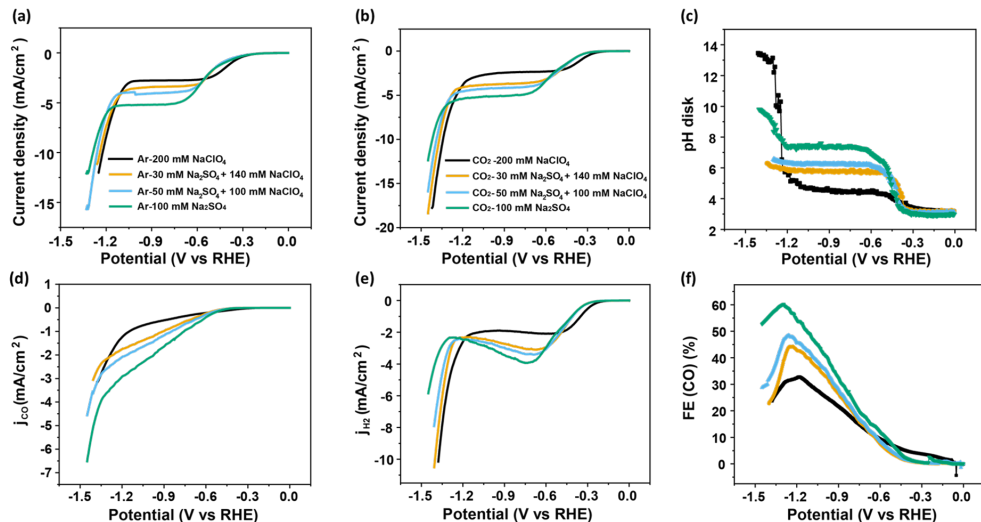


Figure 3. Cyclic voltammograms in sulfate-containing electrolytes with 200 mM Na⁺ and different SO₄²⁻ concentrations with a bulk pH of 3 at 2 mV s⁻¹ and a rotation rate of 2500 rpm under **a)** Ar and **b)** CO₂ atmosphere. Variation of **c)** the interfacial pH, **d)** the partial current density of CO₂RR, **e)** the partial current density of HER, **f)** the Faradaic efficiency of CO as a function of potential during the cyclic voltammetry from **b)**.

this higher mass transport limited effective proton reduction current also leads to higher interfacial pH, as deduced from the pH measurements on the ring (see Fig. S3) and disk (see Fig. 3c).

Once the CO₂RR starts, the proton reduction decays, due to, as mentioned above, CO₂RR generating hydroxide ions which consume the protons which would otherwise contribute to proton reduction. The results indicate that CO₂RR increases with the SO₄⁻ concentration. As shown in Figure 3, with the SO₄⁻ concentration raised from 30 mM to 200 mM, the current density of CO₂RR is enhanced by a factor of two, leading to the FE of CO increasing from 40% to 60%. The reason for this enhancing effect of the higher SO₄⁻ concentration on CO₂RR is not entirely clear. It likely has to do with the higher interfacial pH, which may also lead to a higher local concentration of cations., which then promotes CO₂RR.

The influence of another typical protic anion, namely H₂PO₄⁻, was also studied, by conducting the same experiments in 0.1M NaH₂PO₄ with a bulk pH of 4. Unlike the results in Na₂SO₄ and NaClO₄, no obvious mass transport limited region is detected (Figure 4a). This is attributed to the large proton flux brought by 0.1M H₂PO₄⁻, which can contribute more than 0.2 M protons during reactions. As Figure 4b illustrates, with the strong support from H₂PO₄⁻ (pK_a = 7.20), the total current density is remarkably larger than that in Na₂SO₄ and NaClO₄. This large current density is mainly due to the high promotion of HER by phosphate anions. The partial current density of HER in NaH₂PO₄ increases by two times compared to that in Na₂SO₄ and NaClO₄. Jackson et al⁵¹ also reported that the contribution to HER by direct phosphate reduction can outcompete water as the dominant proton source and enable HER activity at neutral pH comparable to that at pH 1. Consequently, the interfacial

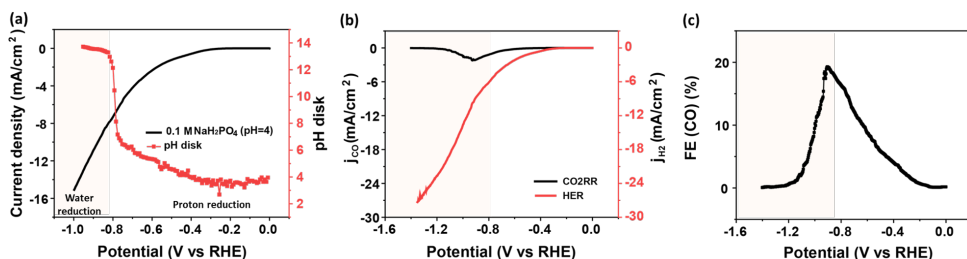


Figure 4. **a)** Variation of the interfacial pH recorded during cyclic voltammetry at 2 mV s⁻¹ and a rotation rate of 2500 rpm in 0.1 M CO₂-saturated NaH₂PO₄ with a bulk pH of 4: the black line and the red curve refer to the current density and to the corresponding interfacial pH during the negative-going scan, respectively. **b)** The partial current density of CO₂RR (black curve) and HER (red curve) during the cyclic voltammetry from a). **c)** The Faradaic efficiency of CO during the cyclic voltammetry

pH rises continuously with higher current density. There is 100 mM phosphate buffer species (H₂PO₄⁻: buffer range 6.2-8.2; HPO₄²⁻: buffer range: 11.3-13.3) in the bulk phase. Due to the buffering of H₂PO₄⁻, the interfacial pH increases slowly from 5 to 8 with increasing current density. Once depleting H₂PO₄⁻ near the interface, the pH increases dramatically and HPO₄²⁻ starts to buffer, resulting in a pH plateau at around 13. As the interfacial environment turns highly alkaline, CO₂RR is severely limited. The current density of CO₂RR declines at -0.9 V with a maximum FE of 20%. Hence, one should be very careful when involving buffer species in the electrolyte, because these protic buffer anions not only influence the interfacial pH, but are also highly likely to impact the proton-electron transfer to generate hydrogen at the interface.⁵²

The effect of cations in acidic media was investigated by measurements in sulfate electrolytes with different cations (pH=3). As shown in Figure 5a, results with different cations show a nearly identical proton reduction-dominant region, demonstrating that the proton reduction reaction is independent of cation identity, in agreement with the literature.²⁵ Additionally, there is no apparent disparity observed in mass transport limited regions with different cations, as the cations have no influence on the total proton flux. Therefore, the total current density of CO₂RR and proton reduction in the mass transport limited region is constant, independent of the identity of the cation. However, as the activity of CO₂RR varies with different cations, the proton reduction current in mass transport limiting region is affected indirectly. Figure 5c shows that the CO₂RR rate increases from Li⁺ to K⁺, demonstrating that weakly hydrated cations promote CO₂RR. Consequently, the activity of CO₂RR is highest in K₂SO₄, and the proton reduction is suppressed accordingly, leading to the largest FE of 70% in K⁺-containing electrolyte (Figure 5e). Interestingly, the FE in K⁺ decreases sharply once the water reduction sets in. This is because the higher concentration of weakly hydrated cations near the interface also contributes to a higher activity of water reduction, by stabilizing the transition state of its rate-determining step.⁵³ Consequently, the onset potential of water reduction shifts positively from Li⁺ to K⁺, resulting in a corresponding decay of the CO₂RR rate. Moreover, the interfacial pH in K⁺ is smaller than that in Na⁺ and Li⁺ in the mass transport limiting region (Figure 5b), even under the same current density. This can be explained by the theory of cation hydrolysis:³³ as the hydrated cation locates in proximity to the interface, its hydration shell interacts strongly with the negative charge on the electrode, causing a significant decrease in the pK_a of the cation (11.64 for Li⁺, 10.26 for Na⁺, 7.95 for K⁺) and facilitating the hydrolysis of the water molecule from the hydration shell to release protons.³³ Since the interfacial pH here is close to the pK_a of K⁺, protons are released from the hydration shell of K⁺ and decrease the interfacial pH.

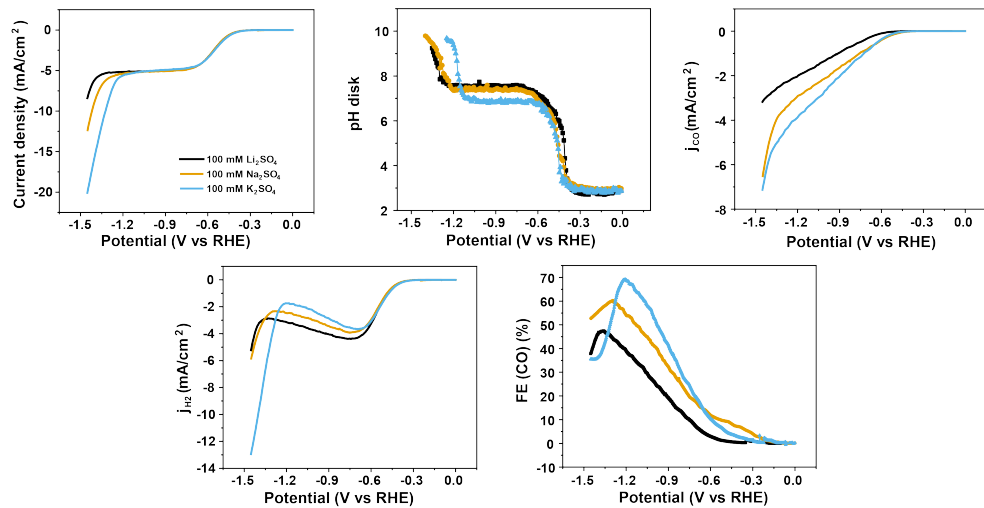


Figure 5. a) Cyclic voltammograms in CO_2 -saturated 100 mM sulfate with different cation identity with a bulk pH of 3 at 2 mV s^{-1} and a rotation rate of 2500 rpm. Variation of b) the interfacial pH, c) the partial current density of CO₂RR, d) the partial current density of HER, e) The Faradaic efficiency of CO as a function of potential during the cyclic voltammetry from a).

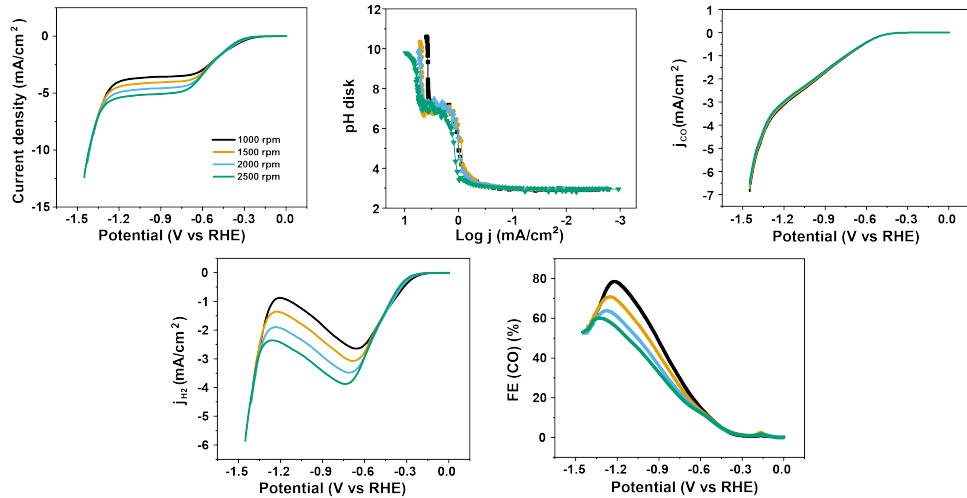


Figure 6. a) Cyclic voltammograms in CO_2 -saturated sulfate with 100 mM Na₂SO₄ with a bulk pH of 3 at 2 mV s^{-1} with different rotation rates of 2500 rpm. Variation of b) the interfacial pH, c) the partial current density of CO₂RR, d) the partial current density of HER, e) The Faradaic efficiency of CO as a function of potential during the cyclic voltammetry from a).

The effect of mass transport was studied by measurements in 0.1 M Na₂SO₄ (pH=3) under different disk rotation rates from 1000 rpm to 2500 rpm. As shown in Figure 6a, mass transport only affects the HER current: there is no effect on the CO₂RR current under these conditions. This observation is compelling evidence for the theory that protons are not directly involved in CO₂RR, but rather that CO₂RR is an OH⁻ generating reaction: at higher mass transfer rates, OH⁻ generated from CO₂RR can neutralize fewer incoming protons, leading to a lower FE. This effect is opposite to the mass transport effect in an alkaline environment: FE of CO₂RR in neutral or alkaline media increases with mass transport, mainly due to the competing water reduction being suppressed by decreasing interfacial pH.³⁶ The results in Figure 6 also illustrate that there is no CO₂-related mass transport effect on CO₂RR, as is often claimed in the literature. The observed mass transport effects are all indirectly related to the mass-transport sensitive HER.⁶

4.4 Conclusions

In this work, we have shown quantitatively using rotating ring-disk voltammetry how modulation of the interfacial reaction environment during CO₂RR in mildly acidic media (pH=3) on planar Au electrodes can generate situations that suppress most of HER, with a corresponding high Faradaic Efficiency (up to 80% under our conditions) and Carbon Efficiency.

Under acidic conditions, there are three ranges during the reaction process, namely the proton reduction dominant region, the proton mass transport limited region, and the water reduction dominant region. At mildly negative potential in acidic interfacial environment, the protons discharge on the surface. The interfacial reaction environment becomes less acidic with increasing current density. Prior to the depletion of protons, CO₂RR discernably increases, signifying the beginning of the second range. Although the total current density is still limited by the proton flux and the interfacial pH keeps constant accordingly, the partial current density of CO₂RR increases with increasingly negative potential, due to the protons being neutralized by the OH⁻ produced by CO₂RR. By the end of the mass transport limited regime, CO₂RR reaches the maximum in FE just before the water reduction initiates. From then on, OH⁻ is formed by water reduction and the interfacial environment quickly turns more alkaline. CO₂RR is inhibited as a result of the considerable depletion of CO₂ by the reaction with OH⁻.

The interfacial reaction environment can be tuned by anion identity, cation identity, and mass transport. A proper protic anion such as HSO₄⁻ can supply extra proton flux and tune the interfacial environment to be nearly neutral. . Besides, the influence of the cation effect and mass transport effect in an acidic interfacial environment is different from that in an

alkaline interfacial environment, since CO2RR competes with different HER branches. In an acidic environment, a weakly hydrated cation such as K^+ accelerates CO2RR while barely impacting the competing proton reduction, leading to a higher FE of CO2RR. But it decays drastically when reaching alkaline interfacial environment, as the competing water reduction is also promoted by a weakly hydrated cation. The FE of CO2RR decreases with enhanced mass transport in an acidic interfacial environment as the rate OH^- generation by CO2RR cannot keep up with the mass transfer rate of the protons. This mass transport effect is very different from the situation in an alkaline environment.³⁶

Our study sketches the interrelationship between different reactions and the interfacial environment and specifies the interrelationship between CO2RR and two major branches of HER, namely proton reduction and water reduction respectively. CO2RR is able to outcompete proton reduction under suitable conditions, while water reduction decreases the Faradaic and Carbon Efficiency of CO2RR.

From our work, we conclude that CO2RR is far from mass transport limited, even in our setup with strong forced convection. We expect that this conclusion may well be relevant for more practical systems and electrode geometries. The observed mass transport effects in our system are all related to the mass-transport sensitive HER, i.e. to pH gradients existing in the electrode boundary layer. Our work also stresses the importance of the interfacial environment, specifically for acid CO_2 electrolysis. Tuning the interfacial environment via an anion, cation and mass transport strategies remarkably impacts CO2RR, as it directly influences the interfacial concentration of CO_2 . Although we realize that the flat Au model surface used in this work is very different from a practical catalyst, we nevertheless believe that the insights gained from this model system can be applied to more practical geometries and can prove valuable for industrial applications. In fact, recent GDL studies in (weak) acid have already confirmed and implemented some of the findings such as the strategy of using concentrated weakly hydrated cations such as K^+ .²²⁻²³

References

- (1) Hori, Y.; Kikuchi, K.; Suzuki, S., Production of CO and CH4 in electrochemical reduction of CO_2 at metal electrodes in aqueous hydrogencarbonate solution. *Chem. lett.* 1985, 14 (11), 1695-1698.
- (2) Hori, Y.; Murata, A.; Takahashi, R., Formation of hydrocarbons in the electrochemical reduction of carbon dioxide at a copper electrode in aqueous solution. *J. Chem. Soc., Faraday Trans. 1* 1989, 85 (8), 2309-2326.
- (3) Ma, W. C.; He, X. Y.; Wang, W.; Xie, S. J.; Zhang, Q. H.; Wang, Y., Electrocatalytic reduction of CO_2 and CO to multi-carbon compounds over Cu-based catalysts. *Chem. Soc. Rev.* 2021, 50 (23), 12897-12914.

(4) Woldu, A. R.; Huang, Z. L.; Zhao, P. X.; Hu, L. S.; Astruc, D., Electrochemical CO₂ reduction (CO₂RR) to multi-carbon products over copper-based catalysts. *Coord. Chem. Rev.* 2022, **454**, 29.

(5) Jin, S.; Hao, Z. M.; Zhang, K.; Yan, Z. H.; Chen, J., Advances and Challenges for the Electrochemical Reduction of CO₂ to CO: From Fundamentals to Industrialization. *Angew. Chem., Int. Ed.* 2021, **60** (38), 20627-20648.

(6) Marcandalli, G.; Monteiro, M. C. O.; Goyal, A.; Koper, M. T. M., Electrolyte Effects on CO₂ Electrochemical Reduction to CO. *Acc. Chem. Res.* 2022, **55** (14), 1900-1911.

(7) Zhu, Y. T.; Cui, X. Y.; Liu, H. L.; Guo, Z. G.; Dang, Y. F.; Fan, Z. X.; Zhang, Z. C.; Hu, W. P., Tandem catalysis in electrochemical CO₂ reduction reaction. *Nano Res.* 2021, **14** (12), 4471-4486.

(8) Dunwell, M.; Lu, Q.; Heyes, J. M.; Rosen, J.; Chen, J. G.; Yan, Y.; Jiao, F.; Xu, B., The Central Role of Bicarbonate in the Electrochemical Reduction of Carbon Dioxide on Gold. *J. Am. Chem. Soc.* 2017, **139** (10), 3774-3783.

(9) Hori, Y. i., Electrochemical CO₂ reduction on metal electrodes. *Modern aspects of electrochemistry* 2008, 89-189.

(10) Wuttig, A.; Yoon, Y.; Ryu, J.; Surendranath, Y., Bicarbonate Is Not a General Acid in Au-Catalyzed CO₂ Electroreduction. *J. Am. Chem. Soc.* 2017, **139** (47), 17109-17113.

(11) Marcandalli, G.; Goyal, A.; Koper, M. T. M., Electrolyte Effects on the Faradaic Efficiency of CO₂ Reduction to CO on a Gold Electrode. *ACS Catal.* 2021, **11** (9), 4936-4945.

(12) Rabinowitz, J. A.; Kanan, M. W., The future of low-temperature carbon dioxide electrolysis depends on solving one basic problem. *Nat. Commun.* 2020, **11** (1), 5231.

(13) Bondue, C. J.; Graf, M.; Goyal, A.; Koper, M. T. M., Suppression of Hydrogen Evolution in Acidic Electrolytes by Electrochemical CO₂ Reduction. *J. Am. Chem. Soc.* 2020, **143** (1), 279-285.

(14) Huang, J. E.; Li, F.; Ozden, A.; Sedighian Rasouli, A.; García de Arquer, F. P.; Liu, S.; Zhang, S.; Luo, M.; Wang, X.; Lum, Y.; Xu, Y.; Bertens, K.; Miao, R. K.; Dinh, C.-T.; Sinton, D.; Sargent, E. H., CO₂ electrolysis to mult carbon products in strong acid. *Science* 2021, **372** (6546), 1074-1078.

(15) Ørkopp, M.; Löwe, A.; Lobo, C. M. S.; Baranyai, S.; Khoza, T.; Auinger, M.; Klemm, E., Producing formic acid at low pH values by electrochemical CO₂ reduction. *J. CO₂ Util.* 2022, **56**, 101823.

(16) Liu, Z.; Yan, T.; Shi, H.; Pan, H.; Cheng, Y.; Kang, P., Acidic Electrocatalytic CO₂ Reduction Using Space-Confining Nanoreactors. *ACS Appl. Mater. Interfaces* 2022, **14** (6), 7900-7908.

(17) Ma, Z.; Yang, Z.; Lai, W.; Wang, Q.; Qiao, Y.; Tao, H.; Lian, C.; Liu, M.; Ma, C.; Pan, A.; Huang, H., CO₂ electroreduction to mult carbon products in strongly acidic electrolyte via synergistically modulating the local microenvironment. *Nat. Commun.* 2022, **13** (1), 7596.

(18) Sheng, X.; Ge, W.; Jiang, H.; Li, C., Engineering the Ni-N-C Catalyst Microenvironment Enabling CO₂ Electroreduction with Nearly 100% CO Selectivity in Acid. *Adv. Mater.* 2022, **34** (38), 2201295.

(19) Xie, Y.; Ou, P.; Wang, X.; Xu, Z.; Li, Y. C.; Wang, Z.; Huang, J. E.; Wicks, J.; McCallum, C.; Wang, N.; Wang, Y.; Chen, T.; Lo, B. T. W.; Sinton, D.; Yu, J. C.; Wang, Y.; Sargent, E. H., High carbon utilization in

CO₂ reduction to multi-carbon products in acidic media. *Nat. Catal.* 2022, 5 (6), 564-570.

(20) Fan, Q.; Bao, G.; Chen, X.; Meng, Y.; Zhang, S.; Ma, X., Iron Nanoparticles Tuned to Catalyze CO₂ Electrocatalysis in Acidic Solutions through Chemical Microenvironment Engineering. *ACS Catal.* 2022, 12 (13), 7517-7523.

(21) Nie, W.; Heim, G. P.; Watkins, N. B.; Agapie, T.; Peters, J. C., Organic Additive-derived Films on Cu Electrodes Promote Electrochemical CO₂ Reduction to C₂+ Products Under Strongly Acidic Conditions. *Angew. Chem., Int. Ed.* 2023, 135 (12), e202216102.

(22) Monteiro, M. C. O.; Philips, M. F.; Schouten, K. J. P.; Koper, M. T. M., Efficiency and selectivity of CO(2) reduction to CO on gold gas diffusion electrodes in acidic media. *Nat. Commun.* 2021, 12 (1), 4943.

(23) Gu, J.; Liu, S.; Ni, W.; Ren, W.; Haussener, S.; Hu, X., Modulating electric field distribution by alkali cations for CO₂ electroreduction in strongly acidic medium. *Nat. Catal.* 2022, 5 (4), 268-276.

(24) Qin, H.-G.; Li, F.-Z.; Du, Y.-F.; Yang, L.-F.; Wang, H.; Bai, Y.-Y.; Lin, M.; Gu, J., Quantitative Understanding of Cation Effects on the Electrochemical Reduction of CO₂ and H⁺ in Acidic Solution. *ACS Catal.* 2022, 13 (2), 916-926.

(25) Monteiro, M. C. O.; Dattila, F.; López, N.; Koper, M. T. M., The Role of Cation Acidity on the Competition between Hydrogen Evolution and CO₂ Reduction on Gold Electrodes. *J. Am. Chem. Soc.* 2021, 144 (4), 1589-1602.

(26) Pan, H.; Barile, C. J., Electrochemical CO₂ Reduction on Polycrystalline Copper by Modulating Proton Transfer with Fluoropolymer Composites. *ACS Appl. Energy Mater.* 2022, 5 (4), 4712-4721.

(27) Zhou, X.; Liu, H.; Xia, B. Y.; Ostrikov, K.; Zheng, Y.; Qiao, S. Z., Customizing the microenvironment of CO₂ electrocatalysis via three-phase interface engineering. *SmartMat* 2022, 3 (1), 111-129.

(28) König, M.; Vaes, J.; Klemm, E.; Pant, D., Solvents and Supporting Electrolytes in the Electrocatalytic Reduction of CO₂. *iScience* 2019, 19, 135-160.

(29) Xu, A.; Govindarajan, N.; Kastlunger, G.; Vijay, S.; Chan, K., Theories for Electrolyte Effects in CO₂ Electrocatalysis. *Acc. Chem. Res.* 2022, 55 (4), 495-503.

(30) Monteiro, M. C. O.; Dattila, F.; Hagedoorn, B.; García-Muelas, R.; López, N.; Koper, M. T. M., Absence of CO₂ electroreduction on copper, gold and silver electrodes without metal cations in solution. *Nat. Catal.* 2021, 4 (8), 654-662.

(31) Pan, B.; Wang, Y.; Li, Y., Understanding and leveraging the effect of cations in the electrical double layer for electrochemical CO₂ reduction. *Chem Catal.* 2022, 2 (6), 1267-1276.

(32) Resasco, J.; Chen, L. D.; Clark, E.; Tsai, C.; Hahn, C.; Jaramillo, T. F.; Chan, K.; Bell, A. T., Promoter Effects of Alkali Metal Cations on the Electrochemical Reduction of Carbon Dioxide. *J. Am. Chem. Soc.* 2017, 139 (32), 11277-11287.

(33) Singh, M. R.; Kwon, Y.; Lum, Y.; Ager, J. W., 3rd; Bell, A. T., Hydrolysis of Electrolyte Cations Enhances the Electrochemical Reduction of CO₂ over Ag and Cu. *J. Am. Chem. Soc.* 2016, 138 (39), 77

13006-13012.

(34) Liu, X.; Monteiro, M. C. O.; Koper, M. T. M., Interfacial pH measurements during CO(2) reduction on gold using a rotating ring-disk electrode. *Phys. Chem. Chem. Phys.* 2023, 25 (4), 2897-2906.

(35) Ayemoba, O.; Cuesta, A., Spectroscopic Evidence of Size-Dependent Buffering of Interfacial pH by Cation Hydrolysis during CO₂ Electroreduction. *ACS Appl. Mater. Interfaces* 2017, 9 (33), 27377-27382.

(36) Goyal, A.; Marcandalli, G.; Mints, V. A.; Koper, M. T. M., Competition between CO₂ Reduction and Hydrogen Evolution on a Gold Electrode under Well-Defined Mass Transport Conditions. *J. Am. Chem. Soc.* 2020, 142 (9), 4154-4161.

(37) Monteiro, M. C. O.; Liu, X.; Hagedoorn, B. J. L.; Snabilié, D. D.; Koper, M. T. M., Interfacial pH Measurements Using a Rotating Ring-Disc Electrode with a Voltammetric pH Sensor. *ChemElectroChem* 2021, 9 (1), e202101223.

(38) Vos, R. E.; Koper, M. T. M., The Effect of Temperature on the Cation-Promoted Electrochemical CO₂ Reduction on Gold. *ChemElectroChem* 2022, 9 (13), e202200239.

(39) Blizanac, B. B.; Arenz, M.; Ross, P. N.; Marković, N. M., Surface Electrochemistry of CO on Reconstructed Gold Single Crystal Surfaces Studied by Infrared Reflection Absorption Spectroscopy and Rotating Disk Electrode. *J. Am. Chem. Soc.* 2004, 126 (32), 10130-10141.

(40) Yang, K.; Kas, R.; Smith, W. A., In Situ Infrared Spectroscopy Reveals Persistent Alkalinity near Electrode Surfaces during CO₂ Electroreduction. *J. Am. Chem. Soc.* 2019, 141 (40), 15891-15900.

(41) Schulz, K. G.; Riebesell, U.; Rost, B.; Thoms, S.; Zeebe, R. E., Determination of the rate constants for the carbon dioxide to bicarbonate inter-conversion in pH-buffered seawater systems. *Mar. Chem.* 2006, 100 (1-2), 53-65.

(42) Deng, G.-H.; Zhu, Q.; Rebstock, J.; Neves-Garcia, T.; Baker, L. R., Direct observation of bicarbonate and water reduction on gold: understanding the potential dependent proton source during hydrogen evolution. *Chem. Sci.* 2023, 14 (17), 4523-4531.

(43) Marcandalli, G.; Monteiro, M. C. O.; Koper, M. T. M., Electrolyte buffering species as oxygen donor shuttles in CO electrooxidation. *Phys. Chem. Chem. Phys.* 2022, 24 (4), 2022-2031.

(44) Albery, W. J.; Calvo, E. J., Ring-disc electrodes. Part 21.—pH measurement with the ring. *J. Chem. Soc., Faraday Trans. 1* 1983, 79 (11), 2583-2596.

(45) Gálvez-Vázquez, M. d. J.; Grozovski, V.; Kovács, N.; Broekmann, P.; Vesztergom, S., Full Model for the Two-Step Polarization Curves of Hydrogen Evolution, Measured on RDEs in Dilute Acid Solutions. *J. Phys. Chem. C* 2020, 124 (7), 3988-4000.

(46) Mukouyama, Y.; Nakanishi, S., An Ordinary Differential Equation Model for Simulating Local-pH Change at Electrochemical Interfaces. *Front. Energy Res.* 2020, 8.

(47) Monteiro, M. C. O.; Jacobse, L.; Koper, M. T. M., Understanding the Voltammetry of Bulk CO Electrooxidation in Neutral Media through Combined SECM Measurements. *J. Phys. Chem. Lett.* 2020, 11 (22), 9708-9713.

(48) Cuesta, A.; Kleinert, M.; Kolb, D. M., The adsorption of sulfate and phosphate on Au(111) and Au(100) electrodes: an in situ STM study. *Phys. Chem. Chem. Phys.* 2000, 2 (24), 5684-5690.

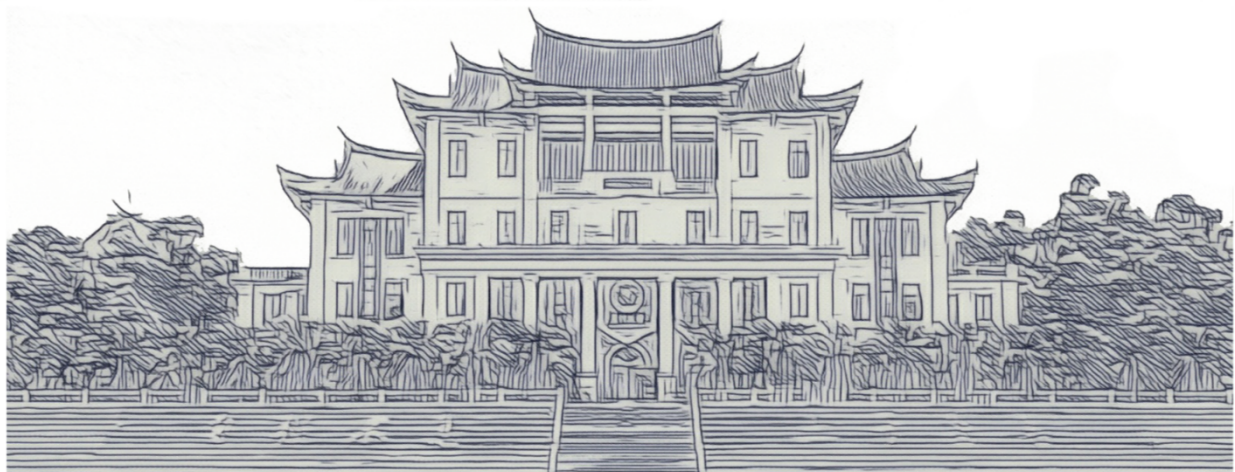
(49) Koutecky, J.; Levich, V., The use of a rotating disk electrode in the studies of electrochemical kinetics and electrolytic processes. *Zh. Fiz. Khim.* 1958, 32, 1565-1575.

(50) Rebouillat, S.; Lyons, M. E. G.; Bannon, T., Evaluation of the proton transfer kinetics of potential electrolytes in non-aqueous solutions using electrochemical techniques Part 1. Kinetic analysis of the general CE mechanism at stationary and rotating electrodes. *J. Solid State Electrochem.* 1999, 3 (4), 215-230.

(51) Jackson, M. N.; Jung, O.; Lamotte, H. C.; Surendranath, Y., Donor-Dependent Promotion of Interfacial Proton-Coupled Electron Transfer in Aqueous Electrocatalysis. *ACS Catal.* 2019, 9 (4), 3737-3743.

(52) Marcandalli, G.; Boterman, K.; Koper, M. T. M., Understanding hydrogen evolution reaction in bicarbonate buffer. *J. Catal.* 2022, 405, 346-354.

(53) Goyal, A.; Koper, M. T. M., The Interrelated Effect of Cations and Electrolyte pH on the Hydrogen Evolution Reaction on Gold Electrodes in Alkaline Media. *Angew. Chem., Int. Ed.* 2021, 60 (24), 13452-13462.



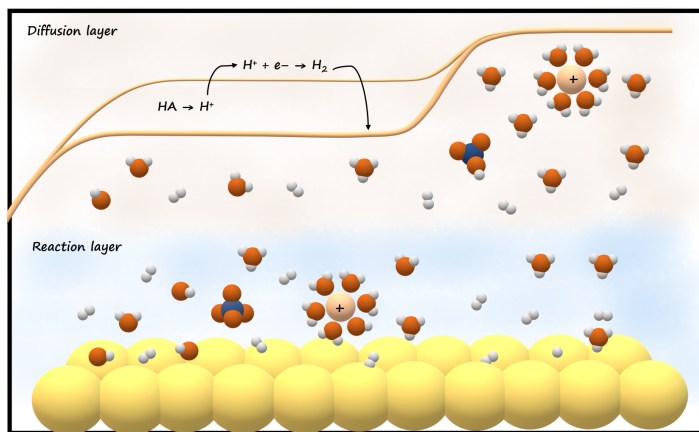
Chapter 5

The Effect of Weak Proton Donors on the Steady-State Behaviour of Hydrogen Evolution in Mildly Acidic Media



Abstract

The vital importance of anionic and cationic electro-inactive species in the Hydrogen Evolution Reaction (HER) is increasingly noted. However, their influence on the steady-state current of HER is potentially underestimated. Here, the effects of these widely-used electrolyte species on the steady-state behavior of HER are investigated on a Au RDE at a bulk pH of 4. A current enhancement is observed from the coupling of proton reduction with homogeneous acid-base equilibria, with HSO_4^- having the largest influence despite the electrolyte condition being far beyond its typical buffering range, while the cations, specifically K^+ and Cs^+ , serve as weak buffers with limited buffer capacity. Further quantitative analysis illustrates that from the steady-state current of HER the thermodynamic parameters of the homogeneous reactions can be evaluated, taking advantage of the linear dependence of the Koutecký-Levich Slope on the concentration of the electro-inactive species. Based on this evaluation, the pK_a 's of HSO_4^- , K^+ and Cs^+ were determined to be 2.06, 2.52 and 2.48, respectively. These results confirm the previously postulated proton-donating capability of certain (alkali) cations and show that these effects influence the HER current in mildly acidic media.



This chapter is based on Liu, X.; Koper, M. T. M., The Effect of Weak Proton Donors on the Steady-State Behavior of Hydrogen Evolution in Mildly Acidic Media (submitted).

5.1 Introduction

Hydrogen is one of the most promising alternatives to fossil fuels in the pursuit of a clean and sustainable society. The Hydrogen Evolution Reaction (HER) coupled with renewable electricity, producing hydrogen from the aqueous solutions with net zero greenhouse gas emissions, is considered as the most viable avenue towards a green hydrogen future.¹⁻² Furthermore, HER often competes and interacts with other electrochemical processes e.g. CO₂ electroreduction,³⁻⁴ and metal electrodeposition.⁵⁻⁶ High HER rates heavily impact the interfacial electrolyte properties, especially local pH and other local ion concentrations.⁷⁻⁸ To control the interference from mass transport and suppress the influence of gas bubble formation, HER studies are commonly performed using a Rotating Disk Electrode (RDE). Several studies have been dedicated to interpreting the HER behavior in different electrolyte conditions.⁹⁻¹¹ It is well-established that a typical HER process in acidic media consists of a proton reduction regime, and a proton mass transport-limited plateau followed by a water reduction regime at more negative potentials. In the first regime, the hydronium cation is the prevailing proton source, while the water molecule provides the protons in the water reduction regime (Eqs. 1-2):¹²



The proton reduction current is expected to be first order in proton concentration, while water reduction current has a complicated dependence on local pH, local cation concentration, and mass transport.¹³ The limiting current density due to proton reduction can be calculated according to the Levich Equation (Eq. 3):¹⁴⁻¹⁵

$$i_l = 0.62nFAD_H^{2/3}\omega^{1/2}\nu^{-1/6}C_H \quad (3)$$

where n is the electron transfer number per proton (1 for HER here), F is the Faraday constant, D_H is the diffusion coefficient of the proton (cm² s⁻¹), ω is the angular rotation rate (rad s⁻¹), ν is the kinematic viscosity (cm² s⁻¹), C_H is the bulk concentration of the proton. This equation is often used to obtain the diffusion coefficient of the reactive species (in this case proton) in the electrolyte under study.

Importantly, special care must be taken to ascertain the applicability of the Levich equation under particular circumstances. The assumptions involved in the derivation of the Levich equation impose limitations on its applicability to those reactions with a low concentration of supporting electrolyte and those coupled with homogeneous reactions.¹⁶⁻¹⁷ Specifically, so-called electro-inactive species, which do not participate directly in the heterogeneous electron-transfer reaction, can play an important role in the steady-state current of HER. The first role is *via* electromigration, when the concentration of supporting electrolyte is not appreciably larger than the bulk proton concentration. Such a situation gives rise to a

migration contribution to mass transport.¹⁸⁻¹⁹ As reported by Osteryoung et al,²⁰⁻²¹ the steady-state current density without supporting electrolyte is two times larger than that with excess supporting electrolyte. Amatore et al¹⁸ also addressed this effect with an analytical model to quantify the migration effects on the steady-state current density.

Of interest in this work is a second effect by which electro-inactive species may modify the steady-state behavior of HER, namely through a preceding chemical reaction, specifically an acid-base reaction, which alters the reactive flux by generating protons. Such a mechanism is referred to as a CE process (Eqs. 4-5):²²⁻²³



By postulating that the reaction layer (in which the chemical reaction C is disturbed by the interfacial E step) is thinner than the diffusion layer, Koutecký and Levich could deconvolute the chemical reaction from the mass transport. The equation for the steady-state current of the CE process is obtained by assuming that all species have equal diffusion coefficients (i_{KL} , Eq. 6),²⁴

$$i_{KL} = \frac{FD(c_{\text{HA}}^b + c_{\text{H}}^b)}{\delta_D + K \sqrt{\frac{D}{k_f + k_b}}} \quad (6)$$

where D denotes the diffusion coefficient of the proton and the proton donors, δ_D signifies the thickness of the diffusion layer, c_X^b is the bulk concentration of X species, K is the equilibrium constant of Eq. 4, and k_f and k_b are the rate constants of the forward and backward reaction of Eq. 4. Later, Dogonadze²⁵ extended this equation to the case of unequal diffusion coefficients (i_{DG} , Eq. 7).

$$i_{DG} = \frac{F \frac{D_H k_f + D_{\text{HA}} k_b}{k_f + k_b} (c_{\text{HA}}^b + c_{\text{H}}^b)}{\delta_D \sqrt[3]{\frac{D_H k_f + D_{\text{HA}} k_b}{D_{\text{HA}}(k_f + k_b)} + K \frac{D_H}{D_{\text{HA}}} \sqrt{\frac{D_{\text{HA}} D_H}{D_H k_f + D_{\text{HA}} k_b}}} \quad (7)$$

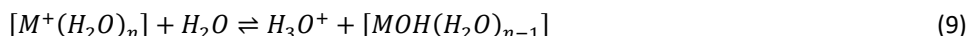
There are also numerical studies to simulate the steady-state behavior of the CE process on RDEs²⁶⁻²⁷. Rebouillat et al²² developed a mathematical simplification of the original Koutecký-Levich equation (Eq. 6) for different rate-limiting scenarios, dependent on the competition between the chemical reaction kinetics and diffusion. Specifically, when the reaction rate is still controlled by diffusion but modified by the preceding homogeneous process, the steady-state current is evaluated through Eq. 8,

$$\frac{1}{i} = \frac{\omega^{-1/2}}{0.62nFAD_{\text{HA}}^{2/3}v^{-1/6}KC_{\Sigma}} \quad (8)$$

where C_{Σ} is the total concentration of the proton donors. These equations have been used to study the kinetics and thermodynamics of the HER-coupled dissociation of weak acids,
85

e.g. acetic acid,²⁸ and citric acid.²⁹

Apart from these aforementioned typical acids, any conjugated acid that is capable of deprotonation in an aqueous solution may function as a potential proton donor for HER, including buffering anions and cations commonly used as supporting electrolytes.³⁰⁻³² Dating back to 1960, Cosijn³³ observed that the mono/di-hydrogen phosphate anions enhance the HER current leading to the appearance of extra current density plateaus in the polarization curves. Jackson et al.³⁴ also reported that phosphate can outcompete water as the primary proton source and enable HER activity at a neutral pH comparable to that at pH 1. Besides, the findings of Moreno-García et al.³⁵ and our previous work³⁶ have validated bisulfate as a proton donor. More recently, alkali metal cations in the vicinity of a negative-polarized electrode have also been suggested to be weak buffers (Eq. 9),



with a buffering capability decreasing in the order $Cs^+ > Rb^+ > K^+ > Na^+ > Li^+$. A computational study by Singh et al.³⁷ indicated that the interaction between the negative charge on the electrode and the alkali cations facilitates the hydrolysis of the water molecules from the cation's hydration shell, thereby decreasing the pK_a of the cations. In-situ pH measurements also confirmed the decrease of local pH due to the presence of weakly hydrated cations such as K^+ and Cs^+ .³⁸⁻⁴⁰

A comprehensive understanding of the interfacial reaction processes includes probing the vital roles that the electro-inactive species play in heterogeneous charge transfer reactions.⁴¹⁻⁴² In this work, we studied the HER performance in different electrolyte conditions on a Au-RDE in order to distinguish the effects of the aforementioned (weak) proton donors, namely the bisulfate anion and the alkali cations, on the HER behavior. To highlight exclusively the implicit influence of these species, the bulk pH was meticulously maintained at 4 to suppress the impact from the bulk protons. The total electrolyte concentration was controlled to suppress any interference from electromigration. We show that HER is still under mass transport control but modified by the homogenous reaction process. Importantly, the current enhancement contributed by the protons generated from the dissociation of the protic anion (HSO_4^-) and the hydrolysis of alkali cations near the electrode interface can be quantified and the corresponding equilibrium constant K can be evaluated.

5.2 Experimental section

Materials and Chemicals. Ultrapure water ($>18.2 \text{ M}\Omega \text{ cm}$, Millipore Milli-Q) and the following chemicals were used to prepare electrolytes involved in the measurements: $LiClO_4$ ($>99.99\%$, trace metal basis, Sigma-Aldrich), $NaClO_4$ ($>99.99\%$, trace metal basis, Sigma-

Aldrich), KClO_4 (>99.99%, trace metal basis, Sigma-Aldrich), Li_2SO_4 (>99.99%, trace metal basis, Sigma-Aldrich), Na_2SO_4 (99.99% Suprapur, Sigma-Aldrich), K_2SO_4 (>99.99%, Suprapur, Sigma-Aldrich), and H_2SO_4 (96% Suprapur, Merck). The pH of the electrolytes was adjusted by H_2SO_4 (96% Suprapur, Merck) and HClO_4 (70% Suprapur, Merck) and measured by a glass-electrode pH meter (Lab 855, SI Analytics) calibrated with standard buffer solutions (Radiometer Analytical), then deaerated by a Ar purge (6.0 purity, Linde, 20 min) prior to experiments. All the electrochemical experiments were carried out in homemade single-compartment electrochemical cells controlled by a 4-channel Biologic potentiostat (VSP-300) and a Modulated Speed Rotator (Pine Research). A three-electrode system was utilized in all the electrochemical measurements, involving a RDE tip (E5TQ ChangeDisk, PEEK Shroud, Pine Research) as the working electrode, a Au wire (0.5 mm diameter, MaTeck, 99.9%) as a counter electrode and a Ag/AgCl electrode (RE-1B, 3 M NaCl , Biologic, connected to the main chamber through a Luggin capillary) as a reference electrode.

Preparation. Prior to measurements, electrolytes were prepared freshly employing certain amounts of aforementioned chemicals. To meticulously control the bulk pH, the electrolytes were prepared by adding a certain amount of 0.1 M proton-donor electrolyte (bulk pH 4.0) to a certain amount 0.1 M supporting electrolyte (bulk pH 4.0). For example, the serial measurements in $\text{LiClO}_4 + \text{KClO}_4$ started from 0.1 M LiClO_4 (bulk pH 4.0), then 5 mL 0.1 M KClO_4 (bulk pH 4.0) was added to 95 mL of the previous electrolyte (i.e. 0.1 M LiClO_4) for the second measurement, and the bulk pH was remeasured by the pH meter and adjusted if any deviation from 4.0 occurred. Next, 10 mL 0.1 M KClO_4 (bulk pH 4.0) was added to 90 mL of the previous electrolyte (i.e. 5 mM LiClO_4 + 95 mM KClO_4) for the third measurement. Detailed compositions and the corresponding bulk pH of the electrolytes are given in the Supporting Information. The electrochemical cells and other glassware were stored in acidified KMnO_4 solution (1 g L^{-1} KMnO_4 in 0.5 M H_2SO_4) overnight and then immersed in dilute piranha to remove the generated MnO_x and the residual KMnO_4 , followed rinsing and boiling in ultrapure water for five times. The RDE tip was polished with the 3 μm , 1 μm , 0.25 μm diamond suspension (MetaDi, Buehler) respectively, with the Au disk ($r = 5\text{mm}$) embedded in the PEEK shroud and sonicated in ethanol and ultrapure water for 5 min in between each step.

Electrochemical measurements. Prior to measurements, the Au RDE tip was electropolished in 0.1 M H_2SO_4 (Ar-saturated) by cycling between 0 and 1.75 V vs RHE at 500 mV s^{-1} for 200 times, followed by a characterizing cyclic voltammogram under the same conditions at 100 mV s^{-1} on Au, to examine the surface and calculate the electrochemical surface area (ECSA) by dividing the charge of the Au oxide reduction peak with the charge density of a Au oxide monolayer ($386 \mu\text{C cm}^{-2}$). The Ar flow was kept purging into the

electrolyte during the measurements to avoid any interference from oxygen. The solution resistance was determined by electrochemical impedance spectroscopy (EIS) and the electrode potential was compensated for 85% of the ohmic drop. Details of quantitative analysis are explained in the Supporting Information.

5.3 Results and discussion

The HER performance in sulfate solutions was investigated on a Au RDE with a bulk pH of 4.0. As illustrated in Figure 1, the polarization curves show two characteristic exponential regimes separated by a plateau. At low overpotential, the current is controlled (kinetically) by proton reduction. As the protons near the interface deplete with increasing polarization, the reaction rate becomes controlled by mass transport, leading to the plateau current. In the simplest case, the value of the limiting current density is proportional to the bulk proton concentration, i.e. an exclusive function of bulk pH. However, the steady-state behavior of HER in Fig.1 perceptibly varies with the cation identity and the electrolyte concentration despite the fact that the bulk pH is the same. This effect cannot be attributed to an electromigration effect as a higher ionic strength would suppress proton migration and lead to a lower current, whereas we observe the opposite. To test whether acid-base equilibria may be involved, similar measurements were carried out in perchlorate solutions. Figure 2 depicts vastly different results compared to sulfate solutions. The (limiting) current density does not depend on the electrolyte concentration in LiClO_4 and NaClO_4 . Figure 2a-b show that, although Li^+ and Na^+ do not affect proton reduction, they promote water reduction. Previous studies have shown that alkali cations aid in water reduction *via* stabilization of the reaction intermediate.⁴³ Therefore, for the results in Fig.1, the sulfate anion must be responsible for the observed increase in limiting current density with higher electrolyte concentration of Li_2SO_4 and Na_2SO_4 , which is in agreement with the results from our previous study at a bulk pH of 3.³⁶ The coupling of the proton reduction and the dissociation of HSO_4^- results in a concentration-dependent behavior of HER in sulfate-containing electrolyte.

Compared with Figure 2a-b, the concentration of KClO_4 in Figure 2c is restricted up to 100 mM, due to the solubility limitations of KClO_4 . Importantly, an evident increase in the limiting current density is observed as the concentration rises from 50 mM to 100 mM, which suggests that K^+ acts as a promotor for the HER current. This amplification may be evidence for a low pK_a and the resultant hydrolysis of the alkali cations in the proximity of the electrode, as has been proposed by Singh et al³⁷ in a computational study. This is attributed to the interaction between the cation and the negatively charged electrode facilitating the hydrolysis of the water molecule from the hydration shell of the cation. The

pK_a of the cation appreciably decreases and protons are released from the cation hydration shell and contribute to the current density. Of course, the buffer capacity of the alkali cations is not as remarkable as that of the commonly-used buffer species as e.g. HCO_3^- , $\text{H}_2\text{PO}_4^{3-}$.³⁶ The hydrolysis effect of the alkali cations is easily overwhelmed by the current density from proton reduction in acidic media. It is of importance to perform the measurements in the least acidic media possible in order to facilitate the observation of the influence of cation hydrolysis, while also ensuring that the change in the limiting current density is detectable. Accordingly, the observed enhancement in Figure 1a-b is attributed to the deprotonation of HSO_4^- while in Figure 1c is due to the combined effect of the deprotonation of HSO_4^- and the hydrolysis of K^+ , which explains the larger enhancement in

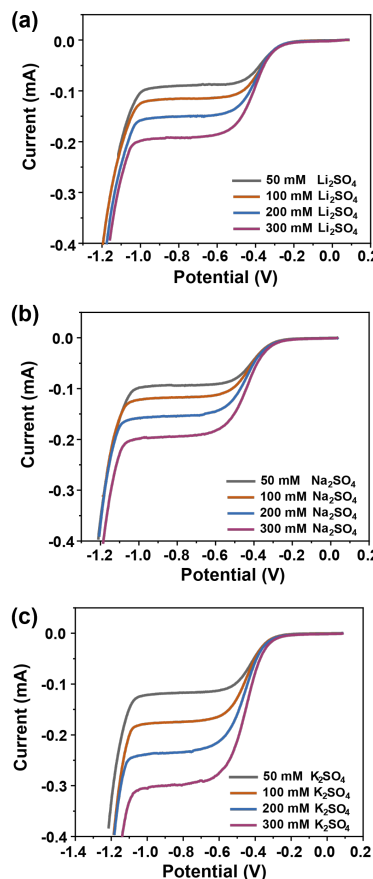


Figure 1. Polarization curves recorded on a Au RDE in Ar-saturated sulfate electrolytes with different cation identity and electrolyte concentration with a bulk pH of 4 at 10 mV s^{-1} and a rotation rate of 2500 rpm.

Figure 1c.

To gain further insights into the effect of these potential proton donors in the electrolyte on the steady-state behavior of HER, additional experiments were conducted in a series of perchlorate electrolytes with progressively higher SO_4^{2-} contents. LiClO_4 was employed as a supporting electrolyte, since neither Li nor ClO_4^- impacts the HER behavior under these conditions, as shown in Fig. 2. The total anion concentration was kept constant. As depicted in Figure 3a, the limiting current density observed increases by a factor of two relative to the pure LiClO_4 electrolyte, as a result of a larger proton flux provided by the HSO_4^- dissociation. The linear relationships between the inverse current density and the inverse

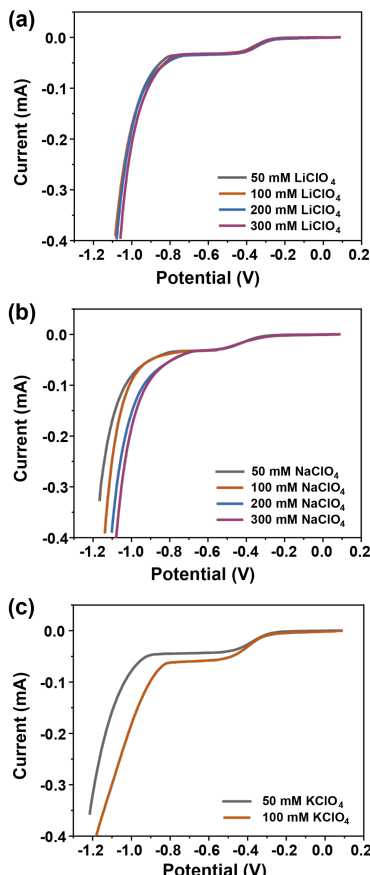


Figure 2. Polarization curves recorded on a Au RDE in Ar-saturated perchlorate electrolytes with different cation identity and electrolyte concentration with a bulk pH of 4 at 10 mV s^{-1} and a rotation rate of 2500 rpm.

of the square root of the disk rotation rate ($\omega^{-1/2}$) shown in Figure 3b confirms that the HER rate is still controlled by diffusion, albeit impacted by the HSO_4^- dissociation process. However, this diffusion control is modified by the chemical reaction as evidenced by the Koutecký- Levich slope (referred to as " S_{K-L} ") being linearly dependent on the SO_4^{2-} concentration (Fig.3c), as expressed in Eq. 10:

$$S_{K-L}^{-1} = 0.13 [\text{SO}_4^{2-}]_{\Sigma} + 7.46 \times 10^{-6} \quad (10)$$

According to the equation proposed by Rebouillat et al. (see Eq.8 in the Introduction),²² the equilibrium constant K can be obtained from this slope. However, since the concentration of the weak acid is assumed to be much greater than that of the proton concentration in the original analysis by Rebouillat, the current contribution from the bulk protons is neglected in the model, which is not the case in our scenario. As there is a non-zero bulk concentration of protons, the total current must be given by the sum of the direct proton reduction and the “indirect” proton reduction generated by the CE mechanism as displayed in Eqs. 11-12:

$$\frac{1}{i} = \frac{\omega^{-1/2}}{0.62nFAD_{HA}^{2/3}v^{-1/6}KC_{\Sigma} + 0.62nFAD_H^{2/3}v^{-1/6}C_H} \quad (11)$$

$$S_{K-L}^{-1} = 0.62nFAD_{HA}^{2/3}v^{-1/6}KC_{\Sigma} + 0.62nFAD_H^{2/3}v^{-1/6}C_H \quad (12)$$

where n is the electron transfer number per proton (1 for HER here), F is the Faraday constant, D_{HA} is the diffusion coefficient of the proton donor ($\text{cm}^2 \text{ s}^{-1}$), ω is the angular rotation rate (rad s^{-1}), v is the kinematic viscosity ($\text{cm}^2 \text{ s}^{-1}$). Based on the linear correlation between S_{K-L}^{-1} and SO_4^{2-} concentration, the pK_a of HSO_4^- is evaluated to be 2.06, in close agreement with the reported pK_a of HSO_4^- (1.99).⁴⁴ Calculation details can be found in the Supporting Information.

To validate the evaluation and the effect of the cation hydrolysis, a similar analysis was performed with different cations. Experiments were conducted in a series of electrolytes with LiClO_4 as the supporting electrolyte and increasing concentration of other alkali cations. The dependence of the steady-state behavior of HER on Na^+ concentration was examined first. However, in alignment with the results above, a barely appreciable change in the limiting current density with increasing Na^+ concentration was found (see Figure S8 in the supporting information), meaning that hydrated Na^+ is an ineffective proton donor. By comparison, Figure 4a illustrates a gradual enhancement of the limiting current density of HER with the increasing K^+ concentration, suggesting that hydrated K^+ can act as a proton donor due to hydrolysis. However, the enhancement by K^+ is limited compared with HSO_4^- , due to a larger proton-donating capacity of HSO_4^- than alkali cations, which is also expressed by the fact that the S_{K-L}^{-1} of HSO_4^- is over two times larger than that of K^+ . Quantitative analysis from the slope shown in Figure 4c gives a pK_a of K^+ of 2.52. This cation hydrolysis is

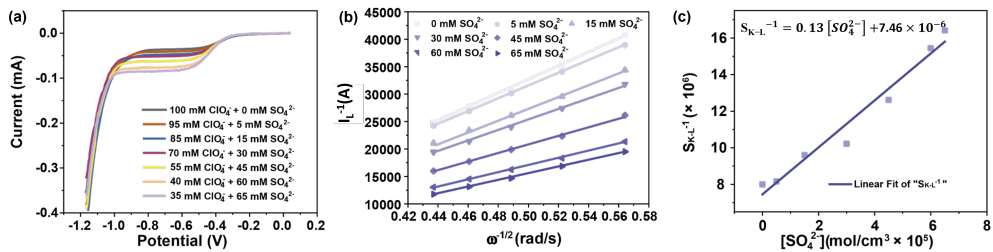


Figure 3. a) Polarization curves recorded on a Au RDE in Ar-saturated lithium electrolytes with a different ratio of the anion with a bulk pH of 4 at 10 mV s^{-1} and a rotation rates of 2500 rpm. b) Koutecky-Levich plots under different electrolyte conditions from a) with the rotation rates range from 900 rpm to 2500 rpm. c) The correspondence between the S_{K-L}^{-1} and the SO_4^{2-} concentration from b) and its linear fit.

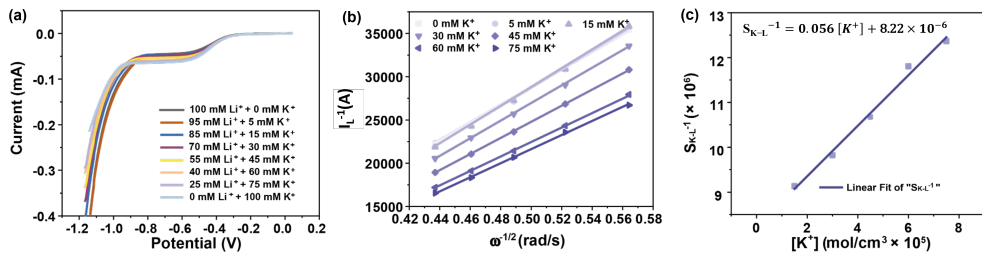


Figure 4. a) Polarization curves recorded on a Au RDE in Ar-saturated 100 mM perchlorate electrolytes with different ratios of cations, with a bulk pH of 4, at 10 mV s^{-1} and a rotation rate of 2500 rpm. b) Koutecky-Levich plots for different electrolyte conditions from a) with the rotation rates ranging from 900 rpm to 2500 rpm (see experimental details in the Supporting Information). c) The correspondence between the S_{K-L}^{-1} and the K^+ concentration from b) and its linear fit.

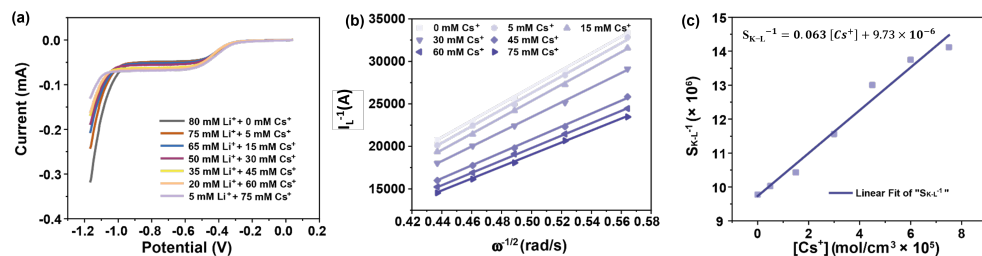


Figure 5. a) Polarization curves recorded on a Au RDE in Ar-saturated 100 mM perchlorate electrolytes with a different ratios of cations with a bulk pH of 4, at 10 mV s^{-1} and a rotation rates of 2500 rpm. b) Koutecky-Levich plots for different electrolyte conditions from a) with the rotation rates ranging from 900 rpm to 2500 rpm. c) The correspondence between the S_{K-L}^{-1} and the Cs^+ concentration from b) and its linear fit.

more pronounced than Singh et al.³⁷ predicted for Cu (8.49 for K^+ , 4.32 for Cs^+) and Ag (7.95 for K^+ , 4.31 for Cs^+) electrodes in a computational study.

Similarly, a quantitative analysis of Cs^+ hydrolysis is shown in Figure 5. The Cs^+ concentration is always below 80 mM due to the limited solubility of Cs^+ . A greater increase in the limiting current density and a corresponding larger slope of 0.063 compared to that of K^+ are observed, showing that hydrated Cs^+ is a slightly better proton donor than K^+ . The pK_a of Cs^+ is determined to be 2.48.

The quantitative investigation in terms of the sulfate electrolyte is carried out involving Li_2SO_4 as a supporting component. In this case the limiting current density of HER is

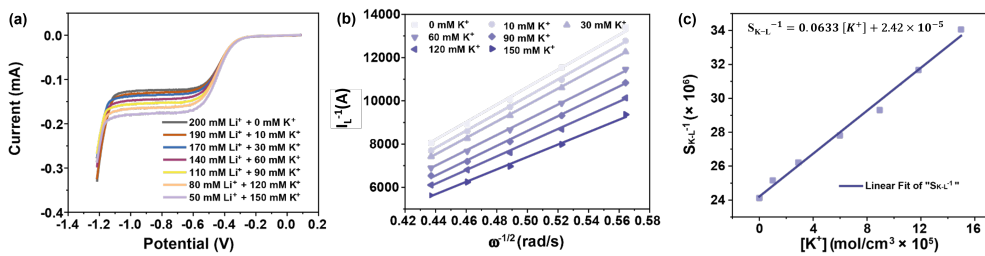


Figure 6. a) Polarization curves recorded on a Au RDE in Ar-saturated 100 mM sulfate electrolytes with a different ratios of cation concentrations with a bulk pH of 4, at 10 mV s⁻¹ and a rotation rate of 2500 rpm. b) Koutecký-Levich plots under different electrolyte conditions from a) with the rotation rates ranging from 900 rpm to 2500 rpm. c) The correspondence between the $S_{\text{K-L}}^{-1}$ and the K^+ concentration from b) and its linear fit.

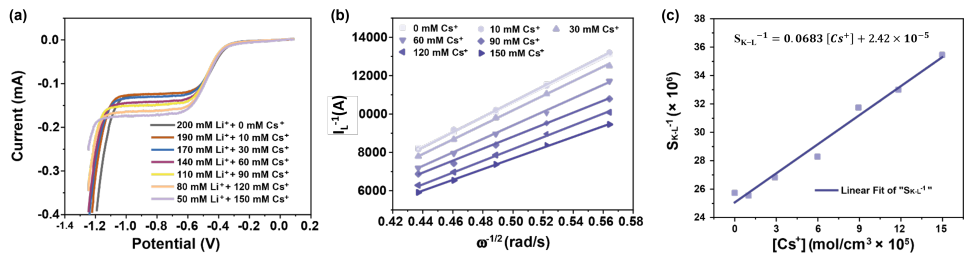


Figure 7. a) Polarization curves recorded on a Au RDE in Ar-saturated 100 mM sulfate electrolytes with a different ratios of cation concentrations with a bulk pH of 4, at 10 mV s⁻¹ and a rotation rates of 2500 rpm. b) Koutecký-Levich plots under different electrolyte conditions from a) with the rotation rates ranging from 900 rpm to 2500 rpm. c) The correspondence between the $S_{\text{K-L}}^{-1}$ and the Cs^+ concentration from b) and its linear fit.

contributed by the bulk protons, the dissociation of HSO_4^- and the hydrolysis of the cation. The hydrated Na^+ is still an ineffective proton-donor in this case with a negligible change in the steady-state current response (see Figure S8 in the supporting information), while the hydrated K^+ and Cs^+ evidently enhance the limiting current density. The linear dependences between S_{K-L}^{-1} and the K^+ and Cs^+ concentrations are shown in Figures 6 and 7, with a slope nearly equivalent to that in perchlorate, but an intercept twice as large. This is attributed to the additional protons from HSO_4^- , which is also suggested by the higher limiting current density compared to the perchlorate solution. Therefore, an additional current density was added to account for the influence from HSO_4^- (Eqs. 13-14):

$$\frac{1}{i} = \frac{\omega^{-1/2}}{0.62nFAD_{\text{cat}}^{2/3}v^{-1/6}K_{\text{cat}}C_{\text{cat}} + 0.62nFAD_{\text{HSO}_4^-}^{2/3}v^{-1/6}K_{\text{HSO}_4^-}C_{(\text{H})\text{SO}_4^-} + 0.62nFAD_{\text{H}}^{2/3}v^{-1/6}C_{\text{H}}} \quad (13)$$

$$S_{K-L}^{-1} = 0.62nFAD_{\text{cat}}^{2/3}v^{-1/6}K_{\text{cat}}C_{\text{cat}} + 0.62nFAD_{\text{H}}^{2/3}v^{-1/6}C_{\text{H}} + 0.62nFAD_{\text{HSO}_4^-}^{2/3}v^{-1/6}K_{\text{HSO}_4^-}C_{(\text{H})\text{SO}_4^-} \quad (14)$$

The pK_a 's of K^+ and Cs^+ are determined to be 2.45 and 2.44, respectively, similar to the results from the values evaluated in perchlorate electrolyte. Taking the diffusion coefficient of the proton as $1.7 \times 10^{-4} \text{ cm}^2 \text{ s}^{-1}$ as determined above, in both K^+ and Cs^+ solutions an identical value of $1.84 \times 10^{-5} \text{ cm}^2 \text{ s}^{-1}$ is obtained for the diffusion coefficient of HSO_4^- , in agreement with the literature data.⁴⁴

A similar analysis was performed in 100 mM perchlorate electrolyte with an increasing Cs^+ content at bulk pH 3.7 (see Figure S9 in the Supporting Information). A S_{K-L} of 0.067 is obtained and the pK_a of Cs^+ and the diffusion coefficient of the proton are evaluated to be 2.46 and $2.17 \times 10^{-4} \text{ cm}^2 \text{ s}^{-1}$, resp. The pK_a agrees well with the results obtained from measurements performed at bulk pH 4, demonstrating that this quantitative analysis is independent of bulk pH.

5.4 Conclusions

In this work, we investigated certain supporting electrolyte species which are also potential proton donors, and their effect on the steady-state hydrogen evolution current at a rotating disk electrode. The species studied including an anionic proton donor, i.e. bisulfate, as well as alkali cations, which have recently been suggested as proton donors in experiments of hydrogen evolution and CO_2 reduction.

By conducting experiments with the bulk pH kept rigorously constant, it was observed that the steady-state behavior of HER discernably varies with the concentration of the protic anion, namely HSO_4^- and the alkali cation, namely K^+ and Cs^+ , while the influence of ClO_4^- , Li^+ and Na^+ is negligible. This is related to the alteration of the reaction flux by coupling proton reduction with homogeneous acid-base equilibria, namely, dissociation of HSO_4^- and hydrolysis of K^+ and Cs^+ . Of these ions, HSO_4^- has the biggest influence, even though the

electrolyte condition is outside its typical buffering range, while the cations serve as a weak buffer with limited capacity. Quantitative studies conducted in both perchlorate and sulfate solutions elucidated that the steady state current of HER can be modeled as a mass transport limited process coupled to a chemical reaction (i.e. the acid-base reaction). A linear variation of the Koutecký-Levich slope with respect to the concentration of electro-inactive species was observed, from which the pK_a of the proton donor involved can be extracted. The corresponding pK_a 's of HSO_4^- , K^+ and Cs^+ were determined to be 2.06, 2.52 and 2.48, respectively. Specifically, these studies confirm that alkali cation species can act as proton donors and (weak) buffering agents near electrode surfaces, and that their effect can be quantified experimentally.

References

- (1)Shih, A. J.; Monteiro, M. C. O.; Dattila, F.; Pavesi, D.; Philips, M.; da Silva, A. H. M.; Vos, R. E.; Ojha, K.; Park, S.; van der Heijden, O.; Marcandalli, G.; Goyal, A.; Villalba, M.; Chen, X.; Gunasooriya, G. T. K. K.; McCrum, I.; Mom, R.; López, N.; Koper, M. T. M., Water electrolysis. *Nature Reviews Methods Primers* **2022**, 2 (1).
- (2)Zou, X.; Zhang, Y., Noble metal-free hydrogen evolution catalysts for water splitting. *Chem Soc Rev* **2015**, 44 (15), 5148-80.
- (3)Huang, J. E.; Li, F.; Ozden, A.; Sedighian Rasouli, A.; García de Arquer, F. P.; Liu, S.; Zhang, S.; Luo, M.; Wang, X.; Lum, Y.; Xu, Y.; Bertens, K.; Miao, R. K.; Dinh, C.-T.; Sinton, D.; Sargent, E. H., CO₂ electrolysis to mult carbon products in strong acid. *Science* **2021**, 372 (6546), 1074-1078.
- (4)Marcandalli, G.; Monteiro, M. C. O.; Goyal, A.; Koper, M. T. M., Electrolyte Effects on CO₂ Electrochemical Reduction to CO. *Acc. Chem. Res.* **2022**, 55 (14), 1900-1911.
- (5)Wu, J.; Wafula, F.; Branagan, S.; Suzuki, H.; van Eisdien, J., Mechanism of cobalt bottom-up filling for advanced node interconnect metallization. *Journal of the Electrochemical Society* **2018**, 166 (1), D3136.
- (6)Schlesinger, M.; Paunovic, M., *Modern electroplating*. John Wiley & Sons: 2014; Vol. 52.
- (7)Monteiro, M. C. O.; Liu, X.; Hagedoorn, B. J. L.; Snabilié, D. D.; Koper, M. T. M., Interfacial pH Measurements Using a Rotating Ring-Disc Electrode with a Voltammetric pH Sensor. *ChemElectroChem* **2021**, 9 (1), e202101223.
- (8)Mukouyama, Y.; Nakanishi, S., An Ordinary Differential Equation Model for Simulating Local-pH Change at Electrochemical Interfaces. *Frontiers in Energy Research* **2020**, 8.
- (9)Zhu, J.; Hu, L.; Zhao, P.; Lee, L. Y. S.; Wong, K. Y., Recent Advances in Electrocatalytic Hydrogen Evolution Using Nanoparticles. *Chem Rev* **2020**, 120 (2), 851-918.
- (10)Dubouis, N.; Grimaud, A., The hydrogen evolution reaction: from material to interfacial descriptors. *Chem Sci* **2019**, 10 (40), 9165-9181.
- (11)Nagel, K.; Wendler, F., Die Wasserstoffelektrode als zweifache Elektrode. *Zeitschrift für*
95

Elektrochemie, Berichte der Bunsengesellschaft für physikalische Chemie **1956**, 60 (9-10), 1064-1072.

(12)Ooka, H.; Figueiredo, M. C.; Koper, M. T. M., Competition between Hydrogen Evolution and Carbon Dioxide Reduction on Copper Electrodes in Mildly Acidic Media. *Langmuir* **2017**, 33 (37), 9307-9313.

(13)Goyal, A.; Koper, M. T. M., The Interrelated Effect of Cations and Electrolyte pH on the Hydrogen Evolution Reaction on Gold Electrodes in Alkaline Media. *Angew Chem Int Ed Engl* **2021**, 60 (24), 13452-13462.

(14)Levich, V. G.; Tobias, C. W., Physicochemical hydrodynamics. *Journal of The Electrochemical Society* **1963**, 110 (11), 251C.

(15)Bard, A. J.; Faulkner, L. R., *Electrochemical Methods: Fundamentals and Applications*. Wiley: 2012.

(16)Treimer, S.; Tang, A.; Johnson, D. C., A Consideration of the application of Koutecký-Levich plots in the diagnoses of charge-transfer mechanisms at rotated disk electrodes. *Electroanalysis* **2002**, 14 (3), 165-171.

(17)Leal, P. H. M.; Barcia, O. E.; Mattos, O. R., Numerical Analysis of CE Processes in RDE Systems: Diffusion and Electro-hydrodynamic Impedances. *Journal of The Electrochemical Society* **2020**, 167 (2), 026502.

(18)Amatore, C.; Fosset, B.; Bartelt, J.; Deakin, M.; Wightman, R., Electrochemical kinetics at microelectrodes: Part V. Migrational effects on steady or quasi-steady-state voltammograms. *Journal of electroanalytical chemistry and interfacial electrochemistry* **1988**, 256 (2), 255-268.

(19)Ciszkowska, M.; Stojek, Z.; Morris, S. E.; Osteryoung, J. G., Steady-state voltammetry of strong and weak acids with and without supporting electrolyte. *Analytical Chemistry* **1992**, 64 (20), 2372-2377.

(20)Stojek, Z.; Ciszkowska, M.; Osteryoung, J. G., Self-enhancement of voltammetric waves of weak acids in the absence of supporting electrolyte. *Analytical Chemistry* **1994**, 66 (9), 1507-1512.

(21)Jaworski, A.; Stojek, Z.; Osteryoung, J. G., A simple theoretical model for the self-enhancement of the cathodic voltammetric waves of weak acids. *Analytical Chemistry* **1995**, 67 (18), 3349-3352.

(22)Rebouillat, S.; Lyons, M. E. G.; Bannon, T., Evaluation of the proton transfer kinetics of potential electrolytes in non-aqueous solutions using electrochemical techniques Part 1. Kinetic analysis of the general CE mechanism at stationary and rotating electrodes. *J. Solid State Electrochem.* **1999**, 3 (4), 215-230.

(23)Leal, P.; Leite, N.; Viana, P.; de Sousa, F.; Barcia, O.; Mattos, O., Numerical analysis of the steady-state behavior of CE processes in rotating disk electrode systems. *Journal of The Electrochemical Society* **2018**, 165 (9), H466.

(24)Koutecký, J.; Levich, V., The use of a rotating disk electrode in the studies of electrochemical kinetics and electrolytic processes. *Zh. Fiz. Khim* **1958**, 32, 1565-1575.

(25)Dogonadze, R., Use of Rotating Disk Electrode in the Study of the Electrochemical Kinetic and Catalytic Processes. The Case of Different Diffusion Coefficients. *Zh. Fiz. Khim.* **1958**, 32, 2437-2442.

(26)Hale, J., Transients in convective systems: I. Theory of galvanostatic, and galvanostatic with current

reversal transients, at a rotating disc electrode. *Journal of Electroanalytical Chemistry* (1959) **1963**, 6 (3), 187-197.

(27)Compton, R.; Laing, M.; Mason, D.; Northing, R.; Unwin, P., Rotating disc electrodes: the theory of chronoamperometry and its use in mechanistic investigations. *Proceedings of the Royal Society of London. A. Mathematical and Physical Sciences* **1988**, 418 (1854), 113-154.

(28)Marinović, V.; Despić, A. R., Cathodic Hydrogen Evolution from Aqueous Solutions of Acetic Acid. *Russian Journal of Electrochemistry* **2004**, 40, 995-999.

(29)Marinović, V.; Despić, A., Hydrogen evolution from solutions of citric acids. *Journal of Electroanalytical Chemistry* **1997**, 431 (1), 127-132.

(30)Marinović, V.; Despić, A., Pyrophosphoric acid as a source of hydrogen in cathodic hydrogen evolution on silver. *Electrochimica acta* **1999**, 44 (23), 4073-4077.

(31)Monteiro, M. C. O.; Dattila, F.; López, N.; Koper, M. T. M., The Role of Cation Acidity on the Competition between Hydrogen Evolution and CO₂ Reduction on Gold Electrodes. *J. Am. Chem. Soc.* **2021**, 144 (4), 1589-1602.

(32)Marcandalli, G.; Boterman, K.; Koper, M. T. M., Understanding hydrogen evolution reaction in bicarbonate buffer. *J. Catal.* **2022**, 405, 346-354.

(33)Cosijn, A. M., Diffusion polarisation of the hydrogen electrode: I. Theory. *Journal of Electroanalytical Chemistry* (1959) **1961**, 2 (6), 437-451.

(34)Jackson, M. N.; Jung, O.; Lamotte, H. C.; Surendranath, Y., Donor-Dependent Promotion of Interfacial Proton-Coupled Electron Transfer in Aqueous Electrocatalysis. *ACS Catal.* **2019**, 9 (4), 3737-3743.

(35)Moreno-Garcia, P.; Kovacs, N.; Grozovski, V.; Galvez-Vazquez, M. J.; Vesztergom, S.; Broekmann, P., Toward CO(2) Electroreduction under Controlled Mass Flow Conditions: A Combined Inverted RDE and Gas Chromatography Approach. *Anal Chem* **2020**, 92 (6), 4301-4308.

(36)Liu, X.; Koper, M. T. M., Tuning the Interfacial Reaction Environment for CO(2) Electroreduction to CO in Mildly Acidic Media. *J Am Chem Soc* **2024**, 146 (8), 5242-5251.

(37)Singh, M. R.; Kwon, Y.; Lum, Y.; Ager, J. W., 3rd; Bell, A. T., Hydrolysis of Electrolyte Cations Enhances the Electrochemical Reduction of CO₂ over Ag and Cu. *J. Am. Chem. Soc.* **2016**, 138 (39), 13006-13012.

(38)Liu, X.; Monteiro, M. C. O.; Koper, M. T. M., Interfacial pH measurements during CO(2) reduction on gold using a rotating ring-disk electrode. *Phys. Chem. Chem. Phys.* **2023**, 25 (4), 2897-2906.

(39)Ayemoba, O.; Cuesta, A., Spectroscopic Evidence of Size-Dependent Buffering of Interfacial pH by Cation Hydrolysis during CO₂ Electroreduction. *ACS Appl Mater Interfaces* **2017**, 9 (33), 27377-27382.

(40)Zhang, F.; Co, A. C., Direct evidence of local pH change and the role of alkali cation during CO₂ electroreduction in aqueous media. *Angewandte Chemie International Edition* **2020**, 59 (4), 1674-1681.

(41)Kamat, G. A.; Zamora Zeledón, J. A.; Gunasooriya, G. K. K.; Dull, S. M.; Perryman, J. T.; Nørskov, J. K.; Stevens, M. B.; Jaramillo, T. F., Acid anion electrolyte effects on platinum for oxygen and hydrogen

electrocatalysis. *Communications Chemistry* **2022**, *5* (1), 20.

(42) Lu, X.; Tu, W.; Zhou, Y.; Zou, Z., Effects of electrolyte ionic species on electrocatalytic reactions: advances, challenges, and perspectives. *Advanced Energy Materials* **2023**, *13* (27), 2300628.

(43) Monteiro, M. C. O.; Goyal, A.; Moerland, P.; Koper, M. T. M., Understanding Cation Trends for Hydrogen Evolution on Platinum and Gold Electrodes in Alkaline Media. *ACS Catal* **2021**, *11* (23), 14328-14335.

(44) Lide, D. R., *CRC handbook of chemistry and physics*. CRC press: 2004; Vol. 85.



Appendix A

Supporting Information to Chapter 2



Calculation of the interfacial disc pH

The relationship between the concentration of protons at the disk and at the ring is shown in Equation S1^[1], originally derived by Albery and Calvo, and the extended theory taking the autoprotolysis of water into account in Equation S2 by Yokoyama et al.^[2] (for unbuffered systems). Here, c_r and c_d are the concentrations of either H^+ or OH^- at the ring and disk, respectively. c_∞ is the electrolyte bulk proton concentration and N_D is the detection efficiency. N_D is given by Equation S3 and Equation S4 and calculated based on the electrode geometry (Figure S2). Figure S2a and Figure S2b show the theoretical relationship between the interfacial ring (pH_{ring}) and disc (pH_{disc}) pH for unbuffered solutions of different bulk pH using Equation S1 and Equation S2, respectively. Here, it becomes clear how the description from Yokoyama is more sensitive in a wider pH range (for a direct comparison see Figure 2 in Yokoyama et al.^[2]).

$$c_r = c_\infty + N_D(c_d - c_\infty) \quad \text{Equation S1}$$

$$c_{r,\text{H}^+} - c_{r,\text{OH}^-} = N_D(c_{d,\text{H}^+} - c_{d,\text{OH}^-}) + (1 - N_D)(c_{\infty,\text{H}^+} - c_{\infty,\text{OH}^-}) \quad \text{Equation S2}$$

$$N_D = 1 - \frac{1}{6}F\left[\left(\frac{r_2}{r_1}\right)^3 - 1\right] - \frac{2}{3}F\left[\left(\frac{r_2+r_3}{2r_1}\right)^3 - 1\right] - \frac{1}{6}F\left[\left(\frac{r_3}{r_1}\right)^3 - 1\right] \quad \text{Equation S3}$$

Where $F[x]$ is:

$$F[x] = \frac{\frac{1}{3^{\frac{2}{3}}}}{4\pi} \ln\left(\frac{\left(1+x^{\frac{1}{3}}\right)^3}{1+x}\right) + \frac{3}{2} \tan^{-1}\left(\frac{2x^{\frac{1}{3}}-1}{3^{\frac{1}{2}}}\right) + \frac{1}{4} \quad \text{Equation S4}$$

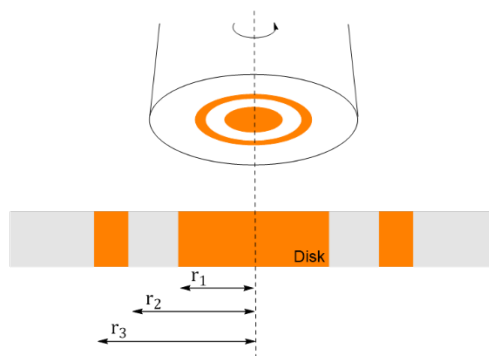


Figure S1. Schematic representation of the rotating ring-disk electrode with the geometrical parameters from Equation S3 indicated.

For buffered systems, we correct Equation S2 to take into account the homogeneous reaction taking place in solution, in the case of our work, involving the phosphate species in the electrolyte. In this case, the consumption of OH^- by the different phosphate species in considered and the corrected concentration of $\text{OH}^- (c'_{\text{OH}^-})$ is given by:

$$c'_{OH^-} = c_{OH^-} + [H_2PO_4^-] + 2[HPO_4^{2-}] + 3[PO_4^{3-}] \quad \text{Equation S5}$$

The following equilibrium constants and equations were used to calculate the concentration of phosphate species^[3]:

$$H_3PO_4 \rightleftharpoons H_2PO_4^- + H^+ \quad K_{a1} = 7.5 \times 10^{-3} \quad \text{Equation S6}$$

$$H_2PO_4^- \rightleftharpoons HPO_4^{2-} + H^+ \quad K_{a2} = 6.2 \times 10^{-8} \quad \text{Equation S7}$$

$$HPO_4^{2-} \rightleftharpoons PO_4^{3-} + H^+ \quad K_{a3} = 2.14 \times 10^{-13} \quad \text{Equation S8}$$

The total concentration of species is given by TC and the concentration of each species to be used in Equation S5 is determined based on Equations S9-S13:

$$TC = [H_3PO_4] + [H_2PO_4^-] + [HPO_4^{2-}] + [PO_4^{3-}] \quad \text{Equation S9}$$

$$[H_3PO_4] = \frac{TC[H^+]^3}{[H^+]^3 + K_{a1}[H^+]^2 + K_{a1}K_{a2}[H^+] + K_{a1}K_{a2}K_{a3}} \quad \text{Equation S10}$$

$$[H_2PO_4^-] = \frac{TC K_{a1}[H^+]^2}{[H^+]^3 + K_{a1}[H^+]^2 + K_{a1}K_{a2}[H^+] + K_{a1}K_{a2}K_{a3}} \quad \text{Equation S11}$$

$$[HPO_4^{2-}] = \frac{TC K_{a1}K_{a2}[H^+]}{[H^+]^3 + K_{a1}[H^+]^2 + K_{a1}K_{a2}[H^+] + K_{a1}K_{a2}K_{a3}} \quad \text{Equation S12}$$

$$[PO_4^{3-}] = \frac{TC K_{a1}K_{a2}K_{a3}}{[H^+]^3 + K_{a1}[H^+]^2 + K_{a1}K_{a2}[H^+] + K_{a1}K_{a2}K_{a3}} \quad \text{Equation S13}$$

Finally, expanding Equation S5, the relationship between the interfacial pH_{ring} and pH_{disc} for a phosphate buffered electrolyte is given by Equation S14.

$$N_D = \frac{c_{r, OH^-} + [H_2PO_4^-]_r + 2[HPO_4^{2-}]_r + 3[PO_4^{3-}]_r - c_{\infty, OH^-} - [H_2PO_4^-]_{\infty} - 2[HPO_4^{2-}]_{\infty} - 3[PO_4^{3-}]_{\infty}}{c_{d, OH^-} + [H_2PO_4^-]_d + 2[HPO_4^{2-}]_d + 3[PO_4^{3-}]_d - c_{\infty, OH^-} - [H_2PO_4^-]_{\infty} - 2[HPO_4^{2-}]_{\infty} - 3[PO_4^{3-}]_{\infty}} \quad \text{Equation S14}$$

A quartic equation can be derived from Equation S5-S14, where a , b , c , d , and e are parameters of C_{r, OH^-} , and x stands for C_{d, H^+} .

$$ax^4 + bx^3 + cx^2 + dx + e = 0 \quad \text{Equation S15}$$

Solving the equation, four roots can be obtained and the nature of which can be inferred from the sign of the discriminants Δ , P and D . In our cases, all the roots are real and distinct roots since the $\Delta > 0$, $P < 0$ and $D < 0$.

$$\begin{aligned} \Delta = & 256a^3e^3 - 192a^2bde^2 - 128a^2c^2e^2 + 144a^2cd^2e - 27a^2d^4 + 144ab^2ce^2 - \\ & 6ab^2d^2e - 80abc^2de + 18abcd^3 + 16ac^4e - 4ac^3d^2 - 27b^4e^2 + 18b^3cde - 4b^3d^3 - \\ & 4b^2c^3e + b^2c^2d^2 \end{aligned} \quad \text{Equation S16}$$

$$P = 8ac - 3b^2 \quad \text{Equation S17}$$

$$D = 64a^3e - 16a^2c^2 + 16ab^2c - 16a^2bd - 3b^4 \quad \text{Equation S18}$$

So that

$$x_{1,2} = -\frac{b}{4a} - S \pm \frac{1}{2} \sqrt{-4S^2 - 2p + \frac{q}{S}} \quad \text{Equation S19}$$

$$x_{3,4} = -\frac{b}{4a} + S \pm \frac{1}{2} \sqrt{-4S^2 - 2p - \frac{q}{S}} \quad \text{Equation S20}$$

Where:

$$p = \frac{8ac - 3b^2}{8a^2} \quad \text{Equation S21}$$

$$q = \frac{b^3 - 4abc + 8a^2d}{8a^3} \quad \text{Equation S22}$$

$$S = -\frac{1}{2} \sqrt{-\frac{2}{3}p + \frac{2}{3a}\sqrt{\Delta_0} \cos \frac{\varphi}{3}} \quad \text{Equation S21}$$

$$\varphi = \cos^{-1} \left(\frac{\Delta_1}{2\sqrt{\Delta_0^3}} \right) \quad \text{Equation S22}$$

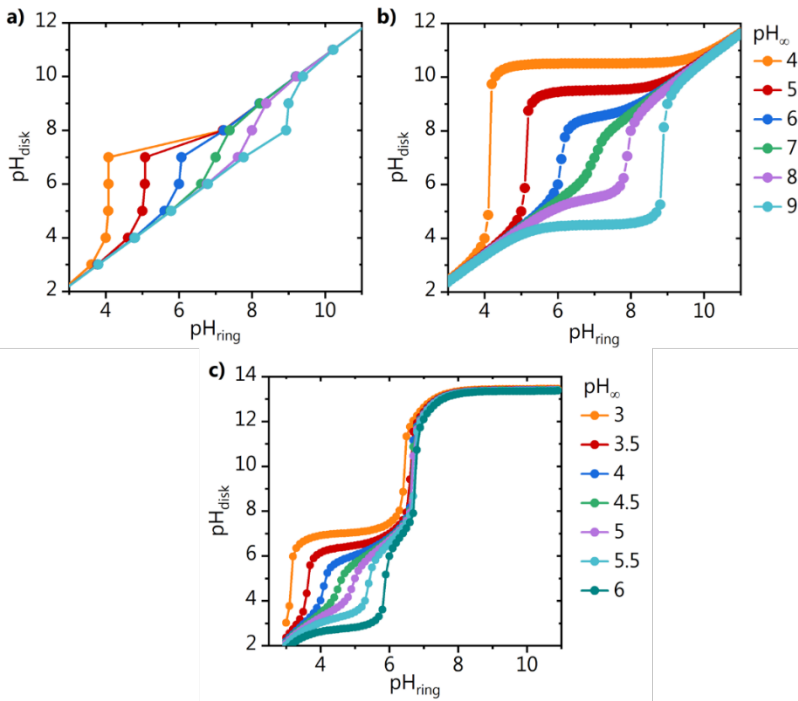


Figure S2. Theoretical relationship between interfacial pH_{ring} and pH_{disk} for different bulk pH (pH_{∞}) using a) the analytical equation reported by Albery and Calvo^[1] and b) the extended theory, reported by Yokoyama et al.^[2] (both for unbuffered systems), and c) the correction presented in this work for a phosphate buffered electrolyte.

With:

$$\Delta_0 = c^2 - 3bd + 12ae \quad \text{Equation S23}$$

$$\Delta_1 = 2c^3 - 9bcd + 27b^2e + 27ad^2 - 72ace \quad \text{Equation S24}$$

The analytical equations S19 and S20 are solved analytically. C_{d,H^+} can be determined out of the four solutions by limiting x (C_{d,H^+}) to be positive and relatively smaller than the corresponding C_{r,H^+} . The theoretical relationship that can be obtained using this description between the interfacial ring (pH_{ring}) and disc (pH_{disc}) pH for phosphate buffered solutions of different bulk pH is shown in Figure S2c.

pH measurements

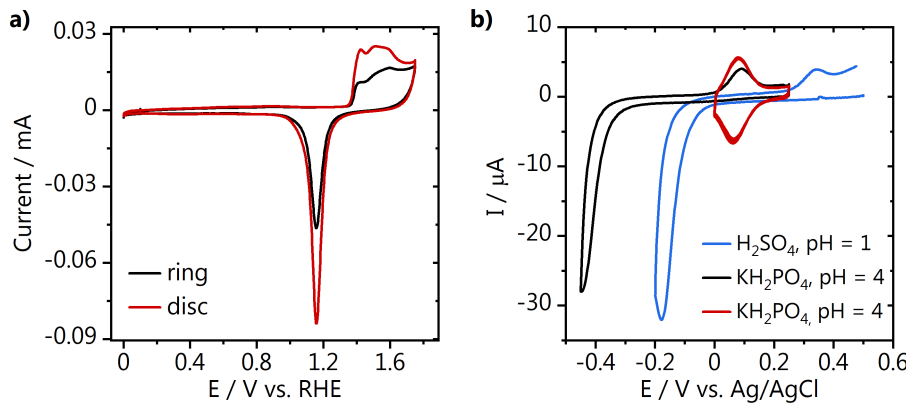


Figure S3. a) Blank voltammetry of the ring (black) and disc (red) electrodes taken in 0.1 M H_2SO_4 at 50 mV s^{-1} . b) cyclic voltammetry of the 4-NTP to 4-HATP conversion in 0.1 M KH_2PO_4 (black, 100 mV s^{-1}) and 0.1 M H_2SO_4 (blue), together with a characterization of the 4-HATP/4-NSTP redox couple (red, 200 mV s^{-1}) in phosphate.

A

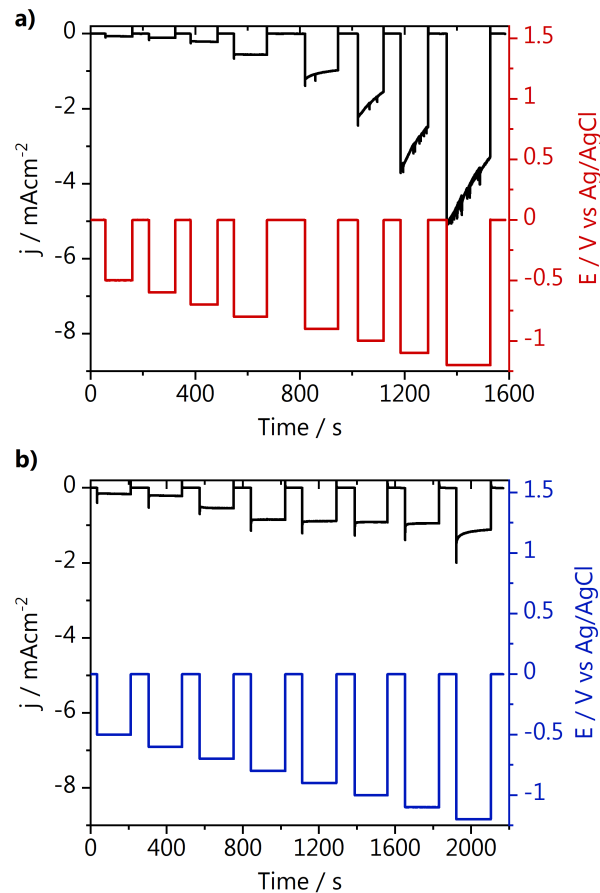


Figure S 4. Chronoamperometry from pH measurements at different potentials in 0.1 M argon saturated a) KH_2PO_4 $\text{pH}_{\text{bulk}} = 4.4$ and b) K_2SO_4 $\text{pH}_{\text{bulk}} = 3.6$ at 1600 rpm.

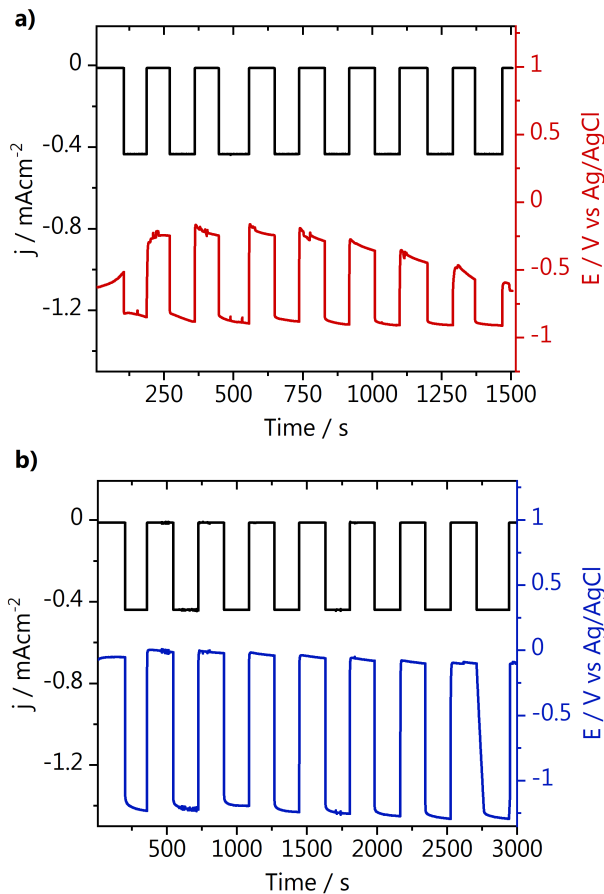


Figure S 5. Chronopotentiometry from pH measurements in 0.1 M argon saturated a) KH_2PO_4 $\text{pH}_{\text{bulk}} = 4.4$ and b) K_2SO_4 $\text{pH}_{\text{bulk}} = 4.0$ at different rotations (500, 750, 1000, 1250, 1500, 1750, 2000, 2600 rpm).

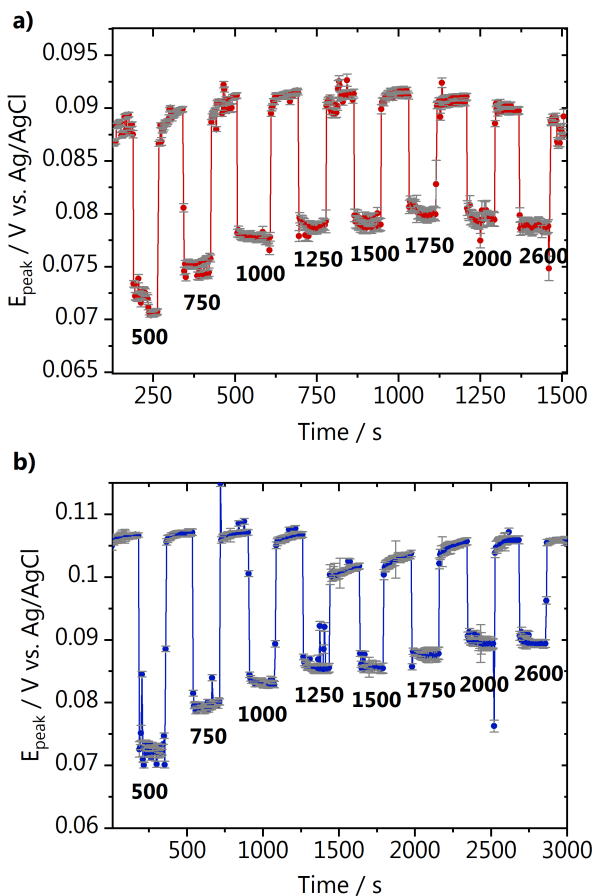
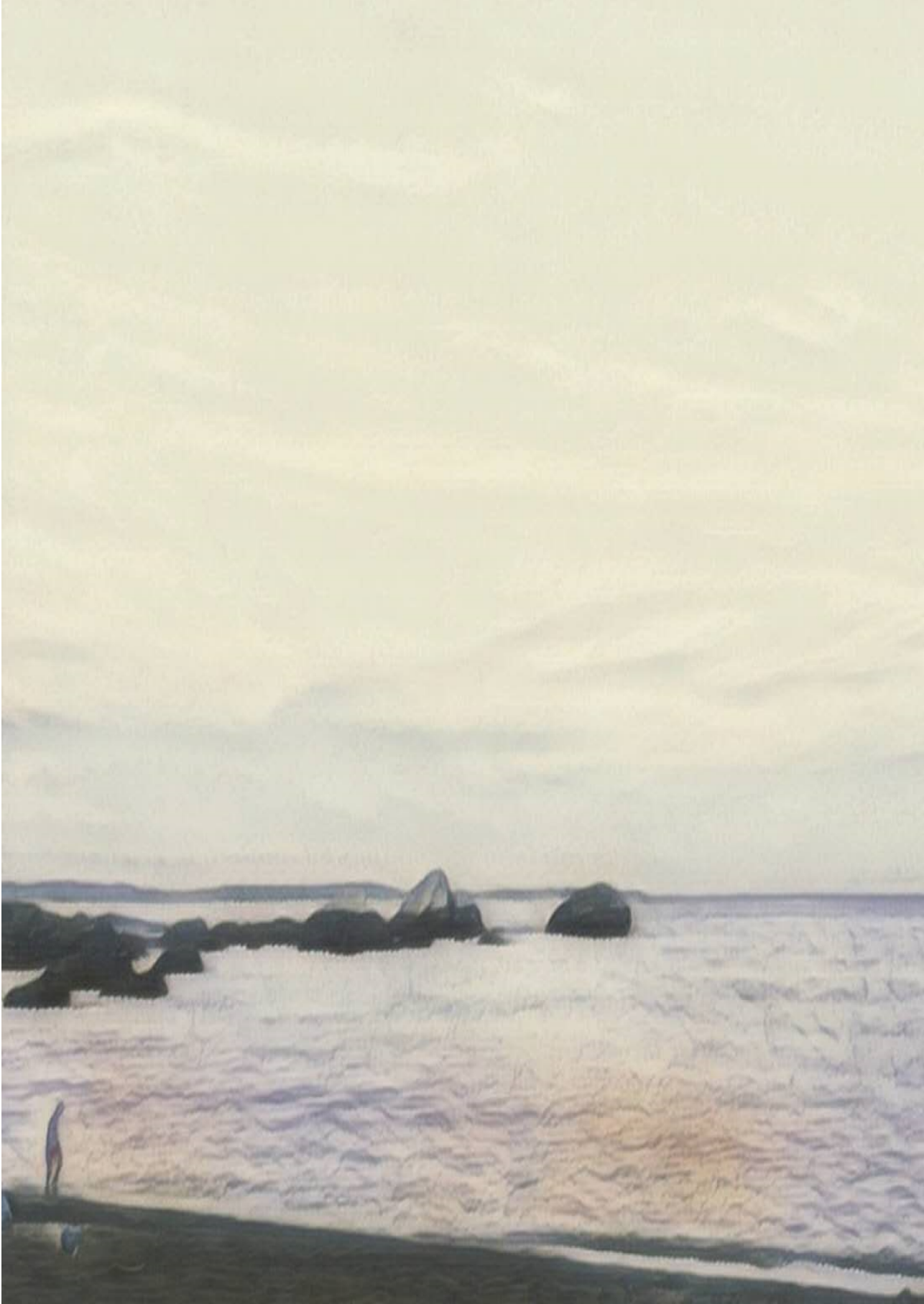


Figure S 6. Mid-peak potential extracted from the 4-HATP/4-NSTP voltammetry for the experiment in 0.1 M argon saturated a) KH_2PO_4 $\text{pH}_{\text{bulk}} = 4.4$ and b) K_2SO_4 $\text{pH}_{\text{bulk}} = 4.0$ at different rotations (500, 750, 1000, 1250, 1500, 1750, 2000, 2600 rpm).

References

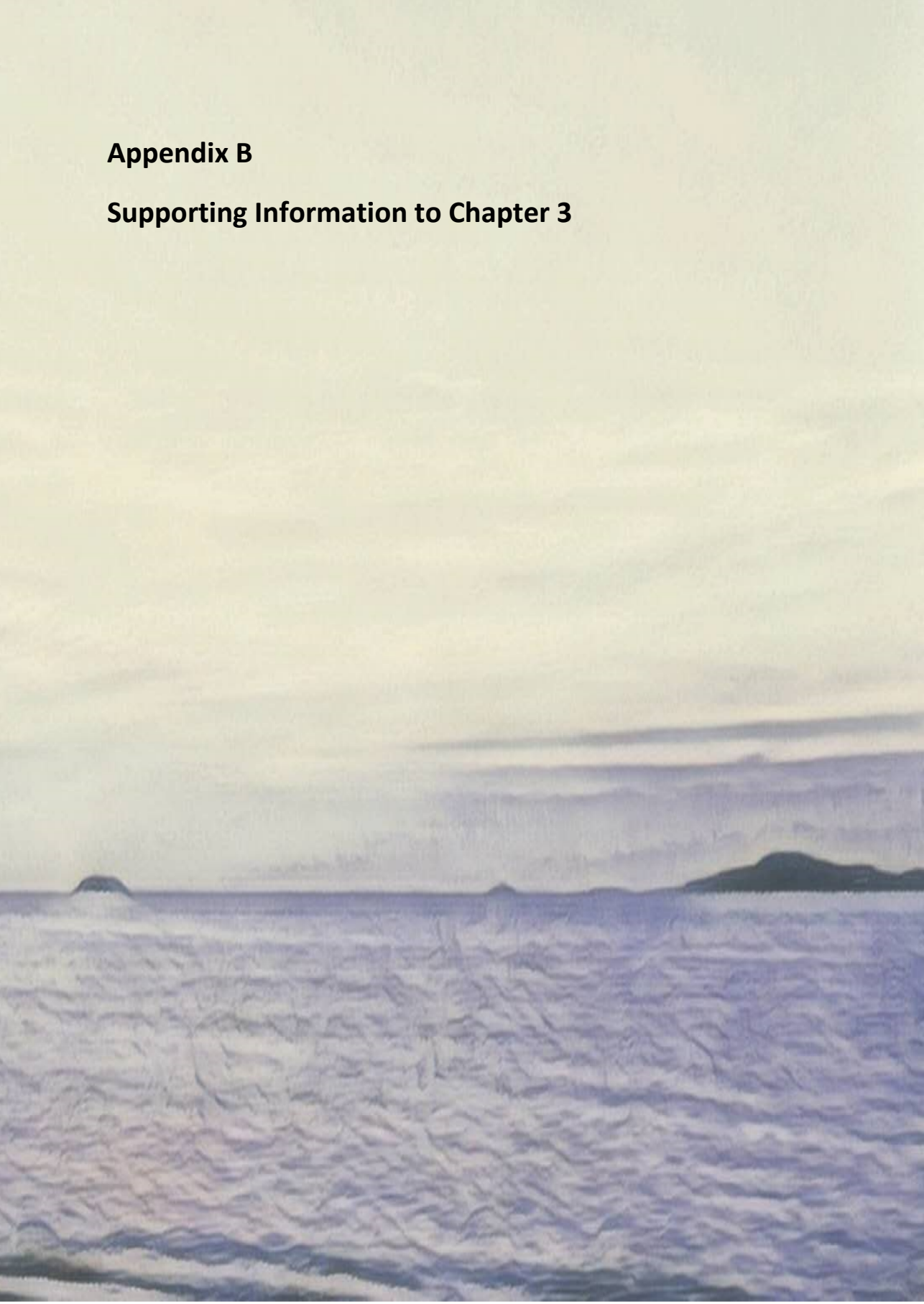
- [1] E. J. Calvo, W. J. Albery, *J. Chem. Soc. Faraday Trans. 1* **1983**, *79*, 2583–2596.
- [2] Y. Yokoyama, K. Miyazaki, Y. Miyahara, T. Fukutsuka, T. Abe, *ChemElectroChem* **2019**, *4750*–4756.
- [3] K. J. Powell, P. L. Brown, R. H. Byrne, T. Gajda, G. Hefter, S. Sjöberg, H. Wanner, *Pure Appl. Chem.* **2005**, *77*, 739–800.

A



Appendix B

Supporting Information to Chapter 3



Cyclic voltammograms of 4-NTP reduction

As shown in Figure S1a, before measurements, to confirm the cleanliness of the electrodes and measure the ECSA, both ring and disk electrodes were characterized in Ar-saturated 0.1 M H₂SO₄ by cyclic voltammetry between 0 and 1.75 V vs RHE. After that, the gold ring was modified with the 4-NTP molecule, and then the 4-NTP was converted into the pH sensing redox couple 4-NSTP/4-HATP using a voltammetry in 0.1 M H₂SO₄ from 0.68 V vs RHE at 100 mV s⁻¹ (Figure S1b). During the negative-going potential sweep, part of the 4-NTP is reduced completely to 4-ATP through a 6-proton-6-electron pathway,¹ while some 4-NTP was reduced partially to the 4-NSTP through a 4-proton-4-electron pathway, and the 4-NSTP is re-oxidized to 4-HATP in the positive-going potential sweep (Figure S1c).² As intermediates of the reduction, the content of 4-NSTP/4-HATP drops with decreasing lower vertex potentials (Figure S1d). Therefore, 0.11V vs RHE was used as lower vertex potential to optimize signals from the redox couple.

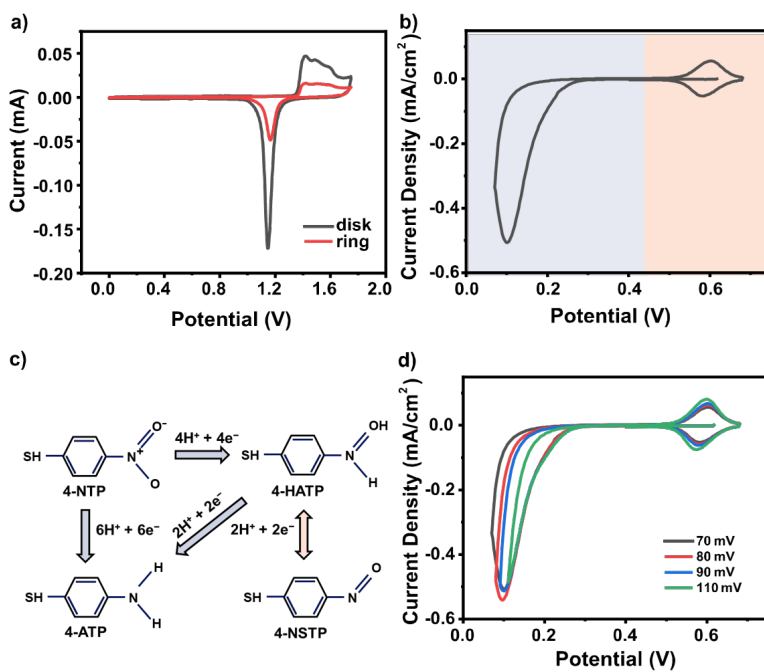


Figure S1. a) Blank voltammograms of the ring (black) and disc (red) electrodes taken in 0.1 M H₂SO₄ at 100 mV s⁻¹. b) the Voltammogram of conversion from 4-NTP to the4-NSTP/4-HATP redox couple in Ar-saturated 0.1M H₂SO₄ at 100mV/s.c) scheme of the reduction pathways of 4-NTP; d) Reduction of 4-NTP with different vertex potentials during cyclic voltammetry in Ar-saturated 0.1M H₂SO₄ at 100mV/s.

Calibration Curve

The peak potentials of the pH redox couple were measured by cyclic voltammetry in electrolytes with different pH. The alkaline region was measured in 0.1 M KHCO₃ with pH adjusted by adding KOH or purging CO₂. The acidic region was measured in CO₂ saturated 0.1 M NaClO₄. pH was measured by a pH meter (lab 855, SI Analytics)

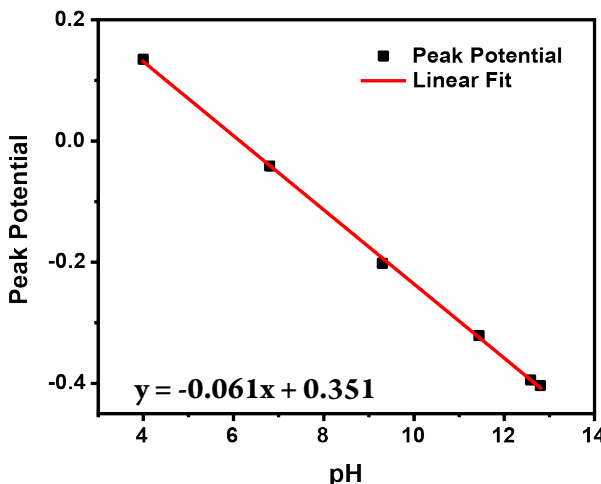


Figure S2. Calibration curve of the 4-NSTP/4-HATP redox couple.

Calculation of the interfacial pH

The interfacial pH at the disk was deduced from the peak potential of the 4-NSTP/4-HATP pH sensing couple. During RRDE measurements, cyclic voltammograms of the 4-HATP/4-NSTP modified Au ring were constantly recorded, the peak potentials of which shifted negatively with the increasing pH (Figure S3a). Firstly, these peak potentials were determined by fitting the anodic scans with a Gaussian function with a linear background. Using the calibration curve ($\text{pH}_{\text{RING}} = (0.351 - E) / 0.061$, see Figure S2b), interfacial pH on the ring electrode was obtained from the peak potential (Figure S3b). Then, the interfacial pH of the disk electrode was calculated according to the well-defined concentration profile of RRDE, developed from the convective diffusion equation by Albery and Calvo.³ The ratio between the average concentration of products on the ring and the disk is defined as the detection efficiency N_D (Eq. s2), where μ is the normalized concentration of products (Eq. s1), C_{∞} is the bulk concentration and subscripts "d" and "r" stand for the ring and disk electrode, respectively. N_D depends only on the geometry of the electrode (Eqs. s3-4),

where r_1 , r_2 and r_3 are the radii of the disk, the inner ring and the outer ring, respectively.⁴ In our case, the designated product here is OH^- . As the current on the ring is far smaller than on the disk, it is assumed that the electric field from the ring barely influences the concentration profile of OH^- . Under strong polarization in highly conductive electrolytes, the current distribution within the disk is assumed to be uniform.⁵ Consequently, the N_D of the RRDE tip employed here ($r_1 = 5.0$ mm, $r_2 = 6.5$ mm, $r_3 = 7.5$ mm) is calculated to be 0.23 according to Eq. s4.

However, in CO_2 -saturated bicarbonates, OH^- generated on the disk is partially consumed by either CO_2 or HCO_3^- on its way to the ring. To avoid an underestimation of the interfacial pH on the disk, these homogeneous buffering reactions (Eqs 2 and 4) are taken into account.

⁶ With effective buffering from $\text{CO}_2/\text{HCO}_3^-$ and $\text{HCO}_3^-/\text{CO}_3^{2-}$, autoprotolysis of water is ignored here. Therefore, the normalized concentration μ here was defined as Eq. s5 and the equation for N_D was also modified (Eq. s6). As CO_2 is continuously purged into the electrolyte during the measurements, the total carbon concentration (TC, see Eq. s7), which is the sum of the concentration of the intrinsic bicarbonate electrolyte and the saturated CO_2 concentration from extrinsic bubbling, stays constant (the TCs for 0.1, 0.25, 0.4 and 0.5 M bicarbonate under continuous CO_2 bubbling are 0.135, 0.271, 0.429, 0.526 M respectively).

⁷ Concentrations of the different carbonaceous species were estimated as a function of pH (Eqs. s8-s10) by combining equilibrium constants from Eq. 2 and 4 and Eq. s7 ($K_2 = \frac{[\text{H}^+][\text{HCO}_3^-]}{[\text{CO}_2]}$, $pK_2 = 6.35$, $K_4 = \frac{[\text{H}^+][\text{CO}_3^{2-}]}{[\text{HCO}_3^-]}$, $pK_4 = 10.33$).⁷ As a result, the interfacial pH of the

disk electrode was derived from Eqs. S6-s10. The theoretical correlation between the pH on the ring and disk is plotted in Figure S3c. The appearance of two turning points is related to the two buffers in the electrolyte.

$$\mu = (C - C_\infty)/C_\infty \quad (\text{s1})$$

$$N_D = \frac{\mu_r}{\mu_{D,0}} = (C_r - C_\infty)/(C_d - C_\infty) \quad (\text{s2})$$

$$F(\theta) = \frac{\frac{1}{3^2}}{4\pi} \ln \left(\frac{\left(1 + \theta^{\frac{1}{3}}\right)^3}{1 + \theta} \right) + \frac{3}{2\pi} \tan^{-1} \left(\frac{2\theta^{\frac{1}{3}} - 1}{\frac{1}{3^2}} \right) + \frac{1}{4} \quad (\text{s3})$$

$$N_D = 1 - \frac{1}{6} F \left[\left(\frac{r_2}{r_1} \right)^3 - 1 \right] - \frac{2}{3} F \left[\left(\frac{r_2 + r_3}{2r_1} \right)^3 - 1 \right] - \frac{1}{6} F \left[\left(\frac{r_3}{r_1} \right)^3 - 1 \right] \quad (\text{s4})$$

$$\mu_{\text{OH}^-} = \frac{(C_{\text{OH}^-} + C_{\text{HCO}_3^-} + 2C_{\text{CO}_3^{2-}} - C_{\infty, \text{OH}^-} - C_{\infty, \text{HCO}_3^-} - 2C_{\infty, \text{CO}_3^{2-}})}{(C_{\infty, \text{OH}^-} + C_{\infty, \text{HCO}_3^-} + 2C_{\infty, \text{CO}_3^{2-}})} \quad (\text{s5})$$

$$N_D = \frac{\mu_{r, \text{OH}^-}}{\mu_{d, \text{OH}^-}} = \frac{C_{r, \text{OH}^-} + C_{r, \text{HCO}_3^-} + 2C_{r, \text{CO}_3^{2-}} - C_{\infty, \text{OH}^-} - C_{\infty, \text{HCO}_3^-} - 2C_{\infty, \text{CO}_3^{2-}}}{C_{d, \text{OH}^-} + C_{d, \text{HCO}_3^-} + 2C_{d, \text{CO}_3^{2-}} - C_{\infty, \text{OH}^-} - C_{\infty, \text{HCO}_3^-} - 2C_{\infty, \text{CO}_3^{2-}}} \quad (\text{s6})$$

$$TC = [CO_2] + [HCO_3^-] + [CO_3^{2-}] \quad (s7)$$

$$[CO_2] = \frac{TC[H^+]^2}{[H^+]^2 + K_2[H^+] + K_2K_4} \quad (s8)$$

$$[HCO_3^-] = \frac{TC[H^+]^2}{[H^+]^2 + K_2[H^+] + K_2K_4} \quad (s9)$$

$$[CO_3^{2-}] = \frac{TC[H^+]^2}{[H^+]^2 + K_2[H^+] + K_2K_4} \quad (s10)$$

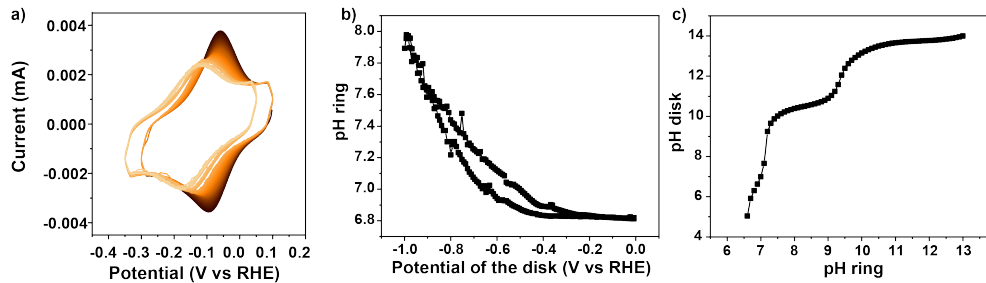


Figure S3. a) Cyclic voltammograms of 4-HATP/4-NSTP modified Au ring electrode during CO₂RR on Au disk electrode in CO₂ saturated 0.1 M NaHCO₃ at 2 mV s⁻¹ and a rotation rate of 2500 rpm. As the disk was cycling from 0 to -1.0 V vs RHE, the CVs on the ring evolved from dark red to light and the peak potentials shifted negatively. b) Variation of interfacial pH at the ring obtained from peak potentials from a) via calibration curve. c) The correspondence between pH_{ring} and pH_{disk} in CO₂ saturated bicarbonates.

Comparison of our RRDE pH sensor and IrO_x

The accuracy and sensitivity of the RRDE pH sensor is highly dependent on the pH-sensitive molecule (or material) present on the ring. Compared with, for example, the recently published IrO_x probe from Tackett and co-workers,⁸ our pH sensor is endowed with higher sensitivity, stability and reproducibility, and wider working range. A direct comparison regarding different properties is given in Table S1 below:

Table S1. Comparison of the pH sensor used by Tackett et al. and in this work:

	This work	Tackett et al. ⁸
pH-sensitive molecule	4-HATP/4-NSTP redox couple	IrO _x
Signal monitored	Current (voltammetric)	Open circuit potential (Potentiometric)
Type of material	Self-assembled monolayer	μm-thick oxide film
Time resolution	4s per data point	120s per data point
Working range	pH 1-13	pH 2-12
Stability	High (no need of reactivation or recalibration)	Dependent on the quality of the IrO _x film ^{9, 10} Possible dissolution in acidic media ¹¹
Reproducibility	High ²	Dependent on the quality of the IrO _x film pH probe needs calibration every day
Sensitivity	0.1 pH unit ²	n.a.

Scan rate dependence experiments in bicarbonate electrolyte

To confirm the equilibrium assumption mentioned above, variations of interfacial pH were recorded with higher scan rates on the disk in CO₂ saturated bicarbonates. As shown in Figure S4a-S4b, the current density increases with scan rate. As a result, accumulation of OH⁻ near the interface of the electrode increases with scan rate, leading to a higher interfacial pH. The interference from current density makes it difficult to distinguish the scan rate effect.

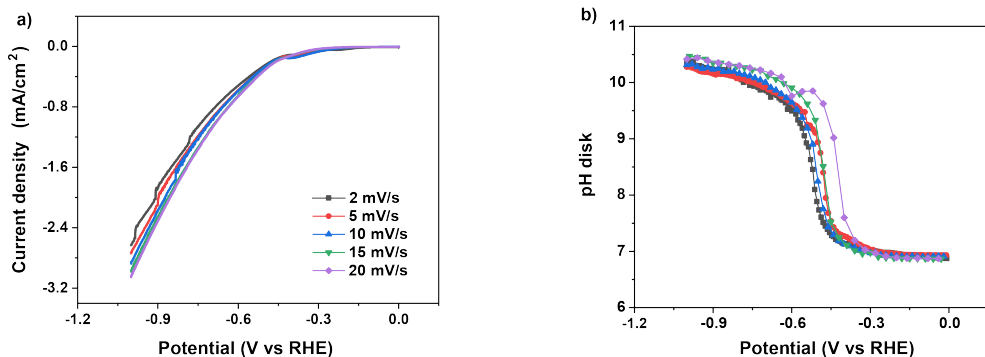


Figure S4. a) Cyclic voltammograms in CO_2 saturated 0.1 M NaHCO_3 at different scan rates. The rotation rate of RRDE is 2500 rpm. b) Variation of the interfacial pH as a function of potential during cyclic voltammetry in figure 4a.

Calculation of theoretical limiting current density and thickness of diffusion layer

The limiting current density for CO_2RR (J_L) and thickness of diffusion layer (δ) is calculated according to the Levich equation:

$$J_L = -0.62nFD^{2/3}\omega^{1/2}v^{-1/6}C^*$$

$$\delta = 1.61D^{1/3}\omega^{-1/2}v^{1/6}$$

where n is the number of electrons transferred, F is the Faraday constant (C mol^{-1}), D is the diffusion coefficient ($\text{cm}^2 \text{ s}^{-1}$), ω is the angular rotation rate (rad s^{-1}), v is the kinematic viscosity ($\text{cm}^2 \text{ s}^{-1}$) and C is the bulk concentration of the reactant (mol cm^{-3}). For CO_2RR , n is equal to 2. The diffusion coefficient D is $1.95 \times 10^{-5} \text{ cm}^2 \text{ s}^{-1}$. The kinematic viscosity of water is $0.0089 \text{ cm}^2 \text{ s}^{-1}$. The angular rotation rate of 2500 RPM corresponds to 261.8 rad s^{-1} . The bulk concentration of CO_2 is 35 mM. The calculated limiting current density is $101.41 \text{ mA cm}^{-2}$. The thickness of diffusion layer is $12.24 \mu\text{m}$.

B

Variation of concentrations of the carbonaceous species

Variation of concentrations of the carbonaceous species is calculated from the interfacial pH monitored under different conditions. According to the results mentioned above, the current density range can be divided into two parts. In the first range ($\log j < -1.0 \text{ mA cm}^{-2}$), the interfacial pH is buffered by $\text{CO}_2/\text{HCO}_3^-$ couple, while in the second range, the

interfacial pH is buffered by $\text{HCO}_3^-/\text{CO}_3^{2-}$ couple. The results show that increasing mass transport, buffer capacity, and the size and the concentration of cation can resist the variation of interfacial pH: exhaustion of CO_2 and accumulation of HCO_3^- in the $\text{CO}_2/\text{HCO}_3^-$

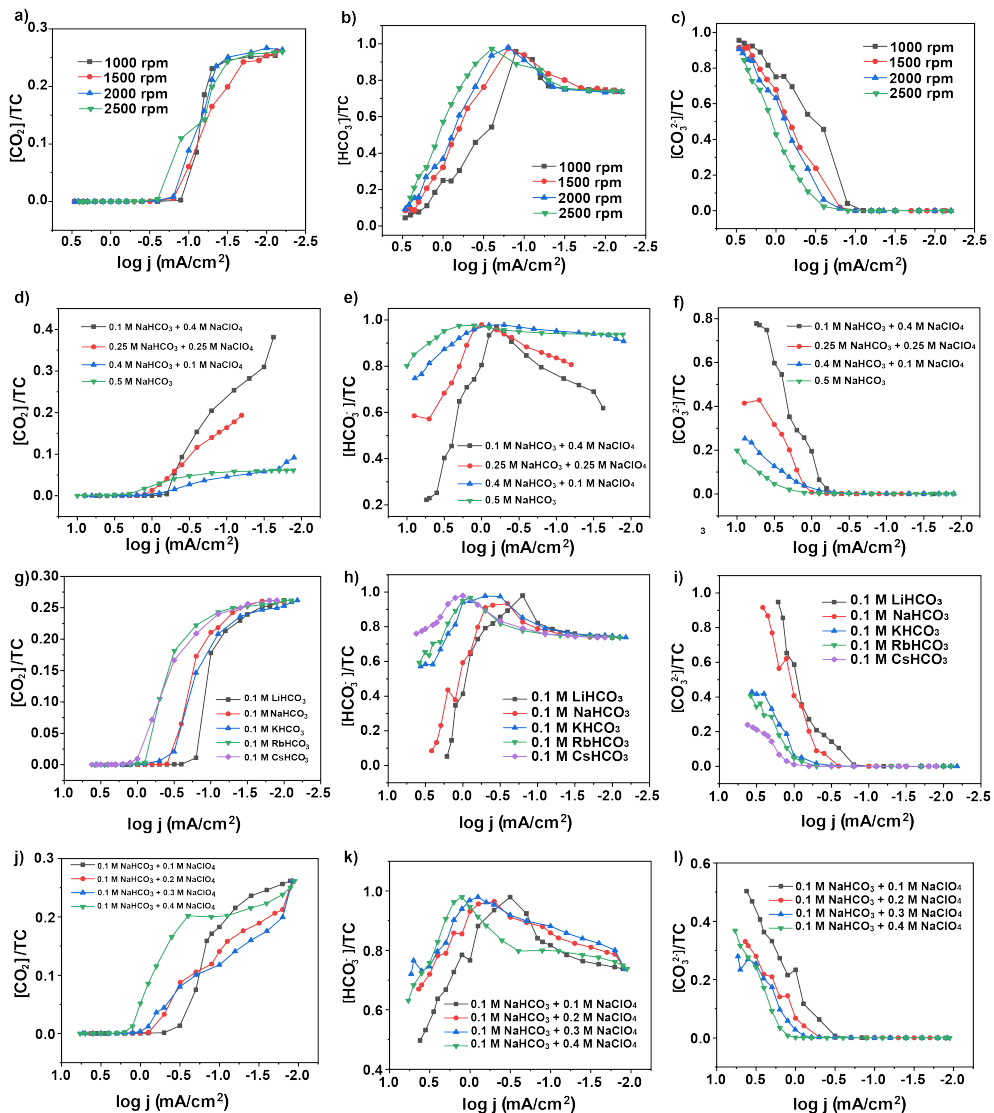
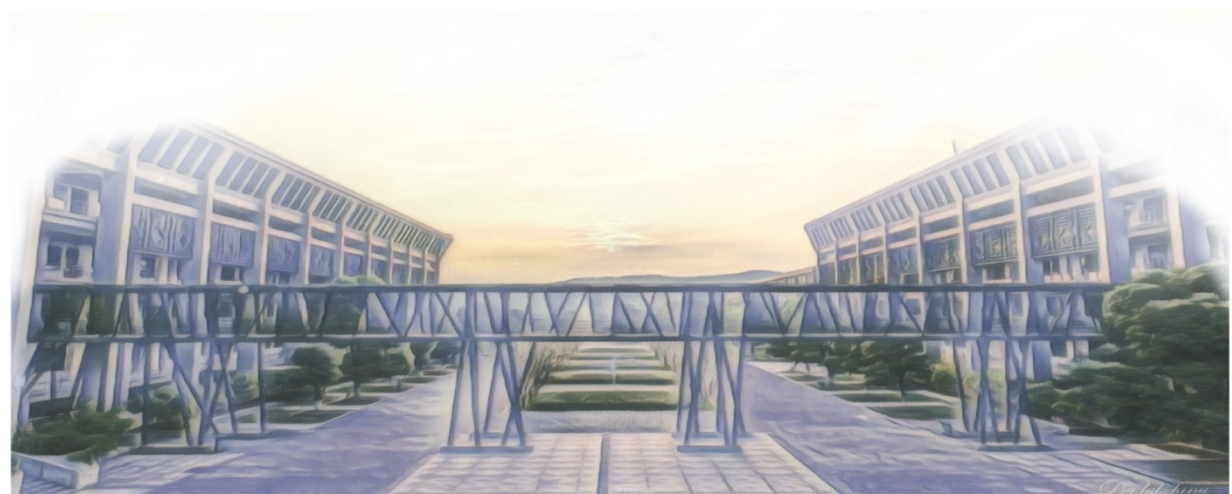


Figure S5. Variation of the interfacial pH as a function of the logarithm of the current density during cyclic voltammetry in (a-c) CO_2 saturated 0.1 M NaHCO_3 with different rotation rates, (d-f) CO_2 saturated bicarbonate with different buffer capacities, (g-i) CO_2 saturated bicarbonate with different cations, and (j-m) CO_2 saturated bicarbonate with different Na^+ concentrations. The buffer range is postponed, and consumption of HCO_3^- and generation of CO_3^{2-} in the HCO_3^-

/CO₃²⁻ buffer range is slowed down as well.

References

- (1) L.-B. Zhao, J.-L. Chen, M. Zhang, D.-Y. Wu and Z.-Q. Tian, *The Journal of Physical Chemistry C*, 2015, **119**, 4949-4958.
- (2) M. C. O. Monteiro, L. Jacobse, T. Touzalin and M. T. M. Koper, *Anal Chem*, 2020, **92**, 2237-2243.
- (3) W. Albery, *Transactions of the Faraday Society*, 1966, **62**, 1915-1919.
- (4) W. J. Albery and E. J. Calvo, *Journal of the Chemical Society, Faraday Transactions 1: Physical Chemistry in Condensed Phases*, 1983, **79**, 2583-2596.
- (5) W. J. Albery and M. L. Hitchman, *Ring-disc Electrodes [by] W.J. Albery and M.L. Hitchman*, Clarendon Press, 1971.
- (6) R. E. Zeebe and D. Wolf-Gladrow, *CO₂ in seawater: equilibrium, kinetics, isotopes*, Gulf Professional Publishing, 2001.
- (7) H. Zhong, K. Fujii, Y. Nakano and F. Jin, *The Journal of Physical Chemistry C*, 2014, **119**, 55-61.
- (8) B. M. Tackett, D. Raciti, N. W. Brady, N. L. Ritzert and T. P. Moffat, *The Journal of Physical Chemistry C*, 2022, **126**, 7456-7467.
- (9) P. Steegstra and E. Ahlberg, *Journal of Electroanalytical Chemistry*, 2012, **685**, 1-7.
- (10) P. Steegstra and E. Ahlberg, *Electrochimica Acta*, 2012, **76**, 26-33.
- (11) P. Jovanović, N. Hodnik, F. Ruiz-Zepeda, I. Arčon, B. Jozinović, M. Zorko, M. Bele, M. Šala, V. S. Šelih and S. Hočevar, *Journal of the American Chemical Society*, 2017, **139**, 12837-12846.



Appendix C

Supporting Information to Chapter 4



Characterization of the Au disk and ring electrode

The Au disk and ring electrode were characterized by cyclic voltammetry in 0.1 M H₂SO₄ respectively, to inspect possible variation of the electrode surface due to the interfacial pH measurements and the dopamine coating. As shown in Figure S1a-b, the CVs before and after dopamine coating on Au ring and disk electrode agree well with each other, signifying that dopamine residue has been totally removed and this coating process hardly influences the surface of Au ring and disk electrode. Figure s1c demonstrates that no discernable changes was traced on the surface of the Au disk during interfacial pH and FE measurements. As the peaks observed in the CVs signify the interplay between Au surface atoms, OH_{ads} and O_{ads} as well as the formation of Au oxide, they are surface sensitive. Each facet exhibits unique peak signatures. Since there is no observable deviation in the CVs, we conclude that the surface structure remains unchanged.

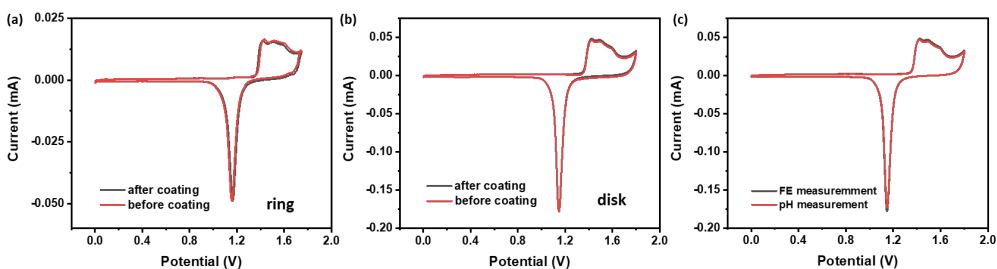


Figure S1. Cyclic voltammograms of **a)** the Au ring and **b)** the Au disk recorded in Ar-saturated 0.1 M H₂SO₄ at 100 mV s⁻¹ before and after the dopamine coating. **c)** Cyclic voltammograms the Au ring and the Au disk recorded in Ar-saturated 0.1 M H₂SO₄ at 100 mV s⁻¹ before the interfacial pH measurement and the FE measurement.

Calculation of the interfacial pH on the disk

Peak potentials of the 4-NSTP/4-HATP redox couple during CO₂RR on the Au disk was recorded. According to the calibration curve of the redox couple (Figure S2a), the interfacial pH on the ring electrode can be obtained. To calculate the interfacial pH on the disk electrode, the relationship between pH on the ring and pH on the disk needs to be figured out. According to the convective-diffusion equation of RRDE, the ratio of the average concentration of products on the ring and the disk is defined to be the detection efficiency N_D as displayed in Eq. s2,¹ where μ is the normalized concentration of products (Eq. s1),

C_∞ is the bulk concentration (The subscript “d” and “r” symbolize the ring and disk electrode, respectively). N_D is determined by the geometry of the electrode (Eqs. s3-4), in which r_1 , r_2 and r_3 are the radii of the disk, the inner ring and the outer ring, respectively.² In this work, the N_D of the RRDE tip employed here ($r_1 = 5.0$ mm, $r_2 = 6.5$ mm, $r_3 = 7.5$ mm) is 0.23.

Besides, the homogenous reactions involving protons or hydroxyl ions also impact the pH gradient between ring and disk electrode. In CO_2 -saturated perchlorate, when the interfacial environment turns alkaline, OH^- generated on the disk is partially consumed by either CO_2 or HCO_3^- on its way to the ring. Also, in CO_2 -saturated electrolyte with protic anions, such as HSO_4^{2-} H_2PO_4^- in this work, the OH^- generated by CO_2R is consumed collectively by the protic anions and CO_2 and HCO_3^- . To avoid an underestimation of the interfacial pH on the disk, influences from the homogeneous buffering reactions (Eqs 2 and 4) need to be compensated.³ For CO_2 -saturated perchlorate, the normalized concentration μ here was redefined as Eq. s5 and the equation for N_D was also modified (Eq. s6). As CO_2 is continuously purged into the electrolyte during the measurements, the total carbon concentration (TC, see Eq. s7), which is the sum of the concentration of the intrinsic bicarbonate electrolyte and the saturated CO_2 concentration from extrinsic bubbling, is supposed to be constant throughout the measurements. Hence the TC for 0.1 M perchlorate under continuous CO_2 bubbling is 0.135. Concentrations of the different carbonaceous species were estimated as a function of pH (Eqs. s8-s10) by combining dissociation equilibrium constants of CO_2 ($\text{pK}_{\text{C}_1} = 6.35$, $\text{pK}_{\text{C}_2} = 10.33$).⁴ As a result, the interfacial pH of the disk electrode was derived from Eqs. S6-S10. The theoretical correlation between the pH on the ring and disk in 0.1 M Sodium perchlorate is plotted in Figure S2b.

$$\mu = (C - C_\infty) / C_\infty \quad (\text{s1})$$

$$N_D = \frac{\mu_r}{\mu_{D,0}} = (C_r - C_\infty) / (C_d - C_\infty) \quad (\text{s2})$$

$$F(\theta) = \frac{\frac{1}{32}}{4\pi} \ln \left(\frac{\left(1 + \theta^{\frac{1}{3}}\right)^3}{1 + \theta} \right) + \frac{3}{2\pi} \tan^{-1} \left(\frac{2\theta^{\frac{1}{3}} - 1}{\sqrt[3]{3^2}} \right) + \frac{1}{4} \quad (\text{s3})$$

$$N_D = 1 - \frac{1}{6} F \left[\left(\frac{r_2}{r_1} \right)^3 - 1 \right] - \frac{2}{3} F \left[\left(\frac{r_2 + r_3}{2r_1} \right)^3 - 1 \right] - \frac{1}{6} F \left[\left(\frac{r_3}{r_1} \right)^3 - 1 \right] \quad (\text{s4})$$

$$\mu_{\text{OH}^-} = \frac{(C_{\text{OH}^-} + C_{\text{HCO}_3^-} + 2C_{\text{CO}_3^{2-}} - C_{\infty, \text{OH}^-} - C_{\infty, \text{HCO}_3^-} - 2C_{\infty, \text{CO}_3^{2-}})}{(C_{\infty, \text{OH}^-} + C_{\infty, \text{HCO}_3^-} + 2C_{\infty, \text{CO}_3^{2-}})} \quad (\text{s5})$$

$$N_D = \frac{\mu_{r, \text{OH}^-}}{\mu_{d, \text{OH}^-}} = \frac{C_{r, \text{OH}^-} + C_{r, \text{HCO}_3^-} + 2C_{r, \text{CO}_3^{2-}} - C_{\infty, \text{OH}^-} - C_{\infty, \text{HCO}_3^-} - 2C_{\infty, \text{CO}_3^{2-}}}{C_{d, \text{OH}^-} + C_{d, \text{HCO}_3^-} + 2C_{d, \text{CO}_3^{2-}} - C_{\infty, \text{OH}^-} - C_{\infty, \text{HCO}_3^-} - 2C_{\infty, \text{CO}_3^{2-}}} \quad (\text{s6})$$

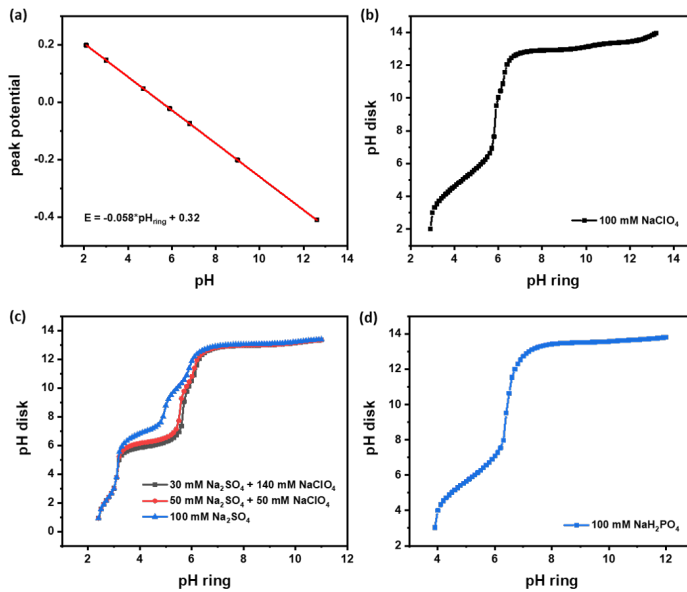


Figure S2. a) Calibration curve of the 4-NSTP/4-HATP redox couple measured in 0.1 M Na₂SO₄, pH is adjusted by adding H₂SO₄ or NaOH. The correspondence between pH_{ring} and pH_{disk} in CO₂-saturated b) 0.1 M NaClO₄ (pH=3), c) Na₂SO₄ with 200 mM Na⁺ and different SO₄²⁻ concentrations (pH=3), and d) 0.1 M NaH₂PO₄ (pH=4).

$$TC = [CO_2] + [HCO_3^-] + [CO_3^{2-}] \quad (s7)$$

$$[CO_2] = \frac{TC[H^+]^2}{[H^+]^2 + K_{c1}[H^+] + K_{c1}K_{c2}} \quad (s8)$$

$$[HCO_3^-] = \frac{TCK_{c1}[H^+]}{[H^+]^2 + K_{c1}[H^+] + K_{c1}K_{c2}} \quad (s9)$$

$$[CO_3^{2-}] = \frac{TCK_{c1}K_{c2}}{[H^+]^2 + K_{c1}[H^+] + K_{c1}K_{c2}} \quad (s10)$$

For CO₂-saturated sulfate, buffering from sulfuric species and carbonate species is compensated, the normalized concentration μ here was redefined as Eq. s11 and the equation for N_D was also modified (Eq. s12). TS is defined as the total concentration of sulfuric species (Eq. s13), and the concentrations of each sulfuric species were estimated as a function of pH (Eqs. s14-s15) by combining dissociation equilibrium constants of HSO₄⁻ (pK_{S1} = 1.99). As a result, the interfacial pH of the disk electrode was derived from Eqs. s12-

s15. The theoretical correlation between the pH on the ring and disk in sodium sulfate with different SO_4^{2-} concentration is plotted in Figure S2c.

$$\mu_{\text{OH}^-} = \frac{(C_{\text{OH}^-} + C_{\text{HCO}_3^-} + 2C_{\text{CO}_3^{2-}} + C_{\text{SO}_4^{2-}} - C_{\infty, \text{OH}^-} - C_{\infty, \text{HCO}_3^-} - 2C_{\infty, \text{CO}_3^{2-}} - C_{\infty, \text{SO}_4^{2-}})}{(C_{\infty, \text{OH}^-} + C_{\infty, \text{HCO}_3^-} + 2C_{\infty, \text{CO}_3^{2-}} + C_{\infty, \text{SO}_4^{2-}})} \quad (\text{s11})$$

$$N_D = \frac{\mu_{\text{r}, \text{OH}^-}}{\mu_{\text{d}, \text{OH}^-}} = \frac{C_{\text{r}, \text{OH}^-} + C_{\text{r}, \text{HCO}_3^-} + 2C_{\text{r}, \text{CO}_3^{2-}} + C_{\text{r}, \text{HSO}_4^-} - C_{\infty, \text{OH}^-} - C_{\infty, \text{HCO}_3^-} - 2C_{\infty, \text{CO}_3^{2-}} - C_{\infty, \text{SO}_4^{2-}}}{C_{\text{d}, \text{OH}^-} + C_{\text{d}, \text{HCO}_3^-} + 2C_{\text{d}, \text{CO}_3^{2-}} + C_{\text{d}, \text{SO}_4^{2-}} - C_{\infty, \text{OH}^-} - C_{\infty, \text{HCO}_3^-} - 2C_{\infty, \text{CO}_3^{2-}} - C_{\infty, \text{SO}_4^{2-}}} \quad (\text{s12})$$

$$\text{TS} = [\text{HSO}_4^-] + [\text{SO}_4^{2-}] \quad (\text{s13})$$

$$[\text{HSO}_4^-] = \frac{\text{TS}[\text{H}^+]}{[\text{H}^+] + K_{\text{S}1}} \quad (\text{s14})$$

$$[\text{SO}_4^{2-}] = \frac{\text{TS}[\text{K}_{\text{S}1}]}{[\text{H}^+] + \text{K}_{\text{S}1}} \quad (\text{s15})$$

Similarly, for CO_2 -saturated phosphate, buffering from phosphate species, carbonate species is compensated, the normalized concentration μ here was redefined as Eq. s16 and the equation for N_D was also modified (Eq. s17). TP is defined as the total concentration of sulfuric species (Eq. s18), and the concentrations of each sulfuric species were estimated as a function of pH (Eqs. s19-s21) by combining dissociation equilibrium constants of H_2PO_4^- ($\text{pK}_{\text{P}1} = 2.14$ $\text{pK}_{\text{P}2} = 7.20$, $\text{pK}_{\text{P}3} = 12.37$). Specially, As the measurements in phosphate is performed at bulk pH 4, H_3PO_4 is ignored because of its extremely small concentration to simplify the calculation. The interfacial pH of the disk electrode was derived from Eqs. S18-s21. The theoretical correlation between the pH on the ring and disk in 0.1 M phosphate is plotted in Figure S2d.

$$\mu_{\text{OH}^-} = \frac{(C_{\text{OH}^-} + C_{\text{HCO}_3^-} + 2C_{\text{CO}_3^{2-}} + C_{\text{HPO}_4^{2-}} + 2C_{\text{PO}_4^{3-}} - C_{\infty, \text{OH}^-} - C_{\infty, \text{HCO}_3^-} - 2C_{\infty, \text{CO}_3^{2-}} - C_{\infty, \text{HPO}_4^{2-}} - 2C_{\infty, \text{PO}_4^{3-}})}{(C_{\infty, \text{OH}^-} + C_{\infty, \text{HCO}_3^-} + 2C_{\infty, \text{CO}_3^{2-}} + C_{\infty, \text{HPO}_4^{2-}} + 2C_{\infty, \text{PO}_4^{3-}})} \quad (\text{s16})$$

$$N_D = \frac{\mu_{\text{r}, \text{OH}^-}}{\mu_{\text{d}, \text{OH}^-}} = \frac{C_{\text{r}, \text{OH}^-} + C_{\text{r}, \text{HCO}_3^-} + 2C_{\text{r}, \text{CO}_3^{2-}} + C_{\text{r}, \text{HPO}_4^{2-}} + 2C_{\text{r}, \text{PO}_4^{3-}} - C_{\infty, \text{OH}^-} - C_{\infty, \text{HCO}_3^-} - 2C_{\infty, \text{CO}_3^{2-}} - C_{\infty, \text{HPO}_4^{2-}} - 2C_{\infty, \text{PO}_4^{3-}}}{C_{\text{d}, \text{OH}^-} + C_{\text{d}, \text{HCO}_3^-} + 2C_{\text{d}, \text{CO}_3^{2-}} + C_{\text{d}, \text{HPO}_4^{2-}} + 2C_{\text{d}, \text{PO}_4^{3-}} - C_{\infty, \text{OH}^-} - C_{\infty, \text{HCO}_3^-} - 2C_{\infty, \text{CO}_3^{2-}} - C_{\infty, \text{HPO}_4^{2-}} - 2C_{\infty, \text{PO}_4^{3-}}} \quad (\text{s17})$$

$$\text{TP} = [\text{H}_2\text{PO}_4^-] + [\text{HPO}_4^{2-}] + [\text{PO}_4^{3-}] \quad (\text{s18})$$

$$[\text{H}_2\text{PO}_4^-] = \frac{\text{TP}[\text{H}^+]^2}{[\text{H}^+]^2 + K_{\text{S}1}[\text{H}^+] + K_{\text{S}1}K_{\text{S}2}} \quad (\text{s19})$$

$$[\text{HPO}_4^{2-}] = \frac{\text{TP}K_{\text{S}1}[\text{H}^+]}{[\text{H}^+]^2 + K_{\text{S}1}[\text{H}^+] + K_{\text{S}1}K_{\text{S}2}} \quad (\text{s20})$$

$$[\text{PO}_4^{3-}] = \frac{\text{TP}K_{\text{S}1}K_{\text{S}2}}{[\text{H}^+]^2 + K_{\text{S}1}[\text{H}^+] + K_{\text{S}1}K_{\text{S}2}} \quad (\text{s21})$$

Ring pH data

Here we show the ring pH data corresponding to Figures 1a, 2a, 3c, 4a, 5b and 6b. The ring pH is markedly dependent on the electrolyte conditions, in agreement with the disk pH data. Noteworthy, as suggested in Figure S3a-b, the ring pH in the mass transport limited region in Na_2SO_4 is higher than that in NaClO_4 (and as a result, the corresponding disk pH is also higher in Na_2SO_4), illustrating the great influence of the current density on corresponding reaction environment during CO2RR. The limiting current density in Na_2SO_4 is higher due to the extra proton flux donated by HSO_4^- , leading to a less acidic reaction environment. Once the ring pH reaches around 6, as shown by the calibration curves in Figure S2, the disk pH rises quickly up to 13, due to the lack of a proper buffer anion and the weak buffer strength of the carbonaceous buffer in the electrolytes.

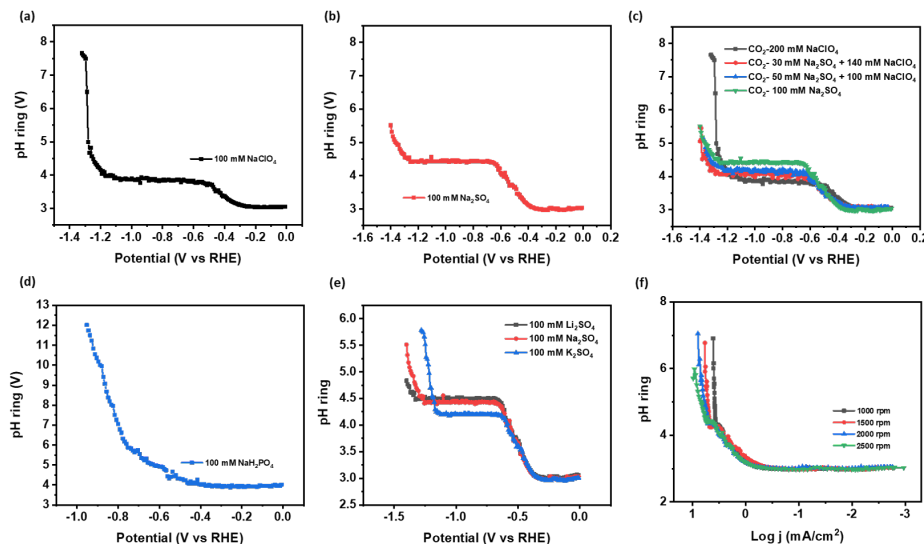


Figure S3. The ring pH data recorded during measurements in a) 0.1 M CO_2 -saturated NaClO_4 with a bulk pH of 3, corresponding to the disk pH data in Figure 1a, b) 0.1 M CO_2 -saturated Na_2SO_4 with a bulk pH of 3, corresponding to the disk pH data in Figure 2a, c) electrolytes with 200 mM Na^+ and different SO_4^{2-} concentrations with a bulk pH of 3, corresponding to the disk pH data in Figure 3c, d) 0.1 M CO_2 -saturated NaH_2PO_4 with a bulk pH of 4, corresponding to the disk pH data in Figure 4a, e) 0.1 M CO_2 -saturated sulfate with different cation identity with a bulk pH of 3 corresponding to the disk pH data in Figure 5b, f) 0.1 M CO_2 -saturated Na_2SO_4 with a bulk pH of 3 with different rotation rates, corresponding to the disk pH data in Figure 6b. The scan rate is 2 mV s⁻¹, and the rotation rate is 2500 rpm unless specially mentioned.

Calculation of Faradaic Efficiency of CO

As a CO-producing metal, Au is also a good catalyst for CO oxidation.⁵ Hence the Au ring electrode can easily deconvolute CO from other products on the disk electrode, since H₂ and CO are the only two products generated on the Au planar electrode. The partial current density for CO2RR on the Au disk can be calculated from the experimental ring current (i_{ring}) and the detect efficiency N of the Au ring (Eq. s22).

$$j_{co} = \frac{i_{ring}}{N * ECSA_{disk}} \quad (s22)$$

The Faradaic efficiency can be calculated by Eq. s23, where the i_{disk} is the current obtained on the disk during experiments.

$$FE_{co} = \frac{i_{ring}}{N * |i_{disk}|} * 100\% \quad (s23)$$

The partial current density and Faradaic efficiency of HER can be determined from Eq. s23-24

$$j_{H_2} = j_{tot} - j_{co} \quad (s24)$$

$$FE_{H_2} = 100\% - FE_{co} \quad (s25)$$

As mentioned in the experimental section, after finishing FE and interfacial pH measurements, the collection efficiency N was measured in 5 mM K₃Fe(CN)₆ dissolved in 0.1 M NaHCO₃, during which the disk was cycled from 0.27 to 1.27 V vs RHE, while the ring potential was set to 0.96 V vs RHE. The collection efficiency was determined for each rotation rate and was calculated according to Eq. s26.

$$N = \left| \frac{i_{ring}}{i_{disk}} \right| \quad (s26)$$

FE measurements during chronoamperometry

To confirm the stability of the Au ring CO sensor, FE measurements during chronoamperometry were conducted in 0.1 M CO₂-saturated Na₂SO₄, where CO2RR on the disk electrode is turned “on” and “off” at different potentials from -0.3 V to -1.4 V vs RHE every 200s. The rotation rate of RRDE is 2500 rpm. As depicted in Figure S4, the results agree well with the ones during cyclic voltammetry in Figure 2. FE of CO2RR increases up to ~60% along the mass transport-limited region (from -0.6V ~ -1.2 V), and starts to decay once the water reduction sets in. During steady-state electrolysis, the ring current stays stable.

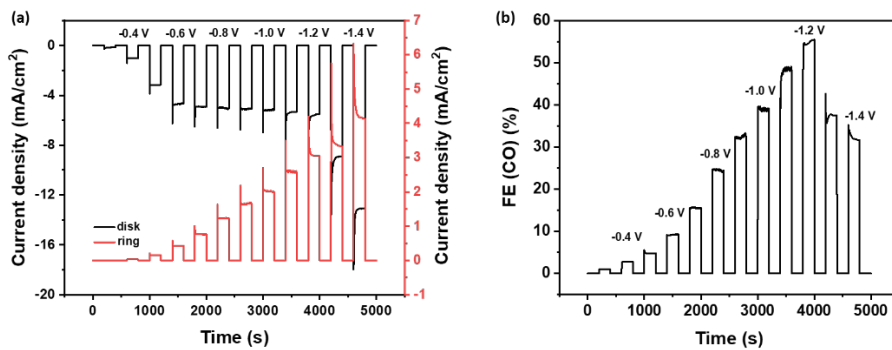
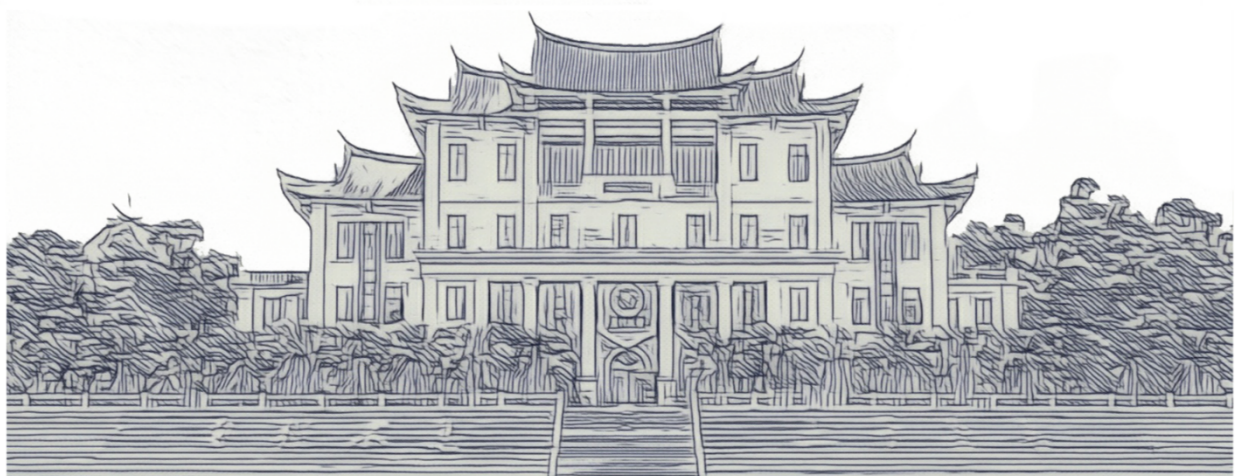


Figure S4. **a)** Current density on the disk (black curve) and ring (black curve) and **b)** FE of CO during chronoamperometry in 0.1 M CO₂-saturated Na₂SO₄ (pH=3).

Reference

- (1)Albery, W., Ring-disc electrodes. Part 1.—A new approach to the theory. *Transactions of the Faraday Society* **1966**, *62*, 1915-1919.
- (2)Albery, W. J.; Calvo, E. J., Ring-disc electrodes. Part 21.—pH measurement with the ring. *Journal of the Chemical Society, Faraday Transactions 1: Physical Chemistry in Condensed Phases* **1983**, *79* (11), 2583-2596.
- (3)Zeebe, R. E.; Wolf-Gladrow, D., *CO₂ in seawater: equilibrium, kinetics, isotopes*. Gulf Professional Publishing: 2001.
- (4)Zhong, H.; Fujii, K.; Nakano, Y.; Jin, F., Effect of CO₂ Bubbling into Aqueous Solutions Used for Electrochemical Reduction of CO₂ for Energy Conversion and Storage. *The Journal of Physical Chemistry C* **2014**, *119* (1), 55-61.
- (5)Monteiro, M. C. O.; Jacobse, L.; Koper, M. T. M., Understanding the Voltammetry of Bulk CO Electrooxidation in Neutral Media through Combined SECM Measurements. *J Phys Chem Lett* **2020**, *11* (22), 9708-9713.
- (6)Blizanac, B. B.; Arenz, M.; Ross, P. N.; Marković, N. M., Surface Electrochemistry of CO on Reconstructed Gold Single Crystal Surfaces Studied by Infrared Reflection Absorption Spectroscopy and Rotating Disk Electrode. *J. Am. Chem. Soc.* **2004**, *126* (32), 10130-10141.



Appendix D

Supporting Information to Chapter 5



Bulk pH of the electrolytes employed in the quantitative analysis

Table 1 Bulk pH of electrolytes employed in measurements of Figure 3

Electrolyte	Bulk pH
100 mM LiClO ₄ + 0 mM Li ₂ SO ₄	3.964
95 mM LiClO ₄ + 5 mM Li ₂ SO ₄	3.964
85 mM LiClO ₄ + 15 mM Li ₂ SO ₄	3.967
70 mM LiClO ₄ + 30 mM Li ₂ SO ₄	3.964
55 mM LiClO ₄ + 45 mM Li ₂ SO ₄	3.964
40 mM LiClO ₄ + 60 mM Li ₂ SO ₄	3.957
25 mM LiClO ₄ + 75 mM Li ₂ SO ₄	3.964
0 mM LiClO ₄ + 100 mM Li ₂ SO ₄	3.960

Table 2 Bulk pH of electrolytes employed in measurements of Figure 4

Electrolyte	Bulk pH
100 mM LiClO ₄ + 0 mM KClO ₄	3.955
95 mM LiClO ₄ + 5 mM KClO ₄	3.948
85 mM LiClO ₄ + 15 mM KClO ₄	3.950
70 mM LiClO ₄ + 30 mM KClO ₄	3.965
55 mM LiClO ₄ + 45 mM KClO ₄	3.948
40 mM LiClO ₄ + 60 mM KClO ₄	3.954
25 mM LiClO ₄ + 75 mM KClO ₄	3.948

Table 3 Bulk pH of electrolytes employed in measurements of Figure 5

Electrolyte	Bulk pH
100 mM LiClO ₄ + 0 mM CsClO ₄	3.951
95 mM LiClO ₄ + 5 mM CsClO ₄	3.949
85 mM LiClO ₄ + 15 mM CsClO ₄	3.944
70 mM LiClO ₄ + 30 mM CsClO ₄	3.940
55 mM LiClO ₄ + 45 mM CsClO ₄	3.943
40 mM LiClO ₄ + 60 mM CsClO ₄	3.943
25 mM LiClO ₄ + 75 mM CsClO ₄	3.948

Table 4 Bulk pH of electrolytes employed in measurements of Figure 6

Electrolyte	Bulk pH
100 mM Li ₂ SO ₄ + 0 mM K ₂ SO ₄	3.954
95 mM Li ₂ SO ₄ + 5 mM K ₂ SO ₄	3.949
85 mM Li ₂ SO ₄ + 15 mM K ₂ SO ₄	3.955
70 mM Li ₂ SO ₄ + 30 mM K ₂ SO ₄	3.958
55 mM Li ₂ SO ₄ + 45 mM K ₂ SO ₄	3.952
40 mM Li ₂ SO ₄ + 60 mM K ₂ SO ₄	3.953
25 mM Li ₂ SO ₄ + 75 mM K ₂ SO ₄	3.954

Table 5 Bulk pH of electrolytes employed in measurements of Figure 7

Electrolyte	Bulk pH
100 mM Li ₂ SO ₄ + 0 mM Cs ₂ SO ₄	3.961
95 mM Li ₂ SO ₄ + 5 mM Cs ₂ SO ₄	3.953
85 mM Li ₂ SO ₄ + 15 mM Cs ₂ SO ₄	3.965
70 mM Li ₂ SO ₄ + 30 mM Cs ₂ SO ₄	3.959
55 mM Li ₂ SO ₄ + 45 mM Cs ₂ SO ₄	3.960
40 mM Li ₂ SO ₄ + 60 mM Cs ₂ SO ₄	3.965
25 mM Li ₂ SO ₄ + 75 mM Cs ₂ SO ₄	3.962

Table 6 Bulk pH of electrolytes employed in measurements of Figure S7a

Electrolyte	Bulk pH
100 mM LiClO ₄ + 0 mM NaClO ₄	3.960
95 mM LiClO ₄ + 5 mM NaClO ₄	3.960
85 mM LiClO ₄ + 15 mM NaClO ₄	3.967
70 mM LiClO ₄ + 30 mM NaClO ₄	3.965
55 mM LiClO ₄ + 45 mM NaClO ₄	3.961
40 mM LiClO ₄ + 60 mM NaClO ₄	3.969
25 mM LiClO ₄ + 75 mM NaClO ₄	3.961

Table 7 Bulk pH of electrolytes employed in measurements of Figure S7b-d

Electrolyte	Bulk pH
100 mM Li ₂ SO ₄ + 0 mM Na ₂ SO ₄	3.954
95 mM Li ₂ SO ₄ + 5 mM Na ₂ SO ₄	3.955
85 mM Li ₂ SO ₄ + 15 mM Na ₂ SO ₄	3.951
70 mM Li ₂ SO ₄ + 30 mM Na ₂ SO ₄	3.957
55 mM Li ₂ SO ₄ + 45 mM Na ₂ SO ₄	3.968
40 mM Li ₂ SO ₄ + 60 mM Na ₂ SO ₄	3.963
25 mM Li ₂ SO ₄ + 75 mM Na ₂ SO ₄	3.970

Table 8 Bulk pH of electrolytes employed in measurements of Figure S8-9

Electrolyte	Bulk pH
100 mM Li ₂ SO ₄ + 0 mM Na ₂ SO ₄	3.701
95 mM Li ₂ SO ₄ + 5 mM Na ₂ SO ₄	3.705
85 mM Li ₂ SO ₄ + 15 mM Na ₂ SO ₄	3.695
70 mM Li ₂ SO ₄ + 30 mM Na ₂ SO ₄	3.699
55 mM Li ₂ SO ₄ + 45 mM Na ₂ SO ₄	3.698
40 mM Li ₂ SO ₄ + 60 mM Na ₂ SO ₄	3.703
25 mM Li ₂ SO ₄ + 75 mM Na ₂ SO ₄	3.700

A quantitative analysis of the steady-state behavior of HER coupled with pre-chemical processes

Dating back to the pioneering work by Koutecký and Levich in 1958,¹ extensive efforts have been devoted to evaluating the current response of steady-state HER when coupled to a pre-chemical process.²⁻⁴ Rebouillat et al⁵ developed a mathematical analysis for different rate-limiting scenarios, dependent on the competition between the chemical reaction kinetics and diffusion. According to our measurements, the steady-state behavior under our conditions belongs to their “DM” regime, where the reaction rate is still controlled by diffusion but modified by the chemical process, in our case the dissociation of HSO₄⁻ and hydrolysis of K⁺ and Cs⁺. The current response is evaluated through Eq. s1,

$$\frac{1}{i} = \frac{\omega^{-1/2}}{0.62nFAD_{HA}^{2/3}v^{-1/6}KC_{\Sigma}} \quad (s1)$$

where *n* is the number of electrons transferred, *F* is the Faraday constant (C mol⁻¹), *D_{HA}* is the diffusion coefficient of the electroinert species (cm² s⁻¹), *ω* is the angular rotation

rate (rad s^{-1}), ν is the kinematic viscosity ($\text{cm}^2 \text{ s}^{-1}$), K is the dissociation constant of the proton donor and C_{Σ} is the total concentration of the proton donor.

To account for the influence of the bulk proton concentration, which is relevant in our case, an additional current from the bulk protons is introduced in Eq. s2,

$$\frac{1}{i} = \frac{\omega^{-1/2}}{0.62nFAD_{HA}^{2/3}\nu^{-1/6}KC_{\Sigma} + 0.62nFAD_H^{2/3}\nu^{-1/6}C_H} \quad (\text{s2})$$

where D_H is the diffusion coefficient of the proton ($\text{cm}^2 \text{ s}^{-1}$) and C_H is the bulk concentration of the proton (mol cm^{-3}). This implies a linear relationship between inverse limiting current density and the inverse square root of rotation speed with a Koutechy-Levich Slope (Eq. s3, referred to as “ S_{K-L} ” in the following text).

$$S_{K-L}^{-1} = 0.62nFAD_{HA}^{2/3}\nu^{-1/6}KC_{\Sigma} + 0.62nFAD_H^{2/3}\nu^{-1/6}C_H \quad (\text{s3})$$

The inverse S_{K-L} is linearly dependent the concentration of the electroinactive species, from which the corresponding acid-base constant K can be evaluated.

In case both anionic and cationic proton donors are present, a third term needs to be introduced in the analysis to account for both the influence of the alkali cation and of HSO_4^- (Eqs. s4-5),

$$\frac{1}{i} = \frac{\omega^{-1/2}}{0.62nFAD_{cat}^{2/3}\nu^{-1/6}K_{cat}C_{cat} + 0.62nFAD_{HSO_4^-}^{2/3}\nu^{-1/6}K_{HSO_4^-}C_{(H)SO_4^-} + 0.62nFAD_H^{2/3}\nu^{-1/6}C_H} \quad (\text{s4})$$

$$S_{K-L}^{-1} = 0.62nFAD_{cat}^{2/3}\nu^{-1/6}K_{cat}C_{cat} + 0.62nFAD_H^{2/3}\nu^{-1/6}C_H + 0.62nFAD_{HSO_4^-}^{2/3}\nu^{-1/6}K_{HSO_4^-}C_{(H)SO_4^-} \quad (\text{s5})$$

where $D_{HSO_4^-}$ is the diffusion coefficient of HSO_4^- ($\text{cm}^2 \text{ s}^{-1}$) and $D_{HSO_4^-}$ is the bulk concentration of HSO_4^- (mol cm^{-3}). Similarly, the inverse S_{K-L} here is linearly dependent on the concentration of the electroinactive species, from which the K 's of both the cation and the $D_{HSO_4^-}$ can be evaluated.

The polarization curves recorded in different electrolyte conditions with rotation rates from 900 rpm to 2500 rpm are shown in Figure S1-7. For HER, n is equal to 1 per proton. The Faraday constant is 96485 C mol^{-1} . The diffusion coefficients of $D_{HSO_4^-}$, D_{K^+} and D_{Cs^+} are $1.385 \times 10^{-5} \text{ cm}^2 \text{ s}^{-1}$, $1.957 \times 10^{-5} \text{ cm}^2 \text{ s}^{-1}$, $2.056 \times 10^{-5} \text{ cm}^2 \text{ s}^{-1}$.⁶ The kinematic viscosity of water is $0.0089 \text{ cm}^2 \text{ s}^{-1}$.

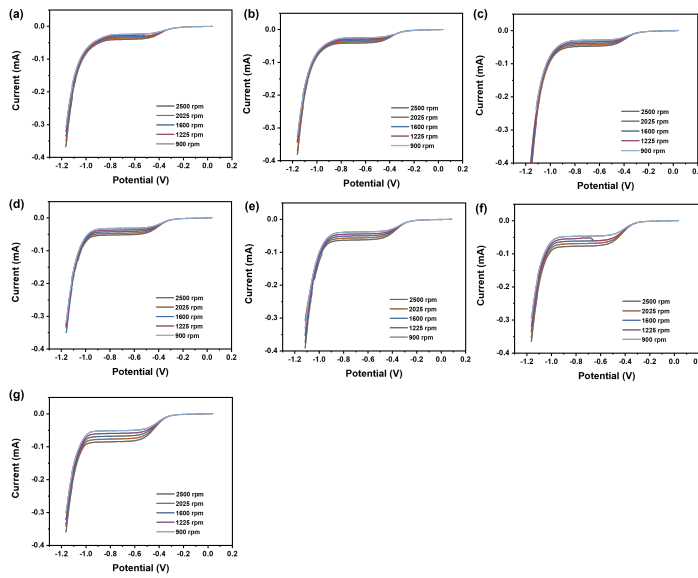


Figure S1. a-g) Polarization curves recorded on a Au RDE at 10 mV s^{-1} with rotation rates from 900 rpm to 2500 rpm at a bulk pH of 4 in Ar-saturated 0 mM, 5 mM, 15 mM, 30 mM, 45 mM, 60 mM, 75 mM Li_2SO_4 respectively, LiClO_4 was added to adjust the ionic strength.

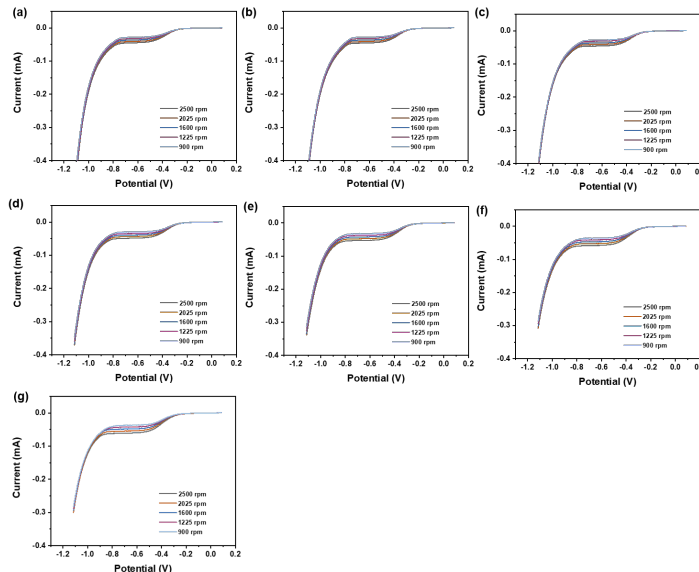


Figure S2. a-g) Polarization curves recorded on a Au RDE at 10 mV s^{-1} with rotation rates from 900 rpm to 2500 rpm at a bulk pH of 4 in Ar-saturated 0 mM, 5 mM, 15 mM, 30 mM, 45 mM, 60 mM, 75 mM KClO_4 respectively, LiClO_4 was added to adjust the ionic strength.

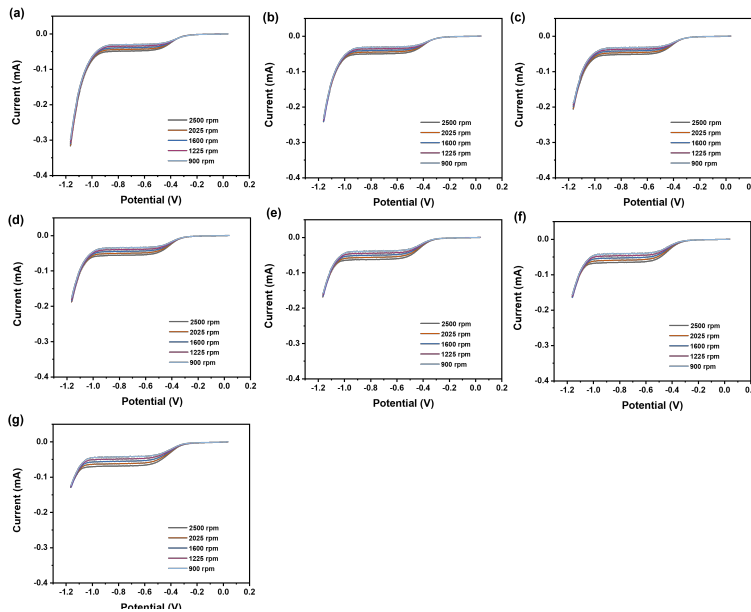


Figure S3. a-g) Polarization curves recorded on a Au RDE at 10 mV s^{-1} with rotation rates from 900 rpm to 2500 rpm at a bulk pH of 4 in Ar-saturated 0 mM, 5 mM, 15 mM, 30 mM, 45 mM, 60 mM, 75 mM CsClO_4 respectively, LiClO_4 was added to adjust the ionic strength.

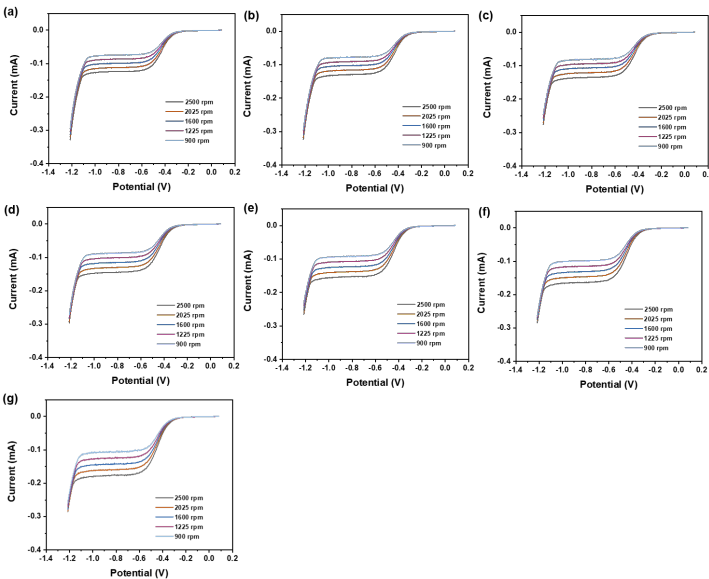


Figure S4. a-g) Polarization curves recorded on a Au RDE at 10 mV s^{-1} with rotation rates from 900 rpm to 2500 rpm at a bulk pH of 4 in Ar-saturated 0 mM, 5 mM, 15 mM, 30 mM, 45 mM, 60 mM, 75 mM K_2SO_4 respectively, Li_2SO_4 was added to adjust the ionic strength.

D

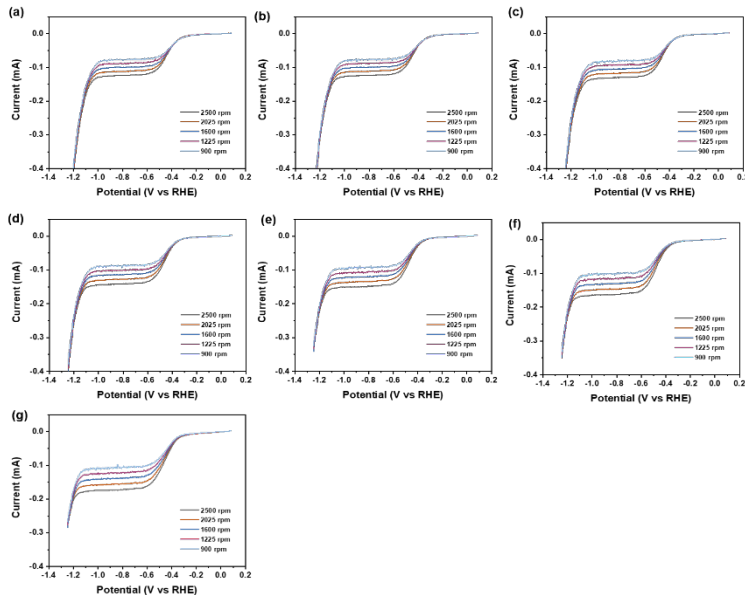


Figure S5. a-g) Polarization curves recorded on a Au RDE at 10 mV s^{-1} with rotation rates from 900 rpm to 2500 rpm at a bulk pH of 4 in Ar-saturated 0 mM, 5 mM, 15 mM, 30 mM, 45 mM, 60 mM, 75 mM Cs_2SO_4 respectively, Li_2SO_4 was added to adjust the ionic strength.

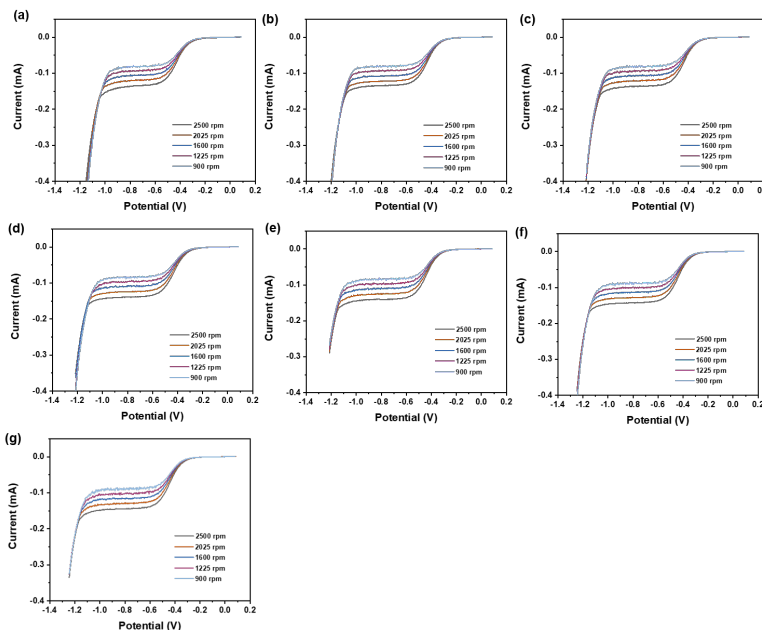


Figure S6. a-g) Polarization curves recorded on a Au RDE at 10 mV s^{-1} with rotation rates from 900 rpm to 2500 rpm at a bulk pH of 4 in Ar-saturated 0 mM, 5 mM, 15 mM, 30 mM, 45 mM, 60 mM, 75 mM Na_2SO_4 respectively, Li_2SO_4 was added to adjust the ionic strength.

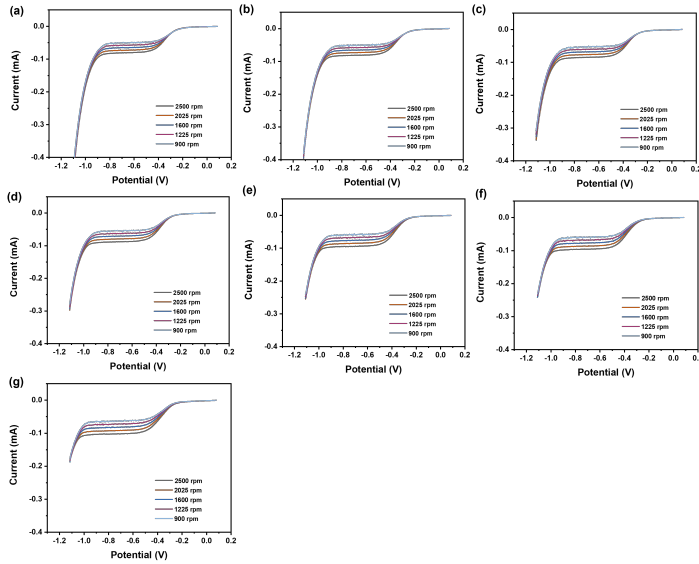


Figure S7. a-g) Polarization curves recorded on a Au RDE at 10 mV s^{-1} with rotation rates from 900 rpm to 2500 rpm at a bulk pH of 3.7 in Ar-saturated 0 mM, 5 mM, 15 mM, 30 mM, 45 mM, 60 mM, 75 mM CsClO_4 respectively, LiClO_4 was added to adjust the ionic strength.

The effect of Na^+ on the steady-state behavior of HER

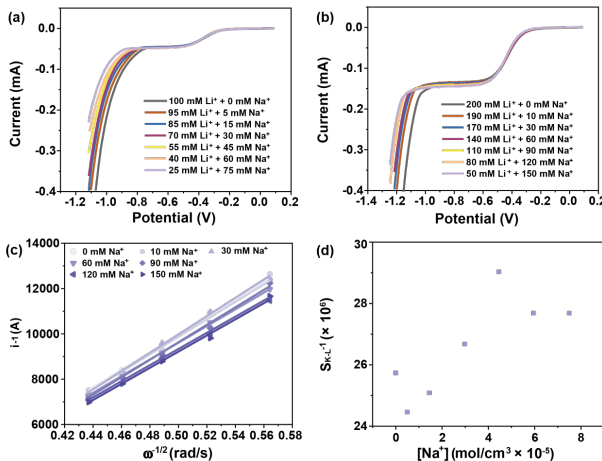


Figure S8. a) Polarization curves recorded on a Au RDE in Ar-saturated 100 mM sulfate electrolytes with different ratios of cation concentrations, with a bulk pH of 4, at 10 mV s^{-1} and a rotation rate of 2500 rpm. b) Polarization curves recorded on a Au RDE in Ar-saturated 100 mM perchlorate electrolytes with different ratios of cation concentrations, with a bulk pH of 4, at 10 mV s^{-1} and a rotation rate of 2500 rpm. c) Koutecky-Levich plots under different electrolyte conditions from a with the rotation rates ranging from 900 rpm to 2500 rpm. d) The correspondence between the S_{KL}^{-1} and the Na^+ concentration from b).

A quantitative analysis at bulk pH of 3.7

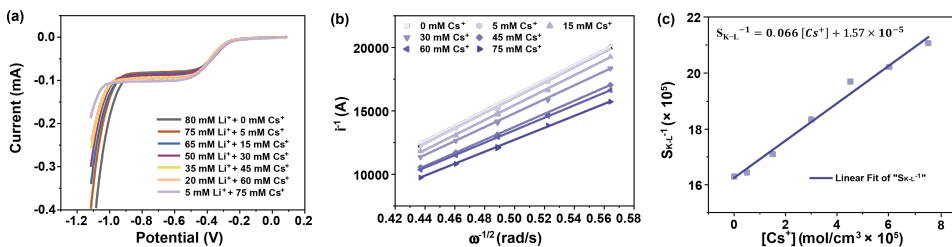
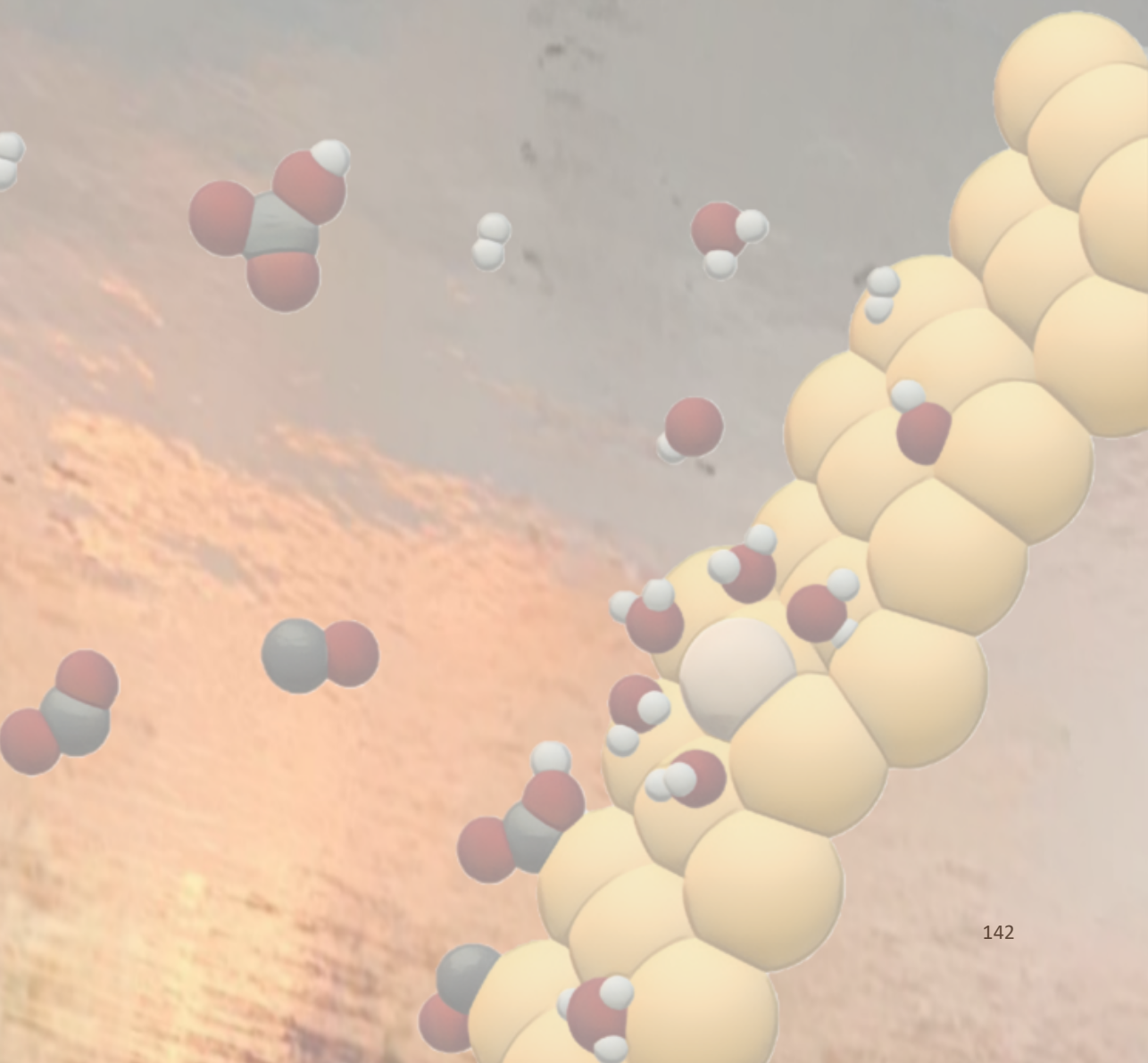


Figure S9. a) Polarization curves recorded on a Au RDE in Ar-saturated 100 mM perchlorate electrolytes with different ratios of cation concentrations, with a bulk pH of 3.7, at 10 mV s⁻¹ and a rotation rate of 2500 rpm. b) Koutecký-Levich plots under different electrolyte conditions from a) with the rotation rates ranging from 900 rpm to 2500 rpm c) The correspondence between the S_{KL}^{-1} and the K^+ concentration from b) and its linear fit.

Reference

- (1) Koutecký, J.; Levich, V., The use of a rotating disk electrode in the studies of electrochemical kinetics and electrolytic processes. *Zh. Fiz. Khim.* **1958**, 32, 1565-1575.
- (2) Dogonadze, R., Use of Rotating Disk Electrode in the Study of the Electrochemical Kinetic and Catalytic Processes. The Case of Different Diffusion Coefficients. *Zh. Fiz. Khim.* **1958**, 32, 2437-2442.
- (3) Treimer, S.; Tang, A.; Johnson, D. C., A Consideration of the application of Koutecký-Levich plots in the diagnoses of charge-transfer mechanisms at rotated disk electrodes. *Electroanalysis* **2002**, 14 (3), 165-171.
- (4) Leal, P.; Leite, N.; Viana, P.; de Sousa, F.; Barcia, O.; Mattos, O., Numerical analysis of the steady-state behavior of CE processes in rotating disk electrode systems. *Journal of The Electrochemical Society* **2018**, 165 (9), H466.
- (5) Rebouillat, S.; Lyons, M. E. G.; Bannon, T., Evaluation of the proton transfer kinetics of potential electrolytes in non-aqueous solutions using electrochemical techniques Part 1. Kinetic analysis of the general CE mechanism at stationary and rotating electrodes. *J. Solid State Electrochem.* **1999**, 3 (4), 215-230.
- (6) Lide, D. R., *CRC handbook of chemistry and physics*. CRC press: 2004; Vol. 85.





Summary

The role of the interfacial environment during electrochemical reactions has been increasingly valued, especially for those reactions involving protons or hydroxyl ions. The acid-base equilibria of the weak proton donors in the bulk electrolyte, namely the protic anions and the weakly hydrated cations, implicitly modify the interfacial environment and impact the rate and selectivity of electrochemical reactions. Therefore, the interfacial pH is key to unveil the electrolyte effects. In this thesis, we devised an in-situ interfacial pH sensor and visualized the evolution of interfacial pH during the electroreduction of CO₂ to CO and H₂ evolution. We found that the reaction activity and competition between CO₂ electroreduction to CO and H₂ evolution is highly dependent on interfacial pH, which can be readily tuned by modulating the interfacial environment *via* various electrolyte species.

Coupled with the highly sensitive voltammetric 4-hydroxylaminothiophenol/4-nitrosothiophenol (4-HATP/4-NSTP) pH sensing redox couple, the Au ring of the RRDE can be used as a robust in-situ pH meter under well-defined mass transport conditions. In **Chapter 2**, the RRDE pH sensor is proved to be capable of recording the interfacial pH during electrode reactions on the Au disk over a wide pH range, without imposing further interference to the reactions. We showed that the interfacial pH during the H₂ evolution was influenced by the potential, or more precisely the current density drawn, the rotation rate, and the buffer capacity. The RRDE setup quantifies how a more negative potential and a larger current density lead to the increase of interfacial pH, while a higher rotation rate and a larger buffer capability suppress it.

As for the CO₂ reduction, the situation is different due to the buffering of CO₂ and HCO₃⁻. **Chapter 3** demonstrated that two pH regimes appear with increasing polarization during CO₂ reduction. The interfacial pH stabilizes at around 7 due to the buffering of CO₂ at a less negative potential and jumps to 9 as the interfacial CO₂ concentration decays and HCO₃⁻ starts to buffer. This also leads to the decay of CO₂ electroreduction and the enhancement of the competing water reduction. The interfacial environment is modified by changes in mass transport and buffer capacity. Also the size and concentration of the cation can suppress the rise in the interfacial pH. The results showed that the anion buffer has the largest effect, while the mass transport and the cations are not as efficient in resisting interfacial pH changes. In fact, increasing mass transport by changing the disk rotation rate appears to be the least effective, as the interfacial pH is still as high as 11 under strong forced convection (2500 rpm). Importantly, increasing buffer or cation concentration might not assist in CO₂ electroreduction, since the competing HER is typically more enhanced by that than the CO₂ electroreduction.

To maintain the interfacial CO_2 concentration, in **Chapter 4**, the CO_2 electroreduction was conducted under mildly acidic electrolyte conditions (at pH 3). We proved that the CO_2 electroreduction outcompetes the proton reduction and increases along the proton mass transport-limited current plateau under a near-neutral interfacial environment, which is attributed to the consumption of the protons by the hydroxyl ion generated by the CO_2 electroreduction. However, when the water reduction regime sets in, the local alkaline environment leads to extra consumption of CO_2 by the hydroxyl ion. Besides, the reaction selectivity towards CO_2 electroreduction can be further improved by tuning the interfacial environment *via* the anion effect, cation effect, and mass transport effect. A proper protic anion such as HSO_4^- can add extra proton flux *via* the acid-base equilibria to maintain the environment to be nearly neutral. In an acidic environment, a weakly hydrated cation such as K^+ accelerates the CO2RR while barely impacting the competing proton reduction, whereas decreasing the mass transport suppresses the proton reduction, leading to a higher selectivity of the CO2RR.

The investigation of the effects of these supporting electrolyte species on H_2 evolution was continued in **Chapter 5**. We observed that the steady-state current of H_2 evolution appreciably increases with the concentration of the protic anion, namely HSO_4^- and the weakly hydrated alkali cations (K^+ and Cs^+). This enhancement is attributed to the coupling of proton reduction with the homogeneous acid-base equilibria, namely, the dissociation of HSO_4^- and hydrolysis of K^+ and Cs^+ . This confirmed the buffering capability of the alkali cation species and their implicit role as a weak proton donor, which can be observed and quantified experimentally using RDE. Quantitative studies elucidated the H_2 evolution in this case as a mass transport limited process coupled to a chemical reaction (i.e. the acid-base reaction). Moreover, the linear relationship between the concentration of electro-inactive species and the Koutecký-Levich slope was observed, from which the pK_a of the proton donor involved can be extracted. The corresponding pK_a 's of HSO_4^- , K^+ , and Cs^+ were determined to be 2.06, 2.52, and 2.48, respectively.

Samenvatting

Het blootleggen van de elektrolyteffecten van CO₂-elektroreductie tot CO en H₂-evolutie vanuit het perspectief van de grensvlak pH.

De rol van het grensvlakmilieu tijdens elektrochemische reacties wordt steeds belangrijker, vooral voor reacties waarbij protonen of hydroxyde ionen betrokken zijn. De zuur-base evenwichten van de zwakke proton donoren in de bulk elektrolyt, namelijk de protische anionen en de zwak gehydrateerde kationen, wijzigen impliciet het grensvlakmilieu en beïnvloeden de snelheid en selectiviteit van elektrochemische reacties. Daarom is de grensvlak pH de sleutel tot het onthullen van de elektrolytische effecten. In dit proefschrift ontwikkelden we een in-situ grensvlak pH-sensor en visualiseerden we de evolutie van de grensvlak pH tijdens de elektroreductie van CO₂ tot CO en H₂ evolutie. We ontdekten dat de reactieactiviteit en competitie tussen CO₂ elektroreductie tot CO en H₂ evolutie sterk afhankelijk is van de grensvlak pH, die gemakkelijk kan worden afgestemd door het grensvlakmilieu te moduleren *via* verschillende soorten elektrolyt.

Gekoppeld aan het zeer gevoelige voltammetrische 4-hydroxylaminothiophenol/4-nitrosothiophenol (4-HATP/4-NSTP) pH detecterende redoxkoppel, kan de Au ring van de RRDE gebruikt worden als een robuuste in-situ pH meter onder goed gedefinieerde massatransportcondities. In **Hoofdstuk 2** werd aangetoond dat de RRDE pH-sensor in staat is om de grensvlak pH tijdens oppervlakte reacties op de Au-schijf over een breed pH-bereik te registreren, zonder verdere interferentie met de reacties. We toonden aan dat de grensvlak pH tijdens de H₂ evolutie beïnvloed werd door de potentiaal, of nauwkeuriger gezegd de getrokken stroomdichtheid, de rotatiesnelheid en de buffercapaciteit. De RRDE-opstelling kwantificeert hoe een negatievere potentiaal en een grotere stroomdichtheid leiden tot een toename van de grensvlak pH, terwijl een hogere rotatiesnelheid en een grotere buffercapaciteit dit onderdrukken.

Voor de CO₂ reductie is de situatie anders door de buffering van CO₂ en HCO₃⁻. **Hoofdstuk 3** toonde aan dat er twee pH-regimes ontstaan met toenemende polarisatie tijdens de CO₂ reductie. De grensvlak pH stabiliseert rond 7 door de buffering van CO₂ bij een minder negatief potentiaal en springt naar 9 als de grensvlak CO₂ concentratie afneemt en HCO₃⁻ begint te bufferen. Dit leidt ook tot de achteruitgang van CO₂ elektroreductie en de versterking van de concurrerende waterreductie. Het grensvlakmilieu wordt gewijzigd door veranderingen in massatransport en buffercapaciteit. Ook de grootte en concentratie van het kation kunnen de stijging van de grensvlak pH onderdrukken. De resultaten toonden aan dat de anionbuffer het grootste effect heeft, terwijl het massatransport en de kationen niet zo efficiënt zijn in het weerstaan van grensvlak pH-veranderingen. In feite blijkt het

verhogen van het massatransport door de rotatiesnelheid van de schijf te veranderen het minst effectief, aangezien de grensvlak pH nog steeds 11 is onder sterke geforceerde convectie (2500 rpm). Belangrijk is dat het verhogen van de buffer- of kationconcentratie mogelijk niet helpt bij de elektroreductie van CO₂, omdat de concurrerende HER daardoor meestal sterker wordt dan de CO₂ elektroreductie.

Om de grensvlak CO₂ concentratie te handhaven, werd in **Hoofdstuk 4** de CO₂ elektroreductie uitgevoerd onder licht zure elektrolytomstandigheden (bij pH 3). We toonden aan dat de CO₂ elektroreductie de protonreductie overtroeft en toeneemt langs het protonmassatransport gelimiteerde stroomplateau onder een bijna neutrale grensvlak omgeving, wat wordt toegeschreven aan het verbruik van protonen door het hydroxyde ion dat wordt gegenereerd door de CO₂ elektroreductie. Wanneer echter het waterreductieregime begint, leidt het lokale alkalische milieu tot extra verbruik van CO₂ door het hydroxyde ion. Bovendien kan de reactieselectiviteit voor CO₂ elektroreductie verder worden verbeterd door het afstemmen van de grensvlak omgeving *via* het anioneffect, kationeffect en massatransporteffect. Een goed protisch anion zoals HSO₄⁻ kan extra protonflux toevoegen *via* het zuur-base-evenwicht om het milieu bijna neutraal te houden. In een zuur milieu versnelt een zwak gehydrateerd kation zoals K⁺ de CO₂RR terwijl het nauwelijks invloed heeft op de concurrerende protonreductie, terwijl het verminderen van het massatransport de protonreductie onderdrukt, wat leidt tot een hogere selectiviteit van de CO₂RR.

Het onderzoek naar de effecten van deze ondersteunende elektrolyt deeltjes op de evolutie van H₂ werd voortgezet in **Hoofdstuk 5**. We stelden vast dat de stationaire stroom van H₂ evolutie merkbaar toeneemt met de concentratie van het protische anion, namelijk HSO₄⁻ en de zwak gehydrateerde alkali-kationen (K⁺ en Cs⁺). Deze toename wordt toegeschreven aan de koppeling van protonreductie met de homogene zuur-base evenwichten, namelijk de dissociatie van HSO₄⁻ en hydrolyse van K⁺ en Cs⁺. Dit bevestigde het bufferend vermogen van de alkali-kationen en hun impliciete rol als zwakke protonendonator, die experimenteel kan worden waargenomen en gekwantificeerd met RDE. Kwantitatieve studies verduidelijkt dat de evolutie van H₂ in dit geval een massatransport gelimiteerd proces is, gekoppeld aan een chemische reactie (d.w.z. de zuur-basereactie). Bovendien werd de lineaire relatie tussen de concentratie van elektro-inactieve stoffen en de Koutecký-Levich-helling waargenomen, waaruit de pK_a van de betrokken protondonor kan worden afgeleid. De overeenkomstige pK_a's van HSO₄⁻, K⁺, en Cs⁺ werden bepaald op respectievelijk 2,06, 2,52, en 2,48.

总结

从界面 pH 角度揭示 CO₂ 电还原反应和析氢反应的电解液效应

界面环境在电化学反应中的作用越来越受到重视，尤其是在涉及质子或氢氧根离子的反应中。体相电解质溶液中弱质子供体，如质子型阴离子与弱水合型阳离子等，其酸碱平衡改变了界面环境，继而影响电化学反应的速率和选择性。这使得界面酸碱度(pH)成为研究电解质效应的关键参数。在本论文中，我们设计了一种原位界面 pH 传感器，并还原了 CO₂ 电还原反应 (CO₂RR) 和析氢反应 (HER) 过程中的界面 pH 的演变。我们发现 CO₂RR 和 HER 的活性和相互竞争在很大程度上取决于界面 pH 值。通过改变电解液条件可以调控界面 pH，影响界面电化学环境，从而谐调 CO₂RR 和 HER 的反应活性及竞争关系。

在第二章中，我们以旋转环盘电极技术为基础开发了一种原位界面 pH 传感技术。在规范的传质条件下，以 4-羟基氨基苯疏酚/4-亚硝基苯疏酚 (4-HATP/4-NSTP) (一对高灵敏度的伏安型 pH 传感电对) 修饰的金环电极作为金盘电极的原位 pH 计实时反映电化学反应过程中界面 pH 的变化。它适用于很宽的 pH 值范围，且不会对反应造成任何额外的干扰。实验证明，在析氢反应过程中，界面 pH 值受电极电势 (电流密度)、电极旋转速率和体系缓冲容量的影响。更负的电极电势和更大的电流密度导致界面 pH 值升高，而更高的旋转速率和更大的缓冲能力则抑制界面 pH 值的变化。而在 CO₂RR 的过程中，由于 CO₂ 和 HCO₃⁻ 的缓冲作用，情况与 HER 有所不同。第三章指出，CO₂RR 过程中，随着电极表面极化程度的增加会出现两种情况。在较低负电位下，由于 CO₂ 的缓冲作用，界面 pH 值稳定在 7 左右，而随着电流密度增大，界面 CO₂ 耗尽，pH 值会跃升至 9，HCO₃⁻开始缓冲，从而导致了 CO₂RR 的衰减，其竞争反应——水还原反应开始占主导地位。调整体相的传质条件及阴离子的缓冲容量能调控电化学界面环境。此外，电解液中阳离子的尺寸和浓度也会影响界面 pH 值的变化。其中，阴离子缓冲剂的作用最大，而传质和阳离子在抵御界面 pH 值的上升方面的效率较低。事实上，在 CO₂RR 过程中，传质条件对于界面 pH 的调控相当有限，实验表明，即使在强制对流 (2500 转/分钟) 条件下，界面 pH 值仍高达 11。值得注意的是，增大缓冲容量或阳离子浓度虽然能有效抑制界面 pH 的上升从而促进 CO₂RR 的活性，但并不能显著提高 CO₂RR 的选择性和效率，因为水还原反应也得到了大幅度的提升。

为了保持 CO₂ 浓度，抑制水还原反应的发生，在第 4 章中进行了弱酸性电解质条件 (体相 pH 值为 3) 下的 CO₂RR 研究。实验表明，在弱酸性条件下，CO₂RR 与质子还原反应竞争。随着电极表面极化程度增加，界面质子耗尽达到传质极限平台时，界面环境接近中性。由于 CO₂RR 产生的氢氧根离子与界面质子发生均相反应，有效地抑制质子还原反应，从而显著地提升了 CO₂RR 的选择性和效率。但到达传质平台末

端, 水还原反应开始发生, 界面 pH 迅速上升, 导致界面 CO_2 的消耗及 CO_2RR 活性及效率下降。类似地, 通过阴离子效应、阳离子效应和传质效应可以调整界面环境, 提高 CO_2RR 的选择性。合适的质子型阴离子(如 HSO_4^-)可通过酸碱平衡释放质子, 提高质子通量, 保持接近中性的界面环境。另外, 在酸性环境中, 弱水合型阳离子(如 K^+)及低传质速度有助于提高 CO_2RR 的选择性: 弱水合型阳离子在促进 CO_2RR 的同时几乎不影响质子还原反应, 而降低传质速度则在抑制质子还原的同时几乎不影响 CO_2RR 。

第 5 章继续研究了支持电解质物种作为潜在的质子供体对于析氢反应的影响。我们观察到, 随着支持电解质 (HSO_4^- 和弱水合型碱金属阳离子 (K^+ 和 Cs^+)) 浓度的增加, 析氢反应的稳态电流明显增加。这是由于质子还原反应与酸碱平衡均相反应(即 HSO_4^- 的解离以及 K^+ 和 Cs^+ 的水解)的耦合。这有力地证实了弱水合型碱金属阳离子物种的缓冲能力及其作为潜在弱质子供体的作用。结果表明, 该耦合反应过程仍受传质控制, 但其反应动力学受均相反应影响。通过 RDE 实验可以对其进一步量化: 质子供体的浓度与 Koutecký-Levich 斜率成线性关系, 由其斜率中算得 HSO_4^- 、 K^+ 和 Cs^+ 的 pK_a 分别为 2.06、2.52 和 2.48。

List of Publications

Chapter 2

Monteiro, M. C. O.; **Liu, X.**; Hagedoorn, B. J. L.; Snabilié, D. D.; Koper, M. T. M., Interfacial pH Measurements Using a Rotating Ring-Disc Electrode with a Voltammetric pH Sensor. *ChemElectroChem* 2021, 9 (1), e202101223.

Chapter 3

Liu, X.; Monteiro, M. C. O.; Koper, M. T. M., Interfacial pH measurements during CO(2) reduction on gold using a rotating ring-disk electrode. *Phys. Chem. Chem. Phys.* 2023, 25 (4), 2897-2906.

Chapter 4

Liu, X.; Koper, M. T. M., Tuning the Interfacial Reaction Environment for CO(2) Electroreduction to CO in Mildly Acidic Media. *J Am Chem Soc*, 2024, 146 (8), 5242-5251.

Chapter 5

Liu, X.; Koper, M. T. M., The Effect of the Electroinactive Species on the Steady-State behavior of Hydrogen Evolution in Mildly Acidic Media. *Electrochimica Acta*. 507, 145068.

Other Publications

Ye, C, **Liu, X.**, Koper, M. T. M., The role of cations in hydrogen evolution reaction on a platinum electrode in mildly acidic media. *Electrochemistry Communications* 166 (2024): 107784.

Wang, Y., Seki, T., **Liu, X.**, Yu, X., Yu, C. C., Domke, K. F., ... & Bonn, M., Direct probe of electrochemical pseudocapacitive pH jump at a graphene electrode. *Angewandte Chemie International Edition*, 2023, 62(10), e202216604.

Nan, W.J., **Liu, X.**, Originating the Driving Force of Photoinduced Interfacial Electron Transfer by Multimode Scanning Electrochemical Microscopy, *The Proceedings of the National Academy of Sciences* (submitted).

Liu, X., Tian, Z. Q., & Zhan, D. Optimizing the interfacial electron transfer capability of single layer graphene by thermal annealing. *Chemical communications*, 2020, 56(2), 253-256.

Han, S., Liu, S., Wang, R., **Liu, X.**, Bai, L., & He, Z. One-Step Electrodeposition of Nanocrystalline ZnxCo3-xO4 Films with High Activity and Stability for Electrocatalytic Oxygen Evolution. *ACS Applied Materials & Interfaces*, 2017, 9(20), 17186-17194.

Curriculum vitae

Xuan Liu was born on the 7th of August 1995 in Sichuan, China, where she spent her childhood and has a most beautiful memory. In 2003, she moved to Chengdu, where she finished her primary and secondary education and developed an interest in Chemistry.

In 2013, Xuan entered Central South University in Changsha, China, and majored in Applied Chemistry. During her four-year undergraduate study, she was well-prepared in the chemical fundamentals and principles and awarded the Excellence prize and the First-prize Scholarship each year. Most importantly, she developed a passion for electrochemistry and started her science journey in a lab of the electrochemical research institute in 2015. Her first project here was concerned with CO₂RR, where she synthesized three different-structured copper materials and examined their CO₂RR performances. The flower-like nano-Cu particles showed the highest amount of active sites and therefore the highest CO₂RR activity compared with the oxide-derived Cu and the planar Cu, making her realize that the nature of the electrode surface largely influences the electrochemical reaction activity.

In 2017, Xuan continued the research of electrode surface engineering as a master student at Xiamen University in China under the supervision of Zhongqun Tian, during which she was thoroughly educated in the basics and methods of electrochemistry and became experienced with the Scanning Electrochemical Microscopy (SECM) technique. She designed and synthesized a model electrocatalytic system consisting of monodispersed hexagonal nano-Ag crystals electrodeposited on single-layer pristine graphene, and SECM characterization suggested that electron transfer performance of the system correlates with the surface potential along the Ag-graphene interface, making her increasingly appreciate the vital importance of the electrode surface and the structure-activity relationship in electrochemical studies. This study was prized as the Provincial Excellent Master Project.

In 2020, Xuan was enrolled in the TRANSCRIPT project which aimed to transform carbon-rich industrial waste gases of metallurgical plants into valuable products. This project was a collaboration between Leiden University and Utrecht University and supported by Tata Steel Nederland Technology BV and the Dutch Research Council (NWO). In the pursuit of a PhD career at Leiden University in the Netherlands under the supervision of Marc Koper, her research extended from the electrode surface to the other side of the electrochemical interface, namely the interfacial electrolyte. With an interfacial pH sensor devised by RRDE coupled with a voltammetric redox couple, she succeeded in monitoring the variation of the interfacial pH with the electrolyte conditions during the reaction process of CO₂RR and HER,

and uncovering the interaction between the interfacial pH and other interfacial electrolyte effects, and its influence on the CO₂RR and HER. During the four years, Xuan was devoted to activities more than research, which enriched her PhD career and improved her multiple skills. She attended the Catalysis An Integrated Approach (CAIA 2021) course and the SurfCat summer school in Denmark and presented her work at the 74th annual meeting of ISE, the 32nd Topical meeting of ISE, the Netherlands' Catalysis and Chemistry Conference (NCCC) and the MaterialenNL conference. She also assisted in the practical courses and internships of BSc students at Leiden Institute of Chemistry.

Acknowledgment

I would not have been where I am without all the help and contributions I got. Genuine gratitude goes to but is not limited to everyone named below.

First of all, I'd like to thank my supervisor, Marc Koper, for giving me the offer four years ago when I was left at the crossing of life and wondering where to go. Thank you for being nice and patient even with my stupid questions. Thank you for always saying "You are doing well". That means a lot. Thank Wentian for always being an approachable hand in the lab to help me out uncountable times with the machines, the computers, and the mathematics. Thank you to all the members of our project Zhiqin, Rafaël, Alisson, and Quentin for supporting each other at every progress meeting, cluster meeting, and annual meeting. Thanks to all the CASC members for every valuable suggestion and insight, and for creating such a welcoming and cheerful environment for our research. Thank Linfan, Xiaoting, Chunmiao, Jinwen, and Mingchuan for every quality conversation we had in and out of the lab and for being considerate and enthusiastic to help me merge into the new life here in Leiden. Thank everyone who had heard me out patiently with all my complaints and puzzles and comforted me a lot.

Most importantly, I am grateful for all the love that accompanied me through all the years. Thank you Granma and Grampa for bringing me up, shaping me up, and cheering me up. It's you with every meal and every effort of loving me that brings me here today. Thank you Mama and Papa for always fighting every chance to be there for me, either physically or remotely. Thank you for your unconditional support and understanding and for letting me be myself to discover who I am, even though I've been moving further and further away from you physically since I pursued my ambition. Thank you Qi for being the pillar of my mental health and my private container for taking in the negative energy and giving out love and thoughtfulness in return. Thank you for being the number one on my call list and being the one I feel free to bother anytime even with the jet lag. You have been the sunshine during the bad days throughout the last years (although sometimes you bring a storm).

Lastly, thank myself for being brave till I get there.

